Fluid Displacements during Multiphase Flow Visualized at the Pore Scale using Micromodels

Master Thesis in Reservoir Physics

Håvard Nakken Follesø

Department of Physics and Technology
University of Bergen

June 2012

Acknowledgements

I would like to thank Professor Arne Graue for the opportunity to work with a topic of personal interest, and for guidance and support throughout the work with this thesis.

To Dr. Martin Fernø, thanks for guiding me both in the experimental work and writing process. Your great efforts were highly appreciated.

Thanks to everyone at the reservoir physics group at the Dept. of Physics and Technology that has willingly shared their expertise and knowledge. I would like to mention Dr. Geir Ersland, Dr. Åsmund Haugen, PhD. Knut Arne Birkedal, PhD. Lars Petter Haugen and PhD. Øyvind Eide.

I would like to thank my lab partner PhD. Jarand Gauteplass, for all the knowledge and experienced you shared, and the hours we spent at the laboratory.

Thanks to RICE University, and especially Assistant Professor Sibani Lisa Biswal and Professor George J. Hirasaki for a pleasant stay, and for sharing their knowledge and equipment.

Thanks to all my fellow master students for all the laughs, conversations and countless hours at room 506, Malin Haugen, Andreas Lien, Jørn-Anders Fløysand Tveit, Anders Christophersen, Eirik Fosse, Ane Skibenes, Glenn-André Kvinge and Torstein Skagseth. You all made my time at the university a pleasant stay.

Lastly, I would like to my girlfriend Linn-Yvonne Mindaas, for all the moral support and love you shared.

Summary

Increasing the recovery from oil reservoirs by injecting CO_2 is a measure that has great potential, and research in that topic has been given much attention at the Dept. of Physics and Technology at UoB. Many of the properties of CO_2 in both miscible and immiscible displacement have been established from experimental work on core plugs and sandstone blocks, and by numerical simulations. Knowledge of fluid displacements during multiphase flow may provide essential information to the understanding of flow mechanisms that enhance oil recovery, and direct visualization of fluid flow in micromodels is a powerful tool to obtain this. The experimental work on micromodels and flow visualization in this thesis was the very first at Dept. of Physics and Technology, and fundamental studies of water imbibition and oil drainage was as important as subsequent CO_2 EOR studies.

Fluid displacements during multiphase flow at ambient pressures and temperatures were visualized in micromodels by the use of a microscope and a camera. Both two-phase and three-phase flow was studied, and by adding Fluorescent additives to the water and oil phases could three phases be visualized simultaneously in the experiments. Control on fluid flow could be maintained by adjusting injection rates and changing boundary conditions, allowing fluid flow in different flow regimes to be studied. Flow both at the pore scale, which was largely determined by capillary pressure, and over the complete pore space of the micromodels, where viscous forces contributed, could be compared directly by visual observations. As the micromodels were constructed by sophisticated techniques and retained many properties of real porous rocks, the observed flow processes were assumed to be representative to those in real rocks.

Three-phase flow was studied for water/n-decane/CO_2 fluid systems, and two-phase flow for water/n-decane, water/CO_2 or water/air systems. Two-phase flow was found to be occurring in two distinct flow regimes, both in spontaneous imbibition, and in primary drainage experiments. In the first flow regime, a stable fluid front advanced through the pore network with good sweep efficiency, resulting in low residual saturation of the displaced fluid. In the second flow regime, instabilities in the displacements were manifested by capillary fingering, and poor sweep efficiency of the displaced fluid was achieved. Fluid displacement mechanisms at the pore scale were studied in great detail by keeping the flow rate in the pore network low. The dominating mechanisms in both three-phase and two-phase flow were found to be piston-like displacement of one fluid by another, either by a stable moving interface or through instant jumps. Flow through fluid films, gas dissolution, gas expansion, snap-off mechanisms and diffusive processes were also observed.

Decane was found to be spreading in the water/n-decane/CO_2 system at the experimental conditions. This ensured an efficient oil production at the pore level from CO_2 gas injection, even when the water saturation was high. This meant that CO_2 only contacted the oil, which therefore could be displaced directly, while water had to be displaced by oil through multiple displacement events. It was found that CO_2 flowed through the pore space in preferred flow paths, mainly through oil-filled pores. When the amount of oil in these flow paths decreased as it was produced, the CO_2 flow shifted to new preferred paths. The spreading layer was found to cause an efficient oil production for two main reasons:

1. The spreading layer of oil was produced together with the CO_2
2. By ensuring that preferred CO_2 flow paths were through oil-filled pores rather than water-filled pores

Contents

1 Introduction

Oil production from reservoirs is a complex matter where viscous-, capillary- and gravity forces affect fluid flow involving water and oil, and possibly gas and/or other injected substances. The different fluids also interact with each other and the porous medium through which it flows, further complicating the process. In most water-wet reservoirs, viscous forces favor mobilization of oil, while capillary forces tend to keep it in place. Gravity forces affect the displacements due to density differences in fluids, but are commonly of magnitudes smaller than at least one of the two other forces. The best means to increase the oil production is therefore by increasing the viscous forces, or reducing the capillary forces. This is done by waterflooding or gasflooding reservoirs to push the oil out viscously, or by injecting fluids or other chemicals able to alter the properties of the oil that makes it flow easier. The latter method is referred to as enhanced oil recovery (EOR), and these methods are normally applied on the residual capillary trapped oil when water- or gasflooding no longer can produce the oil economically beneficial.

CO_2 gas injection after waterflooding is an EOR measure that has great potential in reducing the residual oil saturation. It has been estimated that CO_2 flooding may produce an additional 7 to 15 % of the initial oil in place (Mathiassen, O.M., 2003), and with the numbers of large producing fields on the Norwegian continental shelf, where high residual oil saturation is in place, even a small percentage increase in recovery results in large additional volumes of oil being produced. CO_2 is also an important topic due to increasing greenhouse gases in the atmosphere and global warming. Carbon capture and storage (CCS), where CO_2 is stored in the subsurface in water aquifers, has been researched with increasing effort for this reason.

Fluid flow in oil reservoirs occurs over hundreds to thousands of meters, and is controlled by the directions of large viscous forces. Knowledge of flow processes is commonly gained by performing laboratory measurements on core plugs taken from reservoirs where information is desired. Flow in core plugs over a length of centimeters is able to reproduce many of the flow properties found in real reservoirs if the subsurface consists of porous rocks with similar properties. When flow on the pore scale is considered, which is over lengths of micrometers, flow processes differ from those at the larger scales, and is controlled to a larger degree by capillary forces. Flow on the pore scale does, however, decide the large scale flow patterns in reservoirs, and optimizing oil recovery at the pore scale will increase the ultimate oil recovery. Therefore, knowledge of the displacement processes during multiphase flow on the pore scale can be used to optimize the production process in oil reservoirs.

Micromodels allow multiphase flow at the pore scale to be visualized directly, as fluids flow in a confined pore network that has been etched into a material and closed from the surroundings by bonding to a transparent glass plate. In the same manner that core plugs are taken from the reservoir to best represent its properties, the pore network of the micromodels can be created from thin-section images of the reservoir rocks, and processed digitally so that the same properties are retained. Flow in micromodels is dominated by capillary forces in the pore-to-pore displacements, but viscous forces may contribute to the flow over the entire pore network. This allows the importance of viscous forces to capillary forces to be investigated and related to the oil production efficiency at larger scales, for different flow conditions and fluid systems.

The Microfluidic Laboratory at the Dept. of Physics and Technology was established during this thesis, and the work presented here was the very first experimental work that was performed in micromodels at this laboratory. Many of the experiments were therefore fundamental experiments

where basic flow processes were investigated, but study of flow processes during CO_2 gas injection for increased oil recovery was also a major part of this thesis.

Part 1: Theory

2 Reservoir Physics Fundamentals

2.1 Porosity

Porosity is one of the most important properties of a reservoir rock as it gives a direct measurement of the volume of fluids that can be stored underground. Effective porosity, which is the porosity of interest in petroleum production, is defined as the interconnected void space of a rock as a fraction of the total volume of the rock, and is denoted φ (Zolotukhin, A.B. and Ursin, J.R., 2000):

$$\varphi = \frac{V_p}{V_b} \qquad \textbf{(1)}$$

where V_p is the pore volume and V_b the bulk volume of the rock.

The effective porosity depends on rock type, grain size, grain shape, packing and orientation, cementing, weathering, compaction and clay content (Zolotukhin, A.B. and Ursin, J.R., 2000).

2.2 Absolute Permeability

The capability of a reservoir rock to transmit fluids through its network of interconnected pores is called its transmissibility, and fluid flow in porous media is commonly described by the phenomenological Darcy equation:

$$Q = \frac{K\,A(p_1 - p_2)}{\mu\,L} \qquad \textbf{(2)}$$

where:
K= Permeability [D]
μ = Viscosity [cP]
Q = Volumetric flow rate [cm^3/s]
A = Cross-sectional area of flow [cm^2]
L = Length of flow [cm]
p_1 = Upstream pressure [atm]
p_2 = Downstream pressure [atm]

Darcy's equation states that fluid flow through a porous medium is proportional to the pressure difference across its length in the direction of flow (Zolotukhin, A.B. and Ursin, J.R., 2000). The proportional coefficient k is constant for a specific medium and is called its permeability. For Darcy's law to be valid, the following conditions need to be satisfied:

- Horizontal flow
- Incompressible fluid
- 100 % saturation of the injected single fluid
- Stationary flow
- Laminar flow
- No chemical reaction between the fluid and the porous medium

The conditions stated above implies that Darcy's law is only valid at low flow rates for liquids at what is called linear laminar flow. However, when permeability is measured in the lab, gas is commonly used. The benefit of using a gas in an absolute permeability measurement is that liquids tend to interact chemically or electrostatically with the porous rock, while an inert gas will not (Zolotukhin, A.B. and Ursin, J.R., 2000).

Because gas is highly compressible, its flow rate is dependent upon the pressure. For gas permeability calculations, one assumes constant mass flux instead of constant rate for a given pressure difference across the medium. The expression for volumetric flow can be described by:

$$\overline{Q} = \frac{KA}{2\mu \overline{p}} \frac{p_1^2 - p_2^2}{L} \quad \textbf{(3)}$$

where $\overline{Q}$ is the mean volumetric flow rate [cm^3/s] at the mean pressure $\overline{p}$ [atm].

At high pressures, gases behave more like liquids, and as a result of this the measured air permeability will decrease with increasing pressure. By plotting permeability against the reciprocal of the mean pressure, one can estimate the absolute permeability by extrapolating to $1/\overline{p}$ = 0, meaning that $\overline{p} \rightarrow \infty$ where the gas behaves like a liquid. The reason for this behavior of gases is a phenomenon called the Klinkenberg effect. Molecules in a liquid at laminar linear flow will have decreasing velocity towards the walls of a porous medium and be stationary at the interface. Molecules in a gas, however, will have negligible friction against the walls and a higher velocity compared to liquids. Klinkenberg discovered that there was a linear relationship between the measured air permeability and the mean pressure, and produced the correlation for this defined by:

$$K = K_\infty \left(1 + \frac{b}{\overline{p}}\right) \quad \textbf{(4)}$$

where:
K = Air permeability [D]
K_∞ = Permeability at infinite mean pressure [D]
b = Klinkenberg factor
$\overline{p}$ = Mean pressure [atm]

2.2.1 Relative Permeability

When more than one fluid is present in the pore space, each fluid will face more resistance to flow compared to a single phase system and their effective permeabilities will be lower. The effective permeability of a fluid varies with fluid saturation, and the ratio of the effective permeability to the absolute permeability is the relative permeability:

$$k_{r,i} = \frac{K_{e,i}}{K} \quad \textbf{(5)}$$

where $K_{e,i}$ and $K_{r,i}$ is the effective and relative permeability, respectively, for fluid *i*. Relative permeability takes on values between 0 and 1.

Effective and relative permeability depend as mentioned on fluid saturation, but also on rock properties, absolute permeability, fluid properties, pressure and temperature (Zolotukhin, A.B. and Ursin, J.R., 2000). The saturation of the flowing fluid is the dominating parameter, and relative permeability for an oil-water system is therefore commonly plotted against water saturation.

A fluid has its maximum relative permeability when it has the highest possible saturation, defined as the end-point relative permeability. This value is commonly measured for a system with two or more fluids present as it indicates how fluids flow and their occupation in the porous system. A high value indicates that a fluid flows in the middle of pores and preferentially occupies the larger ones while a small value indicates that it flows along the surface of the grains and occupies the smaller pores. The systems wettability determines which one is preferred for the different fluids, a property that will be defined in section 2.4.

2.3 Capillary Pressure

When two immiscible fluids are present in a porous medium, the interface between them will be curved if one fluid is more wetting than the other. Capillary pressure, denoted P_c, is defined as the molecular pressure difference across this interface (Zolotukhin, A.B. and Ursin, J.R., 2000):

$$P_c = P_{NW} - P_W \qquad \textbf{(6)}$$

where P_{NW} and P_W is molecular pressure in the non-wetting and the wetting phase, respectively.

A simple relation of capillary pressure can be expressed when two fluids are confined in a cylindrical channel:

$$P_c = \frac{2\sigma\cos\theta}{r} \qquad \textbf{(7)}$$

where σ is the interfacial tension between the fluids, ϑ is the wetting angle and r is the radius of the channel.

This relation can be applied to porous media when making the assumption that pores are spheres and pore throats are cylinders. The advantage of expressing capillary pressure in this manner is that for a given capillary pressure the radius of the pores determines the fluid occupancy in the pores. However, in real porous media, no throats or pores will be perfect spheres or cylinders, and which phase occupies the different pores cannot be found directly from equation (7). As can be seen from Equation 6, the capillary pressure can be calculated from the different phase pressures, and capillary pressure therefore depends on fluid saturations. A common way to present capillary pressure is therefore to plot it against the wetting phase saturation. Two important processes in two-phase flow, imbibition and drainage, have different influence on the capillary pressure. During imbibition, the wetting phase saturation and pressure increase, and the capillary pressure decreases. During drainage, the non-wetting phase saturation and pressure increase, and the capillary pressure increases.

Figure 1 shows a primary drainage capillary pressure curve obtained on six Bentheim sandstone cores by the use of the porous plate technique. In this technique water-filled cores were mounted in a chamber and placed on a porous plate also saturated with water. The chamber was closed and the air pressure was increased stepwise. A given amount of water was displaced from the core through the porous plate at each pressure increment and the volume was found by mass balance

calculations. Air did not displace water from the porous plate below a threshold pressure, which meant that the average water saturation against applied air pressure was found.

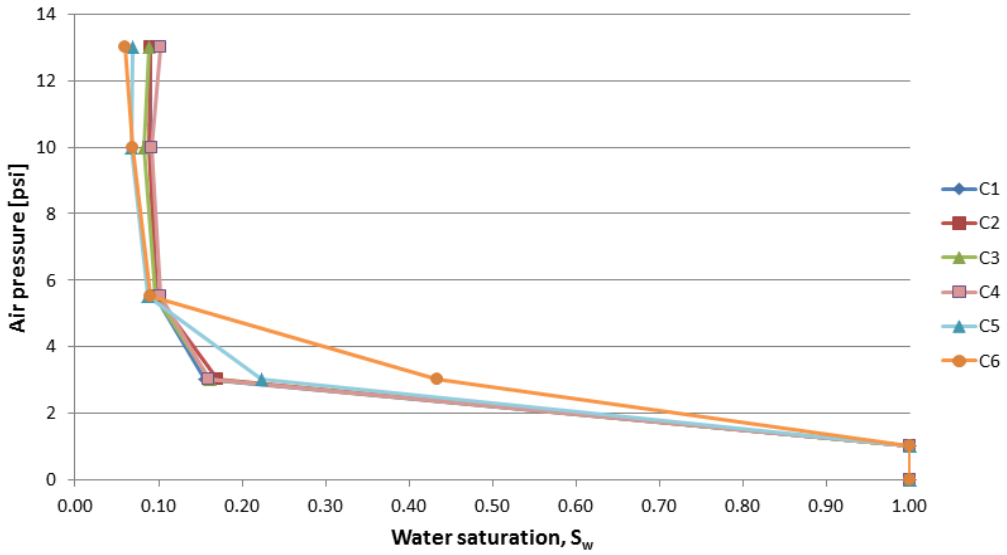

Figure 1: Capillary pressure curve during primary drainage for six Bentheim cores obtained by the porous plate method.

The process above was a primary drainage process where the water saturation decreased at each step from an initial 100 %. The average water saturation was only obtained at a few points as a low water saturation was reached after only small pressure increments. The true capillary pressure curve for the cores would have been smoother than they appeared in this example if continuous measurements could be obtained. However, regardless of how smooth the capillary pressure curve appears, pore scale events cause the capillary pressure to fluctuate during fluid flow in porous media. One reason for these fluctuations is a pore scale displacement phenomenon called Haines' jumps, and will be clear from the experimental observations on the pore level in micromodels later.

2.3.1 Haines' Jumps

Haines' jumps was first described by William B. Haines who studied hysteresis effects in capillary properties, and has later been investigated by several authors (Melrose, J.C., 1965) and (Morrow, N.R., 1970). Haines' jumps occur when the interface between two fluids reaches an unstable position as it advances through porous media when the capillary pressure increases or decreases.

In a drainage process the interface advances as the capillary pressure is increasing. This advance is steady as long as the interface remains stable, but if it reaches an unstable position in the porous media it jumps to obtain a stable position again. This occurs when the pore geometry causes the curvature between the two fluids to decrease to a position where it no longer is stable at the current capillary pressure (Melrose, J.C., 1965). The jump the interface makes is accompanied by a rapid decrease in capillary pressure. As an effect of this rapid jump, fluids elsewhere in the porous media redistributes, and the magnitude of the decrease in the capillary pressure depends on the displaced fluid volume compared to the systems capability to redistribute fluids elsewhere (Morrow, N.R., 1970). This nature of fluid movement through heterogeneous porous media is the reason for the fluctuations in capillary pressure during imbibition and drainage. These events are only occurring at the fluid-fluid interfaces which only exist in restricted areas of large samples, and the magnitude of the pressure drop is normally too small to be manifested on a capillary pressure curve.

Haines' jumps also occur during imbibition processes with opposite effect on the capillary pressure. A stable movement of the interface is accompanied by a decrease in capillary pressure, and when the curvature of the interface reaches an unstable position and makes a jump, a rapid small increase in capillary pressure follows (Melrose, J.C., 1965).

2.4 Wettability

2.4.1 Contact Angle Measurement

The wettability of a porous medium defines which fluid that is preferred to spread on the surface of the grains. For a system with two immiscible fluids the wettability can be estimated by measuring the contact angle between the fluids on a solid surface in equilibrium. This contact angle is called the wetting angle, ϑ_{ij}, where the notations *i* and *j* represents the two fluids, and is measured through the densest phase, *j*. In petroleum reservoirs, where oil and water is present, possible wettability configurations can be arranged into three different categories (Anderson, W.G., 1986a):

1) $0^o \leq \vartheta_{ow} \leq 75^o \rightarrow$ Strong to preferentially water-wet. Water adheres to the solid surface and oil resides in the middle of the pores. The end-point relative permeability will be high for oil and low for water.

2) $105^o \leq \vartheta_{ow} \leq 180^o \rightarrow$ Preferentially to strongly oil-wet. Oil adheres to the solid surface and water resides in the middle of the pores. The end-point relative permeability will be high for water and low for oil.

3) $75^o \leq \vartheta_{ow} \leq 105^0 \rightarrow$ Intermediate wet. The solid has no strong preference for oil or water to adhere to the surface, and end-point relative permeabilities for oil and water can take a range of values.

The equilibrium contact angle of a system is commonly different from the advancing and the receding contact angles, the contact angle when the wetting phase saturation is increasing and decreasing respectively. This is a phenomenon called contact angle hysteresis which is introduced due to surface heterogeneity and roughness in porous media (Anderson, W.G., 1986b). The advancing contact angle is equal to or larger than the receding contact angle.

The contact angle measurement is a quantitative method which determines the wettability of the surface it is measured on. For wettability measurements of large heterogeneous samples, for instance core plugs, two quantitative methods that measure the average wettability of samples are commonly used; the Amott-Harvey and the USBM methods (Anderson, W.G., 1986b). These methods will only be described briefly as alternative methods of measuring wettability, as they will not be used in this thesis.

2.4.2 Amott-Harvey Method

The Amott method uses both capillary imbibition and viscous displacement to measure the average wettability of a medium (Amott, E., 1959). The wetting preference for a porous medium saturated with oil and water is measured as follows:

1. A sample at residual oil saturation is immersed in oil for capillary imbibition and displacement of water, and the displaced water volume at equilibrium is recorded. For the system to reach equilibrium this process may continue for days or weeks.

2. Oil is injected into the sample by force, normally in a centrifuge, until the irreducible water saturation has been reached. The total volume of water displaced at this step, both capillary and viscously, is measured.

3. The sample is immersed in water, and the volume of oil displaced by capillary imbibition is measured.

4. Viscous displacement of oil by water is performed, and the total volume oil displaced is measured.

Amott expressed the results by introducing the terms displaced-by-oil ratio and displaced-by-water ratio. The displaced-by-oil ratio was defined as the volume water displaced spontaneously to the total volume water displaced, and the displaced-by-water ratio compared the similar volumes of displaced oil. Amott's method was later modified slightly, and the two displacement ratios introduced by Amott were combined to produce the Amott-Harvey index, here denoted *I* (Boneau, D.F. and Clampitt, R.L., 1977*)*:

$$I = \frac{\text{Volume oil displaced spontaneously}}{\text{Volume oil displaced total}} - \frac{\text{Volume water displaced spontaneously}}{\text{Volume water displaced total}}$$

It can be understood that for strongly water-wet cores no water will be displaced spontaneously as they are immersed in oil, and all the displaced oil will occur spontaneously. This gives an Amott-Harvey index of 1. For strongly oil-wet cores, the Amott-Harvey index will be -1 for similar reasons. The sample is said to be water-wet when $0.3 \leq I \leq 1$, oil-wet when $-1 \leq I \leq -0.3$, and intermediate wet when $-0.3 \leq I \leq 0.3$.

2.4.3 USBM method

The other common way to measure the average wettability, the USBM method, also utilizes the spontaneously displaced and forced displaced quantities of the fluids, but instead of looking at the volumes in each of these processes directly it looks at the work required to displace these volumes. The work done in each of these processes is related to the capillary pressure of the sample.

The volume of water displaced during the porous plate experiment described above requires a force, and the work needed during the displacement process is equal to the area under the drainage curve. To apply the USBM method to determine the wettability of the medium in question, a forced water imbibition process is also required. During a forced imbibition, a negative capillary pressure is obtained as the water saturation increases, and the volume between the forced imbibition curve and the x-axis equals the work done in this process. The way to combine the two amounts of work done as a measurement for wettability was introduced in 1969 (Donaldson, E.C., Thomas, R.D. and Lorenz, P.B., 1969). They labeled the area below the drainage curve A_1 and the area above the imbibition curve A_2, and defined the USBM index as:

$$W = \log\left(\frac{A_1}{A_2}\right) \qquad \textbf{(8)}$$

When $A_1 > A_2$ the USBM index gives a positive index indicating a water-wet sample, when the opposite is the case a negative number is returned indicating an oil-wet sample.

In practice, most petroleum reservoirs are fractional wet where the porous medium has some pores that are oil wet and some that are water wet. The reason for this is that polar compounds in crude oil alter the wettability of the grains, making them more oil-wet. When oil in a reservoir is unevenly distributed, often occupying only the largest pores, alteration of the wettability of only a portion of the grains produces the fractional wettability.

3 Description of Fluid Flow at Different Length Scales

Fluid flow in porous media at the micro scale has been studied extensively over many decades, and trying to describe macro scale laws by micro scale observations has been the purpose of many studies. One example of this approach is attempting to derivate Darcy's empirical flow equation (Equation 2) by averaging of micro scale laws. Upscaling from the micro scale is commonly done by averaging properties over a representative elementary volume (REV), the smallest volume that produce values representative for the medium as a whole, a definition introduced by Jacob Bear (Bear, J., 1988).

Fluid flow through porous rocks depends on pore scale properties at the scale of 10^{-6} m. When cores and blocks are of the magnitude of 10^{-1} - 10^{1} m, at what is called the Darcy scale, and real oil reservoirs are at 10^{3} – 10^{5} m, different approaches must be taken when trying to predict fluid flow for the different scales. A continuum description of the porous media is common at the Darcy scale, where all components involved are present in every volumetric part of the reservoir space, even if the volume considered approaches zero (Zolotukhin, A.B. and Ursin, J.R., 2000). In a continuum description, micro scale properties are averaged to constant values, or described by empirical relations. When flow is studied at the pore scale, however, properties like fluid saturations and phase pressures cannot be given constant values to represent every volumetric part.

In this thesis, multiphase fluid flow will be studied at the pore scale by the use of micromodels. Flow in micromodels can be studied over the complete pore network, which is large enough to meet the REV scaling requirements, in addition to pore level flow. This allows both viscous and capillary forces to influence the fluid flow, and pore scale events to be related to the larger flow pattern in the micromodels. Experimental results in micromodels are used to evaluate the validity of the observed pore level events in 2D models when describing 3D flow at the Darcy scale.

3.1 Micromodels for Studying Fluid Flow

Micromodels are suitable for experimental study of flow in porous media at the pore scale, the smallest scale relevant to petroleum recovery. Micromodels contain enclosed pore networks where flow can be observed visually in a microscope, making it possible to study how pore scale events affect flow patterns and displacement efficiency at larger scales. Visual studies enable several key features regarding oil recovery to be identified and described, and the effect of changing parameters like injection rate and types of injection fluids can be observed. Both naturally occurring displacement processes, such as imbibition and drainage of water, and EOR processes, such as CO_2 gas or CO_2 foam injection amongst many, can be studied by the use of micromodels.

Micromodels consist of a digitally constructed pore network etched into a material and enclosed by a transparent surface, which typically is glass or plastic. The pore network can be constructed manually after a desired design, or it can be constructed from 2D thin-sections of real porous rocks to represent a realistic pore structure. The first method is normally preferred when elementary study of flow physics with controlled flow conditions is the objective, while the second method is used to study fluid flow in real porous rocks. Micromodels can obtain a range of values concerning porosity, permeability, wettability, pore and grain sizes and shapes, grain surface roughness, pore network size and coordination number, the average number of flow entrance/exit paths from pores in the network.

The obvious advantage of micromodels is that flow can be studied visually. This does however put restrictions to the dimensionality of micromodels, which again limits the ability to perform direct

measurement of many relevant flow properties like relative permeabilities and fluid saturations. The reason for this is that real porous media have pores that are connected in 3D that will be isolated in 2D, which will affect the conductance and trapping of fluids. A pore network with a high coordination number will be less affected by the reduced dimensionality (Sarathi, P., 1986).

For many types of micromodels other disadvantages also exist, and an early study that investigated and listed the discrepancies was performed by Sarathi in 1986 (Sarathi, P., 1986). He argued that micromodels had to model the pore geometry and dimensions appropriately in order to realistically model the ratio of viscous to capillary forces, capillary pressure hysteresis, entrapment mechanics and remobilization of trapped fluids. The most important problems with micromodels he listed as follows:

- Difficult to obtain a specific etch depth repeatedly.
- Introduction of microscopic heterogeneities during the etching process.
- Larger pores in the micromodels compared to reservoirs lead to a Peclet number, which is the ratio of the time for a fluid to diffuse over a distance compared to the flow time, different from that found in reservoirs.
- Difficult to produce representative porous network sufficiently due to extreme variations in rock characteristics of real rocks.
- The fact that 2D micromodels do not permit the same level of continuity as 3D models.

With more recent construction techniques of micromodels, and with the pore network etched in silicon wafer instead of glass, Hornbrook et al. managed to eliminate all of the problems above except for the loss of dimensionality (Hornbrook, J.W., Castanier, L.M. and Pettit, P.A., 1991). This was also addressed, however, as in the construction process the pore structures that were created from the thin-sections of the rock were manually manipulated in order to increase the coordination number and maintain the connectivity found in real rock as much as possible. Limited strength of these micromodels, however, only allows small differential pressures across the pore network. The silicon wafer can withstand pressures of about 2 – 3 bars when no modifications to the micromodels to increase their strength are done. Micromodels constructed in silicon wafer with the construction techniques developed by Hornbrook et al. will be used in this thesis.

Flow in micromodels is in most situations capillary dominated due to the small dimensions. A typical viscous pressure drop along a throat or across a pore is typically of the order of one hundredth or one thousandth of the capillary pressure drop across a fluid interface (Blunt, M. and King, P., 1991). Viscous forces may however impact the macroscopic flow pattern in micromodels as the viscous pressure drop may be of comparable size over a number of pores. Depending on injection rate and fluid displacements both stable and unstable displacement can be achieved in micromodels. How flow is manifested can be described by comparing two essential parameters concerning two-phase flow, the capillary number and the mobility ratio. The dimensionless capillary number describes the ratio of viscous to capillary forces, and is often defined as (Moore, T.F. and Slobod, R.L., 1955):

$$N_c = \frac{v_i \, \mu_i}{\sigma_{ij}} \qquad \textbf{(9)}$$

In Equation 9, subscripts *i* and *j* denotes displacing and displaced fluid, *v* is the true flow velocity, the actual flow rate of the displacing fluid in the pore space which is higher than bulk flow velocity due to tortuous flow paths, μ is viscosity and σ is the interfacial tension between the fluids. The capillary number can also been defined in terms of the pressure drop across a flow length and the interfacial tension (Taber, J.J., 1969), and later the permeability was included so that a dimensionless number was obtained:

$$N_c = \frac{K\Delta p}{L\sigma_{ij}} \qquad \textbf{(10)}$$

where Δp and L is the pressure and the length between two points, respectively.

It can be seen that the two definitions for capillary number is related through Darcy's law (equation 2), so when replacing the absolute permeability in equation (10) with the effective permeability of the injected fluid, the capillary numbers are equal. Capillary forces become significant at capillary numbers < 10^{-5}, which can cause instabilities in the fluid displacement. The mobility ratio compares the mobility of the displacing fluid to that of the displaced fluid (Zolotukhin, A.B. and Ursin, J.R., 2000):

$$M = \frac{\lambda_i}{\lambda_j} = \frac{k^o_{r,i}\mu_j}{\mu_i k^o_{r,j}} \qquad \textbf{(11)}$$

where λ is the mobility, taken as the ratio of the end-point relative permeability, k_r^o, to the viscosity of the fluid.

Mobility ratios below and at unity favors a stable displacement while large mobility ratios (M > 10) may cause unstable displacement. Gravity effects on displacement stability are in most cases negligible for micromodels as they are 2D models with shallow etching depth. If they are placed vertically such that flow length is in the vertical direction, gravity may affect displacement pattern for fluids with large differences in density to some degree.

For two-phase flow of immiscible fluids in micromodels, it was found that different flow regimes occurred for different values of the capillary number and mobility ratio (Lenormand, R., Touboul, E. and Zarcone, C., 1987). Either the displacement of one fluid by the other was stable, or it experienced either viscous fingering or capillary fingering. The different scenarios can be organized after the principles of Lenormand et al., but reproduced slightly different here as they used other definitions for the capillary number and mobility ratio (Lenormand, R., Touboul, E. and Zarcone, C., 1988):

- Low capillary number and intermediate to low mobility ratios
    - Capillary forces dominate and displacement processes are primarily convective with instabilities in the form of capillary fingering.

- High mobility ratio and intermediate to high capillary number
    - Viscous forces dominate and displacement is primarily diffusive with instabilities in the form of viscous fingering.

- High capillary number and low mobility ratio
    - Stable displacement and a combination of convective and diffusive displacement processes take place.

There is a significant difference in instabilities from viscous fingering and capillary fingering that makes it easy to separate them visually without performing calculations of mobility ratio and capillary number. While viscous fingers develop in the direction of the pressure drop and fluid flow, capillary fingers develop in the direction of, normal to, and even in the opposite direction of the

general flow direction, entering either the largest pores during drainage or the smallest throats during imbibition, as capillary fingers are controlled by the capillary pressure.

A theoretical description of two-phase fluid flow in porous media where viscous forces are negligible and flow is completely dominated by capillary forces was introduced by Wilkinson and Willemsen (Wilkinson, D. and Willemsen, J.F., 1983), which they named the invasion percolation theory. The theory describes a situation where the wetting phase spontaneously displaces the non-wetting phase in the pore space in series of discrete jumps as the fluid interface moves quickly through narrow throats and stagnates at wider pores. The fluid always follows the path of least resistance, and hence, the throats are always filled before the pores. Only one place at a time in the porous media does the wetting phase advance, and the smallest available pore decides the filling direction. This fluid movement introduces trapping of the non-wetting phase, and the invasion percolation theorem does not allow trapped fluid to be mobilized. It was found that applying the invasion percolation theorem in 2 dimensional models meant that once breakthrough of the wetting across the network occurred, no more non-wetting fluid was displaced.

Part 2: Results and Discussions

4 Experimental Apparatus

4.1 Microfluidic Laboratory at Dept. of Physics and Technology

Figure 2 shows the experimental setup designed for visualization of flow and study of pore scale phenomena in micromodels by the use of an inverted microscope. The setup was made so that different fluids could be injected at different rates and injection pressures.

Micromodels were mounted in custom-made holders, which were placed on the stage of the inverted microscope. The holders were connected to syringe pumps for injection of liquids, or to a CO_2 tank for CO_2 gas injection, with Swagelok and NPT tubing and fittings. Pressure transducers were connected to the flow line to measure both the gauge pressure and the differential pressure. Digital time-lapse images were obtained during flow experiments by a computer controlled camera. Injected fluids were filtered through an in-line 2 µm sized mesh before flowing into the micromodels, to avoid unwanted particles entering and blocking flow paths.

Figure 3 shows a photograph of the microfluidic setup. At this time two absolute pressure transducers were present, but one of these were later were replaced by a differential pressure transducer.

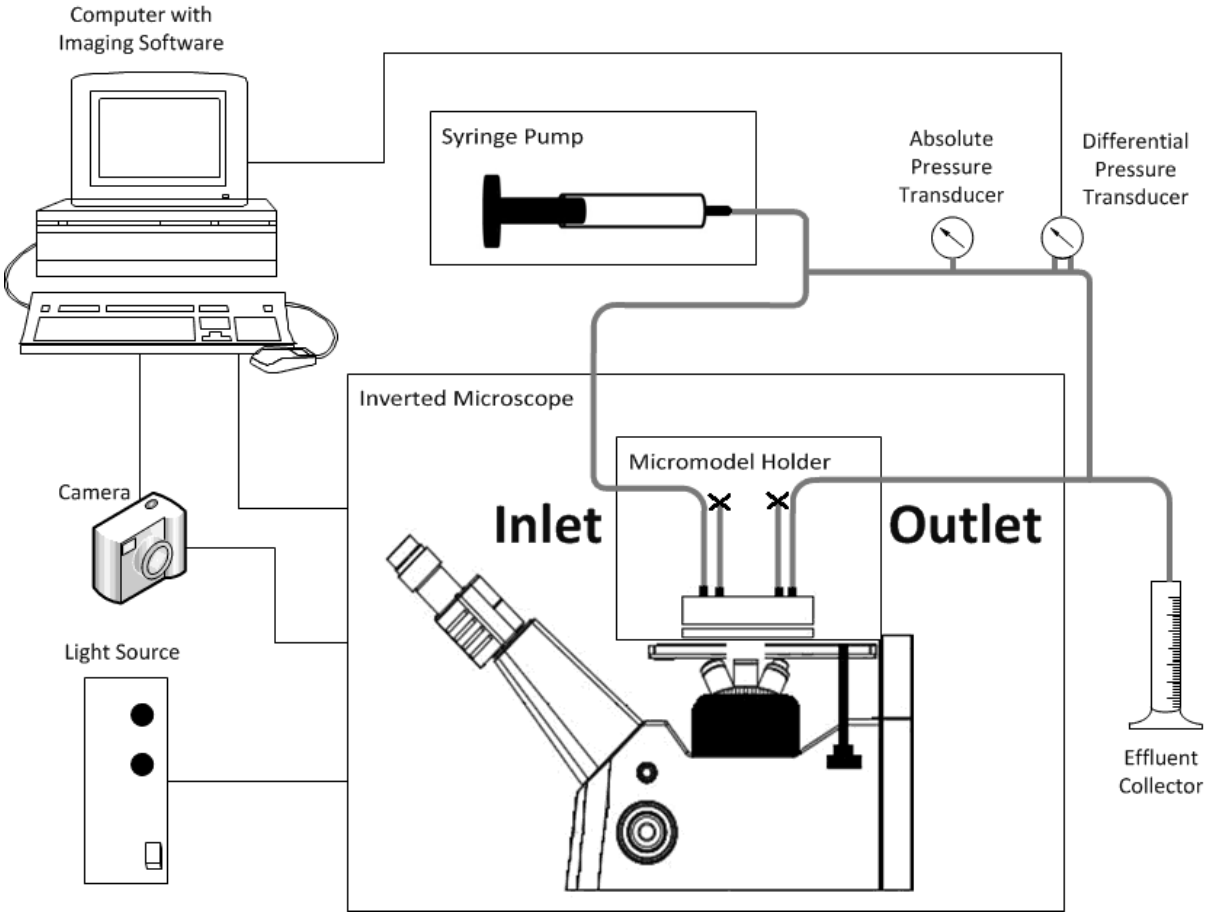

Figure 2: Sketch of the experimental setup for micromodel experiments at the microfluidic laboratory. When CO_2 gas was injected, a CO_2 tank was connected replacing the syringe pump.

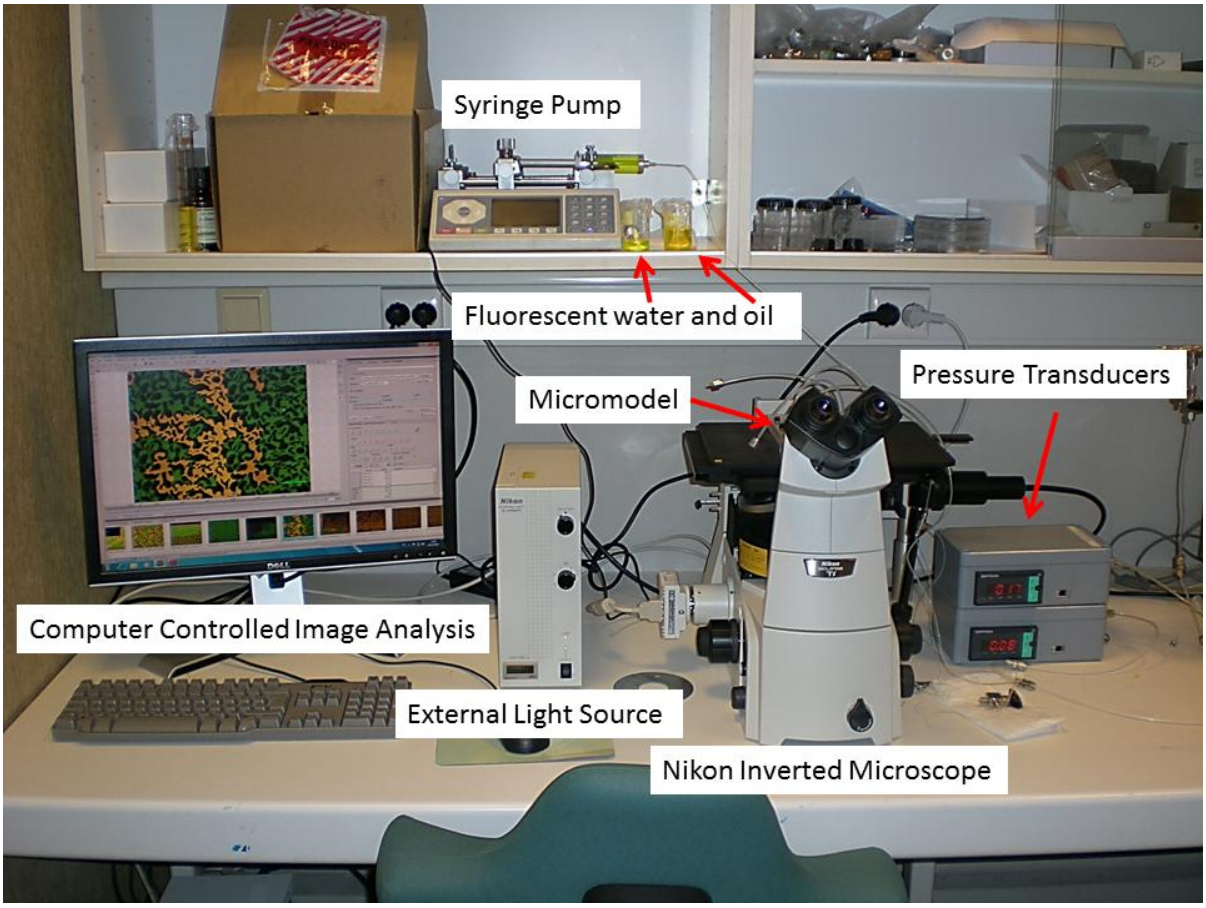

Figure 3: Microfluidic laboratory equipment setup

4.1.1 Micromodel Holders

Micromodel holders were designed and manufactured at the Dept. of Physics and Technology to position the porous network close the microscope, and for fluid injection and production.

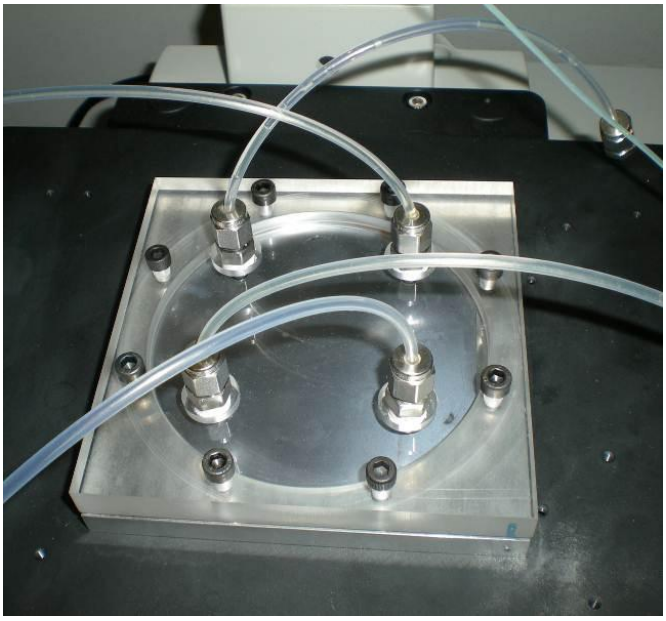

Figure 4: Close-up photo of a micromodel holder. A silicon micromodel has been placed between the two plates, and tubing has been connected to four ports where injection of fluids can be made.

The holders consisted of two plates, one made of Plexiglas and one made of aluminum, with space for the micromodels in between. The aluminum plate was designed to minimize the distance between the objective and the micromodels. The bottom Plexiglas plate had four holes with NPT fittings for injection and production of fluids. Small O-rings were placed between the micromodel and the Plexiglas plate to ensure that fluids would enter the micromodel through the holes, instead of spreading out on top of it. The two plates where fastened together with the micromodel in between to keep it in place and avoid leakage.

4.1.2 Pressure Transducers

Two different types of pressure transducers were connected to the setup; one gauge pressure transducer that could measure pressures up to 2 bars, and one gauge pressure transducer with a pressure range up to approximately 15 bars (200 psi), which also could measure the differential pressure. The latter pressure transducer was connected to a computer making it possible to log the pressure throughout experiments.

The two pressure transducers that can be seen in Figure 3 were constructed at the Dept. of Physics and Technology, and had an uncertainty of ± 1 % of full scale. The one of these that were used in this thesis had a full scale of 2 bars, which meant that pressure was measured with an uncertainty of ± 0.02 bars. The Paroscientific Series 6000 Transmitters package was used for differential pressure measurements and logging of pressure. It consisted of a DigiQuartz® pressure transducer, connected to a digital interface board, which was connected to a computer. The pressure transducer could measure pressures up to about 15 bars with an uncertainty of ± 0.01 % of full scale, or ± 0.015 bars. Figure 5 shows the integrated system with the pressure transducer to the left and the digital display to the right. In this picture, the 2 µm filter can also be seen in the flow line, before the pressure transducer.

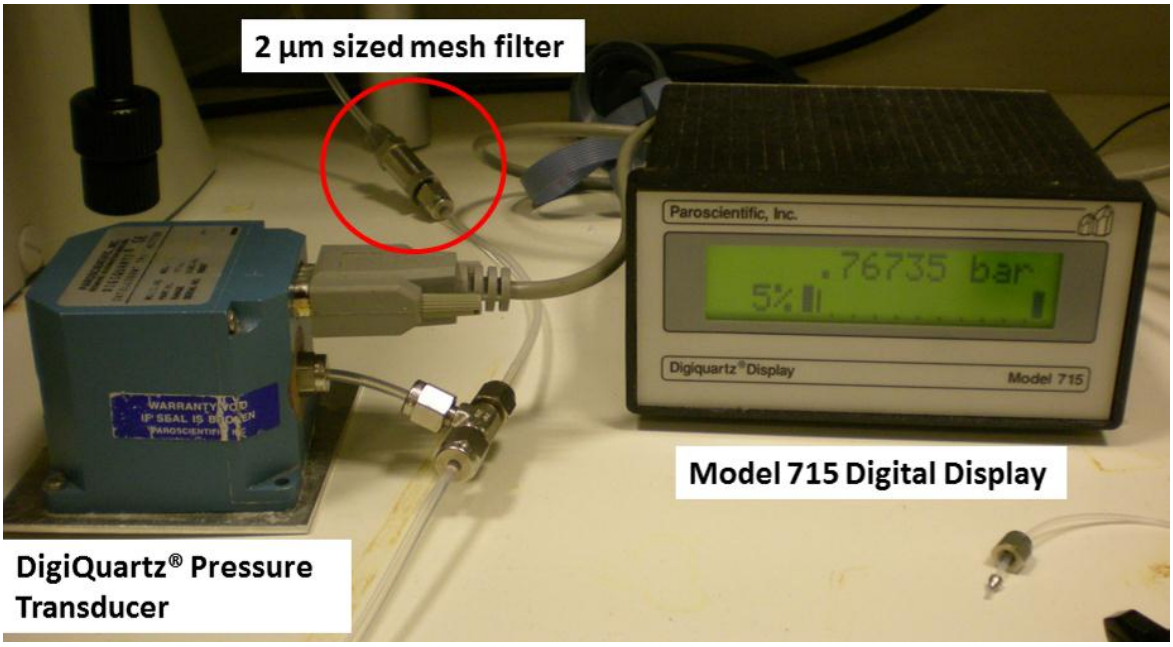

Figure 5: Paroscientific Series 6000 pressure transmitter system for logging of pressure.

4.1.3 Syringe Pumps

A Nexus 3000 KR Analytical syringe pump (seen in Figure 3), and a Pharmacia LKB P-500 pump (Figure 6), were used for injection of liquids. The Pharmacia pump had a minimum injection rate of 1 mL/h,

so for all rates below this the Nexus 3000 was used. Commonly, filling of the micromodels to 100 % water saturation was performed with the Pharmacia pump, as it had two syringes making continuous injection of fluids possible, while the syringe of the Nexus 3000 had to be refilled manually.

Figure 6: Pharmacia LKB P-500 syringe pump with two syringes.

4.1.4 Nikon Eclipse TI-FL Inverted Microscope

An inverted microscope was used for studying displacement processes in the micromodels. In an inverted microscope, studied object is placed above the objective lenses instead of below, which allowed extra space for the holders and equipment needed to flood the micromodels. An external adjustable light source was connected to the microscope via optical fiber cable.

Four different objective lenses were installed to the microscope with different magnification capabilities: 2x, 5x, 10x and 20x zoom. In addition, the microscope had a built-in 1.5x zoom that could add up with the objectives, thus making a 30x magnification possible. The study areas covered by the different objective lenses are given in Table 1:

Table 1: Study areas covered by the different objective lenses

Objective lens	Width [µm]	Height [µm]
2x zoom	6167.3	4629.6
5x zoom	2470.3	1854.3
10x zoom	1238.5	929.7
20x zoom	626.9	470.6

4.1.5 External Light Source

Nikon Intensilight was used as an external device that delivered light to the microscope. The lamp could deliver light of high intensity over a broad wavelength spectrum, and was especially suited for the green spectrum at wavelengths around 450 nm to 500 nm (Nikon Instrument product information). This was very convenient as fluorescent additives used in the water phase in the

experiments emitted light with these wavelengths. The light intensity could be changed between six different levels, and while a high intensity was required at low magnification, the ability to reduce it at greater magnification was crucial in experiments where fluorescence were used to extend its lifetime. The fact that it was an external device that could be placed away from the microscope was also ideal when capturing images at large magnification over a period of time, as this prevented vibration from the cooling fan to disturb the capturing process.

4.1.6 Camera and Imaging Software

For capturing images of the displacement processes, Nikon Digital Sight DS-Fi1 high-definition color camera was installed on the microscope. This is a 5-megapixel CCD camera that can capture images of up to 2560 x 1920 pixels with 16 bit RGB pixel depth. The camera was controlled by a computer with Nikons NIS-Elements imaging software which could capture time-lapse image sequences. A capture rate of 1 frame per second could be achieved during image sequence capturing for images of 1280 x 960 pixels with 8bit RGB pixel depth.

4.1.7 Fluorescence Filters

Installed on the microscope were 3 fluorescence filters, each letting through different wavelengths of light. When mixing fluorescent additives with different fluids and selecting a suited fluorescence filter, it was possible to ensure that only the fluids of interest were visualized. Fluorescence was also used to get a better contrast between different fluids that normally would be hard to distinguish from each other, for instance water and oil, by adding fluorescent additives that emitted different wavelengths and appeared in different colors. The microscope was delivered with a bright light filter, and the two additional filters were installed for studying fluorescent water and fluorescent oil specifically. The filter suited for the wavelengths emitted from the fluorescent water will be referred to as the “blue” filter as the light appeared blue when passing through it, and the filter meant for the oil will be referred to as the “green” filter for the same reason.

4.2 Fluids and Fluorescent Additives

The fluids used in the experimental work and their fluorescent additives are listed in Table 2 below, and the physical properties of the fluids relevant for this study found in the literature, are listed in Table 3.

Table 2: Fluids and fluorescent additives used in the experimental work

Fluid phase	Fluid	Fluorescent additive
Liquid	Distilled water	Fluorescein, FT175
Liquid	Decane	Nile Red
Gas	CO_2	-
Gas	Air	-

Table 3: Viscosity and interfacial tensions found in the literature

Fluid	Viscosity [cP]	Interfacial Tension [mN/m]	Water	n-Decane	CO_2	Air
Water	1.002[1]	**Water**	-	52.00[4]	71.03[5]	72.88[3]
Decane	0.9135[1]	**Decane**	52.00[4]	-	22.45[6]	23.83[3]
CO_2	0.01469[1]	**CO_2**	71.03[5]	22.45[6]	-	1.190[3]
Air	0.01813[2]	**Air**	72.88[3]	23.83[3]	1.190[3]	-

[1](NIST Chemistry WebBook, 2012)
[2]Calculated from Sutherland's law (Sutherland, W., 1893)
[3](Jasper, J.J., 1972), IFT at 20 ^{o}C
[4](Johnson Jr, R.E. and Dettre, R.H., 1966), IFT at 24.5 ^{o}C
[5](Chun, B.-S. and Wilkinson, G.T., 1995), IFT at 25 ^{o}C
[6](Ayirala, S.C., Xu, W. and Rao, D.N., 2006), IFT at 37.8 ^{o}C

Since visualization of flow is the major advantage of the micromodels, making a good visual expression was of great importance. Different fluorescent additives were added to the injected fluids for this purpose. The fluorescent tracers of Fluorescein, FT175 and Nile Red were used, and their properties and applications are described below. Throughout the thesis, the term "water" will be used for distilled water, and if it contains a fluorescent additive it will be referred to as "fluorescent water". Which of the fluorescent additives it contains will be specified. N-decane will be used as the oil phase, hence, whenever the term "oil" is used this refers to n-decane. Experiments were conducted at ambient pressures and temperatures which meant that CO_2 was in a gas phase at all times, CO_2 gas will therefore be referred to simply as "CO_2".

4.2.1 Fluorescein

Fluorescein was added to the water for fluorescent effects. Mechanisms of fluorescence, including important effects as photobleaching and quenching of fluorescence, was reviewed by Williams and Bridges (Williams, R.T. and Bridges, J.W., 1964).

Fluorescein is the most common green fluorescent tracer, used in a wide range of applications and industries. Fluorescein is a powder which is soluble in water and alcohol and visible in concentrations as low as 0.005 ppm. It has a pH sensitive excitation and emission spectrum that peaks at 490 and 530 nm respectively, and the intensity of the fluorescence increases with increasing concentration up to a certain maximum (Kenneth G, R., 1982). The blue fluorescence filter installed on the Nikon

Eclipse inverted microscope was chosen for studying fluorescence caused by Fluorescein in particular.

One disadvantage of Fluorescein is that it has a relative high rate of photobleaching, which means that most of the fluorescence intensity gets reduced quickly when exposed to constant illumination. This limits the time one can study a specific area in the micromodels unless more unexposed water with Fluorescein is injected here. Another disadvantage that was observed during experimental work was that when mixed with water in a high concentration, it tended to accumulate in the pore network where the fluids entered from the injection channels, where it appeared as a separate phase insoluble in water. Mixing ratios ranging from 1:200 000 – 1:2 000 000 of Fluorescein/water were tested, and the optimal ratio with regards to photobleaching and retention was found to be 1:800 000.

Testing of different mixing ratios of water and Fluorescein was done in PDMS micromodels, models that will be described in section 4.3.1. These models were saturated with the fluorescent mixes and exposed to maximum illumination that the external light source could deliver. The models were viewed with the microscope using the 10x zoom objective lens using the blue fluorescent filter while the camera was capturing time lapse photos. Figure 7 and Figure 8 show the effect of photobleaching and retention for Fluorescein in a ratio of 1:200 000 and 1:800 000, respectively.

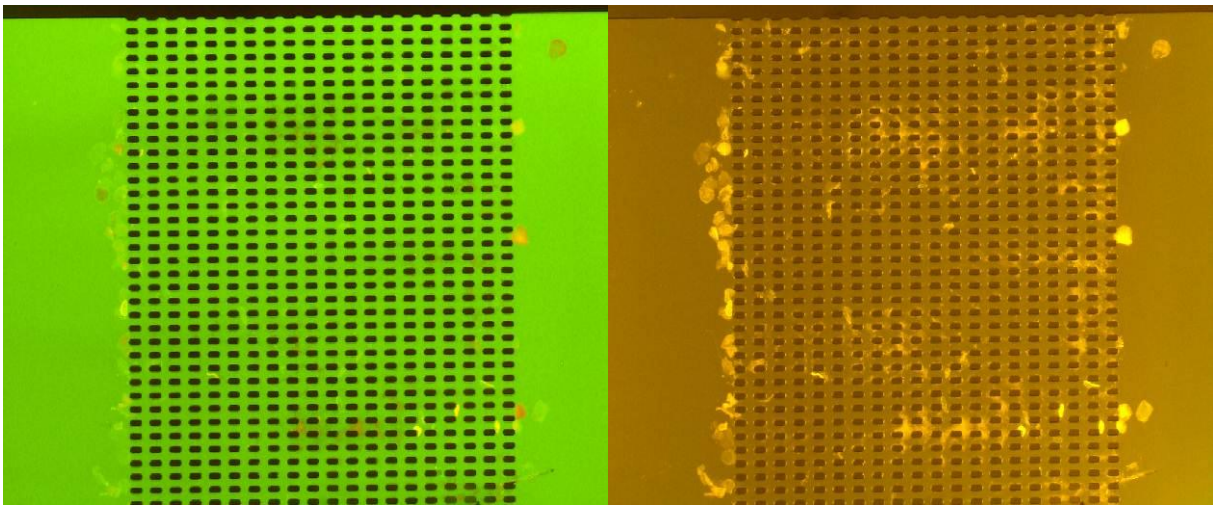

Figure 7ab: Fluorescein and water 1:200 000 mixing ratio, before and after 44 minutes of exposure to light. Grains in the micromodel appear black.

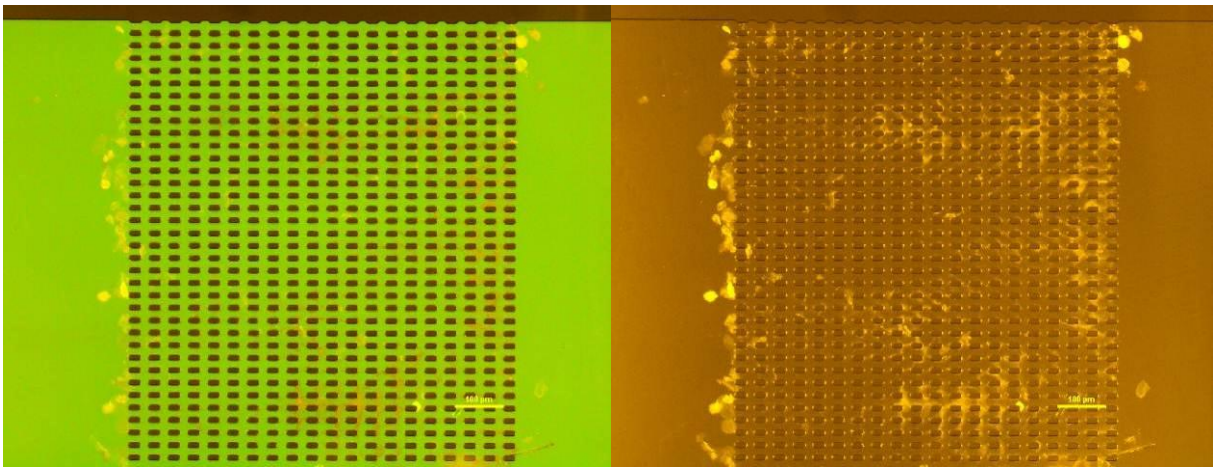

Figure 8ab: Fluorescein and water 1:800 000 mixing ratio, before and after 60 minutes of exposure to light.

As can be seen from the images above, both of the mixing ratios suffered from photobleaching after some time. In addition, Fluorescein accumulated in high concentrations, both at the inlet and outlet side of the pore network. The 1:200 000 mixing ratio gave the best fluorescent color initially, but also caused more accumulation of Fluorescein as it precipitated from the solution. This effect was less significant in the 1:800 000 mixing ratio while the initial fluorescent color were satisfactory.

4.2.2 FT175

FT175 is produced by the American Gas and Chemical Co. Ltd., and is a tracer dye commonly used for identifying water leakage in flow systems. The dye gives water an intense yellow-green color that when tested was found to fluorescence, and was clearly visualized with the blue fluorescence filter. The intensity of the fluorescence was kept for longer than that of Fluorescein when exposed to light. However, it was seen that particles of FT175 accumulated in decane, and it was suspected that this dye also affected interfacial tensions. It was therefore not used as frequently in flow experiments Fluorescein.

The FT175 that was received was a concentrated liquid dye of unknown concentration. As a consequence, the mixing ratio given here refers to the dilution of this concentrated mixture. It was not critical that the exact concentration of the solute in this mixture was unknown as different mixing ratios were tested before use to find the best suited one. Figure 9 shows the photobleaching test at a mixing ratio of 1:400 of FT175/water. The rate of photobleaching was lower for FT175, but after long time exposure the green fluorescent color was removed for these mixtures as well. Note that maximum light intensity was applied during these tests to speed up the photobleaching process. This intensity was never required in the experiments, and the rate of photobleaching was significantly slower when intensity was reduced.

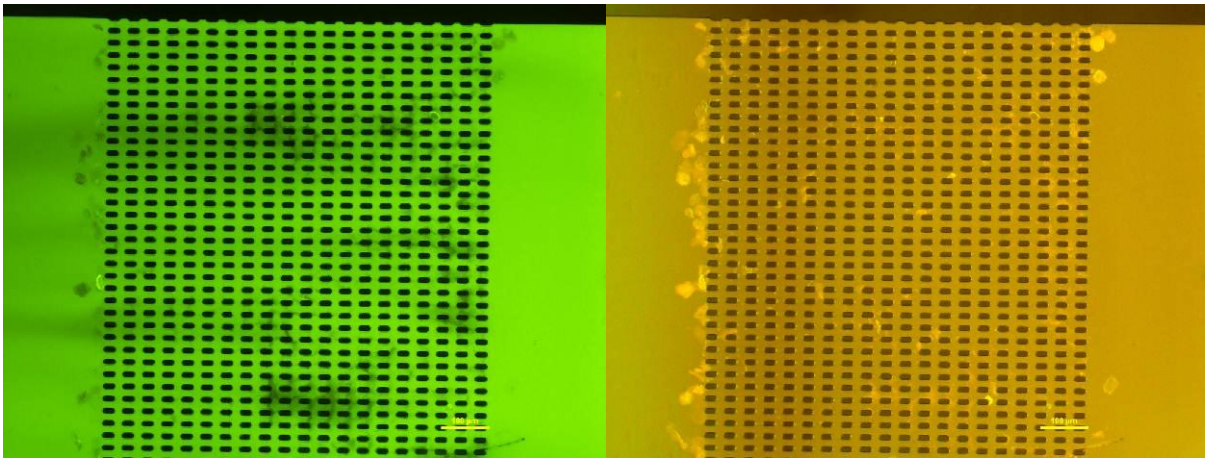

Figure 9ab: FT175 and water 1:400 mixing ratio, before and after 42 minutes of exposure to light.

4.2.3 Nile Red

Nile Red was the fluorescent additive used in the oil phase. Nile Red is soluble in organic solvents and hydrophobic lipids, and almost insoluble in water. Also, if Nile Red were to be found in an aqueous solution its fluorescence would be totally quenched (Fowler, S.D. and Greenspan, P., 1985a).

The excitation and emission spectra of Nile Red is highly dependent upon the solvent, and varies widely in both shape and intensity (Fowler, S.D. and Greenspan, P., 1985b). A result of this was that Nile red could be studied when using two of the different light filters on the microscope. When viewed using the green filter installed for the Nile Red emission spectra specifically, the oil containing

Nile Red appeared red. However, when using the blue filter, oil with Nile Red was also clearly identified as it appeared in a bronze like color. The fact that both fluorescent water and oil were visible when using the blue filter was very convenient for oil/water displacement processes as this made it easy to separate both of the phases from the grains without having to swap between filters.

Nile Red did also suffer from photobleaching when exposed to light over a period of time, but not as severe as Fluorescein. A mixing ratio of 1:100 000 Nile Red/decane was found to fluorescence satisfactory. Oil containing Nile Red in higher concentrations was found to leave high amount of Nile Red behind in the matrix possibly affecting flow patterns.

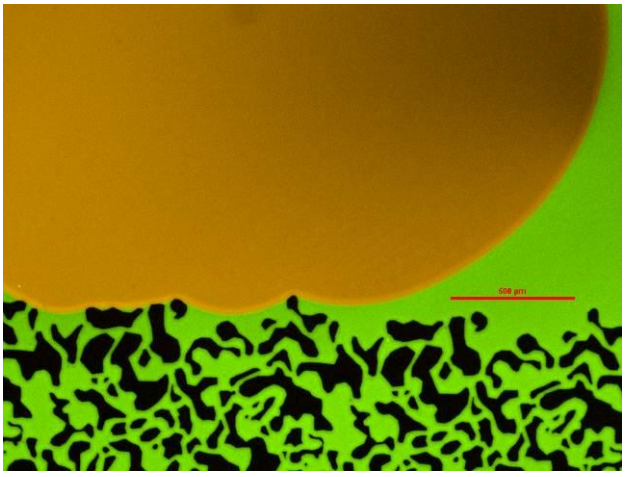

Figure 10: Oil with Nile Red entering the channel in a silicon micromodel filled with water with Fluorescein. Grains in the micromodel appear black.

4.3 Micromodels: Material and Manufacturing

In this thesis, two different types of micromodels were used. The simplest type had the pore network created in a rubber-like substance named Polydimethylsiloxane (PDMS). This substance is an organic polymer belonging to a group commonly referred to as “silicones” or “silicone oils” (Ecotoxicology, E.C.f. and Chemicals, T.o., 1994). The second type had the pore network etched in a silicon wafer and provided the most accurate representation of real porous media. Both of these model approaches had the pore network enclosed by bonding to a glass plate. More detailed descriptions of the models follow below.

4.3.1 PDMS Micromodels

The PDMS models used in this thesis was fabricated at Haukeland University Hospital in Bergen. The pore network was made in SU-8 photoresist which can provide a high-resolution pore structure where the height to width ratio of pores can be up to 20 with near vertical side walls. The SU-8 can achieve film thicknesses from 0.5 µm and up to approx. 200 µm (MicroChem SU-8 Data Sheet). Models of this type cannot represent pore structures found in real porous rocks in their true dimensions and physical properties, and the models used in this thesis were constructed with ordered pore structure that contained smaller pores and throats in comparison to real porous sandstone. They were therefore only used for testing the effect of changing the concentration of the fluorescent additives and how the intensity was reduced during illumination when changing the light intensity.

As a part of this thesis, a visit to Rice University in Houston was undertaken to take part in the manufacturing process of the PDMS micromodels used for flow experiments there. These models were constructed with procedures alike those at Haukeland, which will be described next.

Manufacturing of PDMS Micromodels

1. Silicon wafers were cleaned with ethanol and acetone, rinsed with DI water and put on a hot plate at 200 ^{o}C to dehydrate. This was performed to remove any unwanted particles attached to the wafer.

2. The wafers were coated with SU-8 photoresist in a spin coat process. By changing the rotation speed of the spin coater and the duration of the spin process, the film thickness of SU-8 could be varied as desired.

3. A two-step bake process was performed on a hot plate ensuring that the photoresist on the wafer solidified. The temperature was increased in two steps to prevent breakage of the film due to rapid temperature change, and was done by first increasing the temperature to 65 ^{o}C keeping it for 6 min and then increasing it to 95 ^{o}C for 20 min.

4. The desired pore structure was created digitally where channels, pores and other open areas were represented as white pixels while the rest was represented as black pixels. The image was exported to a computer connected to a UV-lithography machine with an automated stage, upon where the silicon wafer was placed with the photoresist-covered side up.

5. To create the pore structure, only the parts of the network that later would be the void areas in the micromodel were exposed to UV radiation. The exposure caused epoxy cross-linking of the SU-8 photoresist to start. This process was completed by performing a post exposure bake on a hotplate at 65 ^{o}C for 1 min and 95 ^{o}C for 5 min. Slow warming and cooling of the photoresist to avoid cracking of the film was of great importance at this stage.

6. Subsequently, the wafer was immersed in a developer for 6 min at room temperature, removing all photoresist that had not been exposed in the previous step. This left the channels and pores as a positive relief on the silicon wafer. Finally, the wafer was rinsed with isopropanol and air-dried. An additional hard bake at 170 ^{o}C for 5 min could be included after the wafer had dried if one wanted additional strength of the remaining SU-8, but was omitted here.

7. The next step was to transfer the pattern to models made of PDMS. The PDMS itself was made by mixing an elastomer with a curing agent in a 10:1 ratio, stir the mixture together and pour it over the silicon wafer. The desired thickness of the PDMS model was achieved by pressing it against the wafer that also ensured that the entire pore network was captured adequately. The wafer and the PDMS were put in a degassing chamber and evacuated for air during 20 min, and placed in an oven at 80 ^{o}C causing the PDMS to solidify. This process resulted in PDMS models with a cast of the pore structure on one of the sides.

8. The PDMS was cooled, removed from the wafer and cut to the desired shape of the micromodel. Holes for injection and production were cut by a needle designed for taking samples of biological tissue, having a diameter of 1/16th of an inch. Any residue or unwanted particles were removed simply by placing and removing scotch tape on the surface of the PDMS.

9. To complete the micromodel, closing of the network was done by bonding the PDMS to a glass plate. If wettability of the pore network was of importance, the glass plate would be covered by

a thin layer of PDMS as well by a spin coat and hot plate bake procedure. When this step was omitted, the channels and pores would have water wet surface against the glass plate and a more oil wet surface against the PDMS. How oil wet this surface would be depended on how the bonding procedure was performed. How the wettability could be controlled will be added as supplementary information at the end of this section.

Bonding of the PDMS to the glass plate was done by placing them both in a confined glass chamber, evacuate the air and treat them with oxygen plasma with a plasma cleaner. The oxygen plasma oxidized the surface of the PDMS causing it to bond irreversibly to the glass plate when taken out of the chamber and put together. The bond strength depended on the dose of the plasma treatment, and it was found that evacuating the glass chamber to 0.4 torr, which equals 0.00053 bars, before turning the plasma cleaner on at maximum power for 20 seconds was a decent dose for creating sufficient strong bonding. Maximum power gave the highest achievable amount of ions in the plasma reacting with the PDMS surface, and hence, the most efficient surface activation.

10. When the plasma treatment was finished, the PDMS was pressed against the glass plate, and the resulting model placed on a hot plate to ensure that the bonding process was complete.

As mentioned, the wettability of the PDMS could be changed from its natural hydrophobic state to a more hydrophilic state, making it possible to vary the contact angle between water and oil in the range of 15^{o} and 105^{o}. The degree of change in wetting angle depended on the plasma treatment dose; a greater dose made PDMS surface to a more water wet. However, the change in contact angle was rapid when using the plasma cleaner, so whenever control on the wettability was desired, an alternative treatment using a combination of UV light and ozone was used at Rice, and a paper for this method has been produced (Ma, K., Rivera, J., Hirasaki, G.J. and Biswal, S.L., 2011). Only water wet models were manufactured during the author's visit to Rice.

Properties of PDMS Micromodels

Only two PDMS models were used in this thesis. They consisted of a pore network of 79 x 20 grains with sizes of approximately 14.2 µm x 27.4 µm. The total network was of 1990 x 790 µm with a porosity of 73 %. As no flow experiments were performed in the PDMS models, permeability measurements were not performed. Figure 11 shows the pore network of a PDMS model with its dimensions.

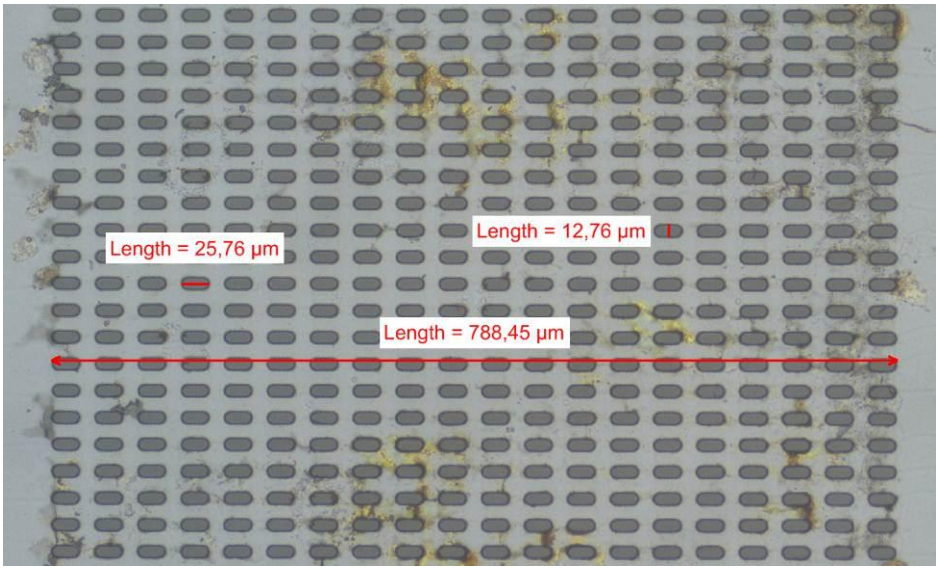

Figure 11: Ordered pore structure of a PDMS micromodel.

4.3.2 Silicon Micromodels

The silicon micromodels used in this thesis were fabricated at Stanford University, Stanford, California at the Stanford Nanofabrication Facility (SNF). The detailed construction process was developed by Hornbrook et al. (Hornbrook, J.W., Castanier, L.M. and Pettit, P.A., 1991), and the important steps in the construction procedure that makes these models superior to glass and PDMS models are described below.

Manufacturing of Silicon Micromodels

1. The pore structure was created from a thin section of a real rock. The thin section was taken at a high magnification to capture all the details, as for instance surface roughness of the grains, from a location in the rock where the resulting 2D image was assumed to best approximate the 3D pore structure.

2. A black and white image was created digitally at a high enough resolution that allowed for a 1:1 replica of the pores and grains found in the real rock. The resulting flow path was edited manually to ensure that the connectivity of the 3D rock was kept as best possible.

3. Construction of an image mask to transfer the pore pattern to the silicon wafer was made after the image manipulation. The image had also been made such that grains and flow paths would be continuous when stacking several images next to each other, and the final mask consisted of the image repeated in a 100 x 100 square.

4. The wafer was coated with photoresist, and the image mask was placed on top of it. The wafer was then exposed to UV light, destroying the parts of the photoresist not covered by the image mask.

5. Etching was performed by the same precise dry etch technique as in the microchips industry. The parts not covered by photoresist were etched to a wanted depth creating the pore bodies and throats. During the etching process the photoresist is also slowly destroyed so that when a deep etch is wanted a thick photoresist layer prior to etching is required. However, if one wants to avoid loss of detail on the grain surfaces, the photoresist cannot be made too thick, and hence, the possible depth of the pores and throats is limited as well.

6. Completion of the micromodel was done by anionic bonding to a glass plate, and drilling of holes for injection and production.

These micromodels can provide exact 2D replicas of any rock of interest, and with the precise etching techniques very small features can be constructed in great detail.

Properties of Silicon Micromodels

The construction procedure above is the general procedure that was followed at SNF. For the models used in this thesis specifically, the pore structure was created from Berea sandstone 2D thin sections. Two generations of micromodels constructed in this manner were used, the newest model have more detailed grain surfaces and a different pore design than the older. However, only one out of eight silicon micromodels were made of the new improved pore design. Prior to start of the experimental work the models were named to keep track of the different processes performed on

each model. The model of the newest design were named Berea A, the rest were given names of Berea B to Berea H.

Some physical properties of the micromodels were measured at the laboratory. For the properties that could not be measured, values received from the manufacturer will be used. Several papers have been produced where experiments on these micromodels have been conducted, and physical properties of the micromodels have been reported. One example is by Kovscek from 2007 (Kovscek, A.R., Tang, G.Q. and Radke, C.J., 2007).

Both of the pore network designs were constructed by repeating a 500 µm x 500 µm pattern 10 000 times resulting in a 5 cm x 5 cm size network of 600 by 600 pores. The dimension of the pore network meets the REV scaling requirements (Gu, J., 2010). The grain sizes range from 10 µm to 215 µm in Berea B - H and 8 µm to 415 µm in Berea A. Pore throats as narrow as 1 µm appear in both cases, but the average throat size is higher in the new design. For this reason, better conductance of fluids was allowed, resulting in a higher absolute permeability that better represented real Berea sandstone.

Two flow channels were etched along the length of the pore network with a width of 500 µm, one at each side of the pore network, connecting two and two ports where fluids could be injected or produced. The channels were also extended a short distance along the width of the pore network. The etch depth of the pore network and the flow channels were 25 µm. A sketch of the silicon micromodels can be seen in Figure 15.

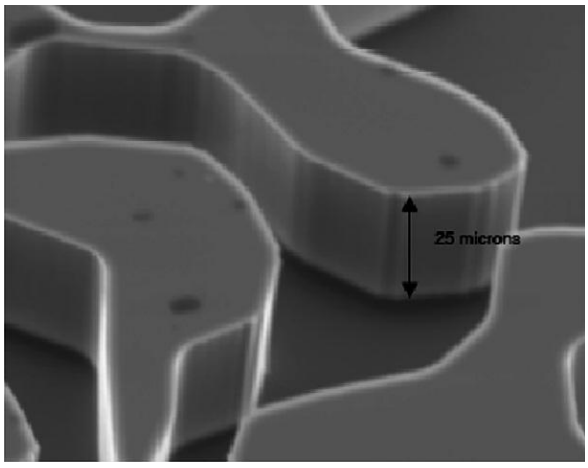

Figure 12: Close-up of scanning electron microscope image showing the etch depth of 25 µm (Kovscek, A.R., Tang, G.Q. and Radke, C.J., 2007).

Porosity and permeability for the micromodels were measured in the laboratory, and the way these measurements were conducted will be described in the experimental procedures in chapter 6. The returned porosity and permeability values from these measurements were given to the micromodels. Measuring the pore volume at the laboratory was not feasible as the additional volume of the injection/production ports and the space between the micromodel holder and the micromodels was many times larger than the actual pore volume of the micromodels. The pore volume will be the one provided by the manufacturer. Only values for the Berea B - H are given as Berea A cracked before these properties were measured, and were not found elsewhere.

Berea A:

1. Porosity 54 %

Berea B – Berea H:

2. Porosity 52 %
3. Matrix permeability 0.7 D
4. Fracture permeability 1,5 D
5. Volume of pore space 0.041 mL

Snapshots taken at 20x magnification from the two pore structures show a significant improvement in Berea A. During the etching process of this network, the rough surfaces of the grains found in real Berea rocks have been reproduced, while grains in Berea B - H were etched with smooth surfaces.

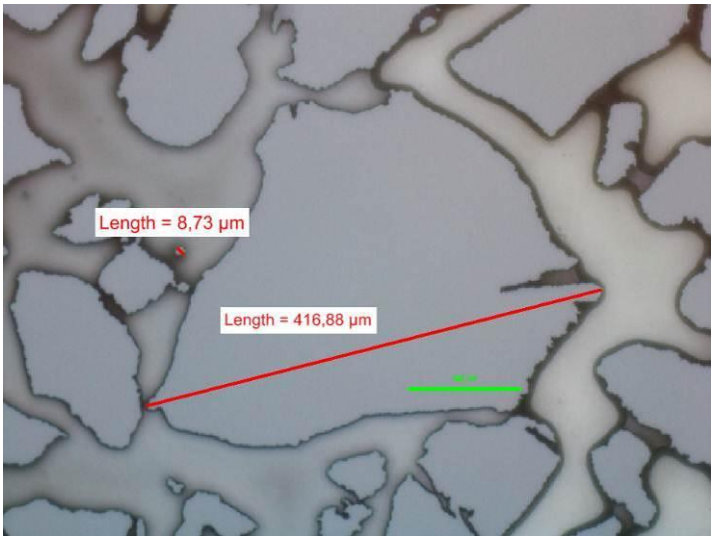

Figure 13: Image taken at 20x magnification of Berea A where surface roughness on the grains is included, showing the largest grain in the pore network.

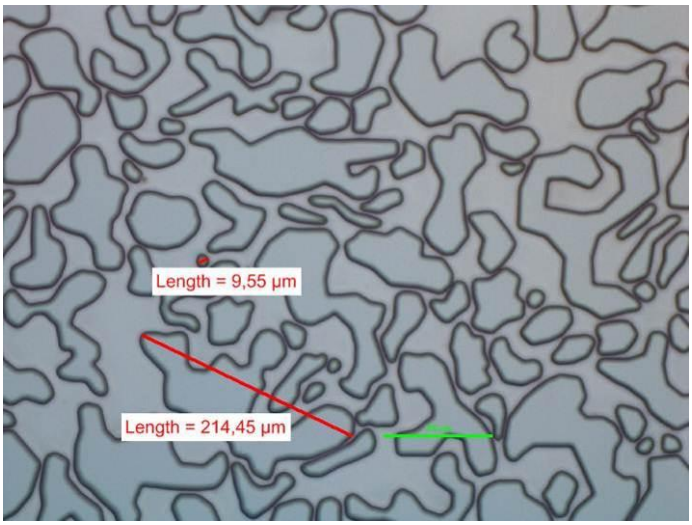

Figure 14: Image taken at 20x magnification of Berea D where grain surfaces are smooth. Both the largest and the smallest grains of the design are captured.

The flow channels of these micromodels were important for studying the effect of capillary forces in the displacement processes because of their large contact areas with the pore network. More displacement events occurred in this setting compared to models where injection was limited to a smaller area, for instance counter-current flow. Foam structure was also better visualized in the flow channels.

5 Experimental Procedures

In this section the experimental procedures are described in general. The individual experiments are presented in the experimental observations section, where boundary conditions, objectives, and experimental conditions will be explained in detail.

5.1 Boundary Flow Conditions

Boundary conditions were controlled by closing and opening different productions ports. The different combinations that were most frequently used and how displacement processes were affected will be presented below.

1. All ports open (later referred to as OPEN).

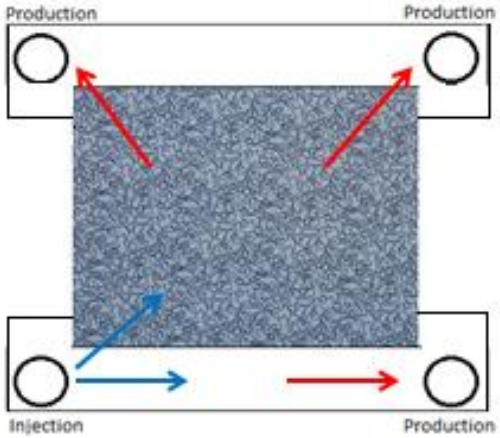

Figure 15: Open ports allowing for co-current and counter-current displacement from the matrix.

- The pressure drop across the matrix increased linearly with the injection pressure, and a large flow rate through the network could be achieved. Most of the displaced fluid escaped the model by co-current flow, meaning that it flowed in the same direction as the injected fluid

2. Closed ports in the opposite channel (closed opposite ports, COP).

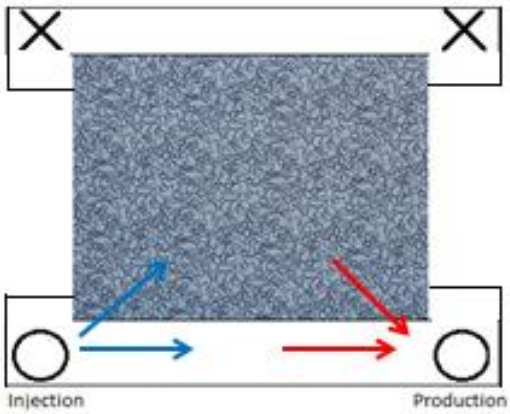

Figure 16: Closed opposite ports forcing counter-current displacement from the matrix.

- Only a small pressure gradient across the network could be achieved resulting from the flow in the injection channel and the fluid configurations in the pore space. Displaced fluid had to escape the model by counter-current flow, meaning that it flowed in the opposite direction of the injected fluid.

3. Closed port in the injection channel and open opposite ports (closed local port, CLP).

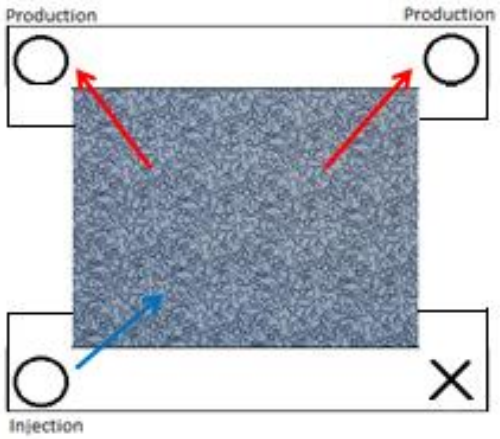

Figure 17: Closed port in the injection channel forcing co-current displacement from the matrix.

- The pressure gradient across the network was equal to the injection pressure, and fluids were displaced co-currently.

5.2 Water Imbibition

Water imbibition was performed to saturate the micromodels with water, to get a basic understanding of water–gas/water-oil displacement processes on the pore scale and to study the effect of the micromodels being water wet, causing water to spontaneously imbibe into the pore network. To see on what level viscous or capillary fingering was present was also important for comparison to larger scale experiments.

Water imbibition was studied in gas-filled micromodels (air or CO_2) in addition to oil-filled micromodels at irreducible water saturation, S_{wi}. Injection rates and boundary conditions were chosen depending on the flow mechanisms to be studied, and the injection pressure was measured continuously throughout injection. To avoid cracking of the micromodels the injection pressure was kept below 2 bars at all times.

During water imbibition experiments the boundary conditions were changed depending on the objective of the experiments between the two first configurations described in section 5.1:

- Water imbibition experiments were performed with all ports open (Figure 15) to study how water filled the micromodel at different injection rates.

    - If the injection rate of the water was lower than the imbibition rate into the matrix, the water spontaneously entered the matrix before the whole channel was filled.

    - If the injection rate of the water was higher than the imbibition rate into the matrix, the water filled the channel before entering the matrix.

- With closed ports in the production channel (Figure 16), capturing pore-level displacement processes were emphasized.

    - Water filled the matrix at a much lower rate making it easier to capture displacement processes that otherwise took only seconds to complete. For instance, end-effects in the opposite channel were easier studied with a slow advancing water front in the matrix.

    - The water always flowed in the channel before entering the matrix, as the air could only escape the matrix by flowing back into the channel where injection occurred through the production port.

5.2.1 Procedure for Saturating the Micromodels with Water

When the objective was to get the micromodels 100 % water saturated as fast as possible, an saturation procedure was followed, as no equipment for evacuating the micromodels without danger of cracking them existed at this point:

1. If oil were present in the micromodel prior to water injection, removing it was done by injecting CO_2 gas. This was done as water would not remove all the oil at the limiting pressure regimes. CO_2 gas, however, removed both water and oil even at very low injection pressures by injecting over a period of time, as it is slightly soluble in both water and decane.

2. Water injection was started with all ports open (Figure 15). The injection rate was set as high as possible in this step without exceeding the pressure limit of 2 bars to fill the easy accessible pore space.

3. When the production rate of air or CO_2 gas decreased, the port in the injection channel was closed (Figure 17) and water was forced into the porous structure. The injection rate was reduced so that the pressure still stayed below 2 bars.

4. Finally, the port in the production channel directly opposite of the injection port was closed to increase the sweep efficiency during waterflooding. Injection rate was reduced when necessary, and injection was continued until the micromodels were fully water saturated.

The whole process of saturating the micromodels with water took 3 – 5 days depending on whether the first step could be omitted. The models were filled to approx. 90 % water saturation in about a day, but displacing the last 10 % of the gas occupying the largest pores were a slow process.

5.2.2 Absolute Permeability Measurements

Permeability measurement of the silicon micromodels was performed by following the procedure below:

1. The micromodel was filled with distilled water to 100 % saturation.

2. Injection of distilled water was performed at 3 different injection rates delivered by the syringe pump, and the pressure drop across the flow length was measured at each rate.

3. The permeability was calculated from Equation 2 when using the depth of the pores times the length of the network as the cross-sectional area.

The absolute permeability of both the channel and the pore network was measured. The channel permeability was measured with all ports open (Figure 15) and the pore network permeability was found by closing only the port in the injection channel (Figure 17).

The values obtained from these permeability measurements were assumed to be representative for all the micromodels of the same design, the models Berea B – Berea H. For the model Berea A permeability measurement was not performed as the model cracked during an early experiment. However, the permeability of this model was seen to be much higher than the rest as higher injection rates could be applied while still keeping the pressure below 2 bars.

5.2.3 Porosity Measurements

Porosity of the micromodels was calculated by an image analysis procedure:

1. The micromodel was filled with fluorescent water to 100 % saturation.

2. Images were taken at 10x and 5x magnification with the blue filter.

3. The image was converted to a binary image with the image processing software ImageJ, so that grains appeared black and the pores and channels originally filled with green fluorescent water appeared white.

4. The ratio of white pixels to total number of pixels was produced, giving the porosity of the micromodel.

5. Estimating the porosity was done by averaging the values obtained from 3 different models at both magnifications.

Uncertainties in the estimated porosity arise from the resolution of the images and from where in the pore network the images are taken. The resolution of the images affected the position and thickness of the grain wall, and photos were taken with the highest quality of 2560 x 1920 pixels to minimize the uncertainty of the grain boundaries. Figure 18 show a binary image that has been created from a photo taken at 5x magnification in one of the models. The image has been further zoomed in on such that the resolution of the grain walls can be better seen. The large rectangle in the upper left corner represents the whole image at 5x magnification and the smaller rectangle shows the section that has been zoomed in on.

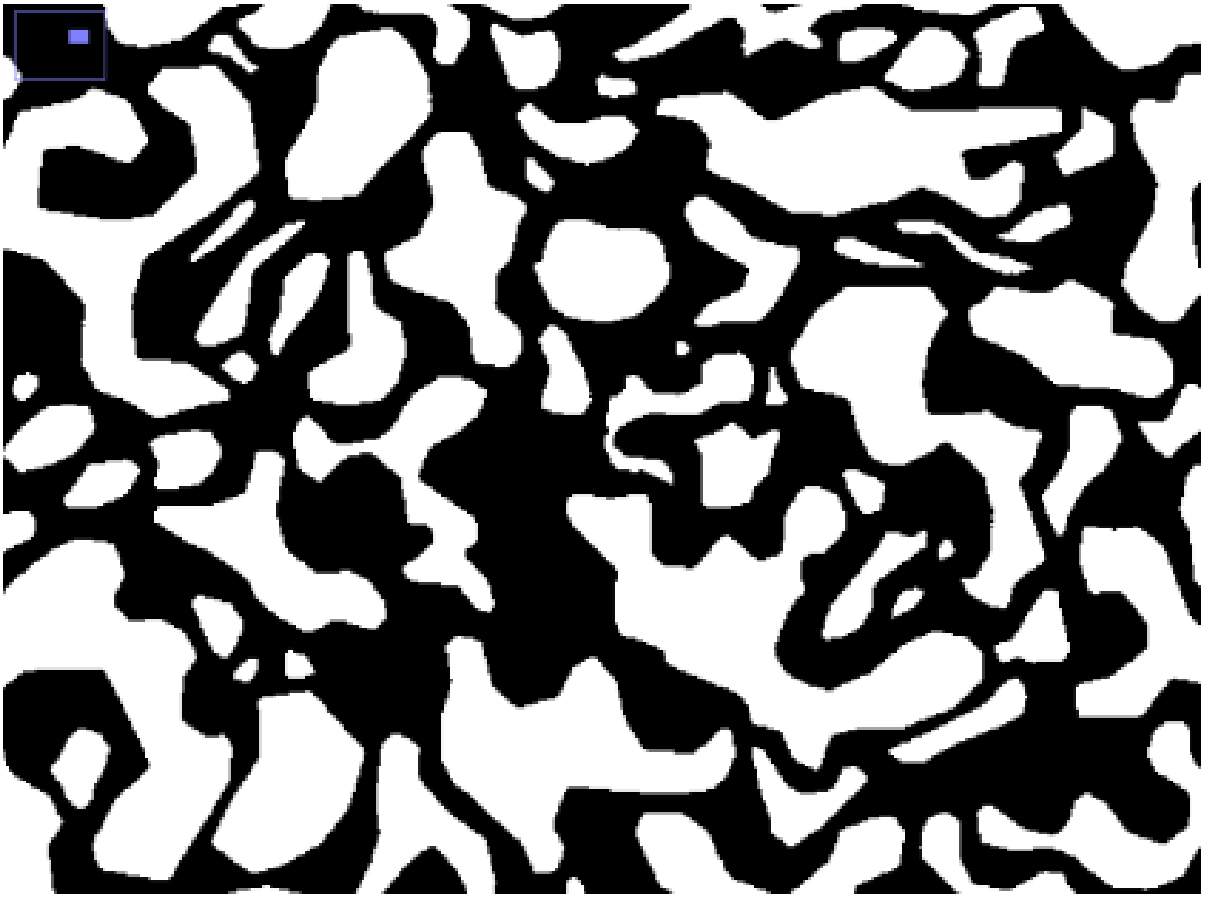

Figure 18: Section of a binary image created for porosity calculations.

5.3 Primary Drainage

Primary drainage was performed on 100 % water saturated micromodels to study the oil-water displacement processes occurring during oil migration into natural water-filled reservoirs. It was also done to investigate the threshold pressure for oil to invade the matrix in the silicon micromodels. Performing primary drainage after water imbibition was also important before carrying out subsequent experiments in order to reproduce the fluid saturation history and obtain the same fluid settings found in real oil reservoirs.

As for imbibition experiments, primary drainage was performed with varying boundary conditions.

- Primary drainage with the opposite ports closed (Figure 16) was performed to minimize the differential pressure across the matrix and prevent oil from invading.
    - If oil did enter at these conditions, viscous forces of the oil flowing in the channel where high enough to overcome the capillary pressure to displace the water counter-currently from the matrix.
- Primary drainage was performed with all ports open (Figure 15) at different injection rates to study viscous fingering and general displacement pattern.
    - Water flowed both counter-currently and co-currently in the micromodel. When oil was injected into 100 % water saturated models the threshold pressure for oil to enter the matrix was found by increasing injection rate stepwise until invasion of oil was observed. The pressure before and after invasion of oil then gave the interval of the threshold pressure.

When the purpose was to reach maximum oil saturation and irreducible water saturation the same procedure as described in steps 1 – 4 in section 5.2.1 was followed, injecting oil instead of water.

5.3.1 Saturation Measurements

Measurement of fluid saturations when two or more fluids were present was done in ImageJ in a similar manner as when porosity was measured. With two fluids present, at least one of the two had to be fluorescent, and with three fluids, two had to be fluorescent, in order to obtain the necessary fluid contrasts.

While the analyzed image was converted to a binary image during porosity measurements, color thresholding were applied during saturation measurements. This made it possible to apply constant values to pixels in the areas occupied by the fluorescent fluids, and then a simple pixel count gave the fluid occupations in the images. The total fluid volume was then found by either continued color thresholding to tag the non-fluorescent fluid, or by multiplying the total pixel count with the previously estimated porosity. Both methods had their pros and cons; color thresholding tagged pixels of the matrix grains while some of the non-fluorescent fluid still were unmarked, and the estimated porosity were made for the models as a whole, not the selected areas where the images were taken.

Figure 19ab show an example of color thresholding applied to a snap-shot image from a micromodel occupied by oil with Nile Red and water with Fluorescein. It can be seen that even water films could be separated from oil by this method.

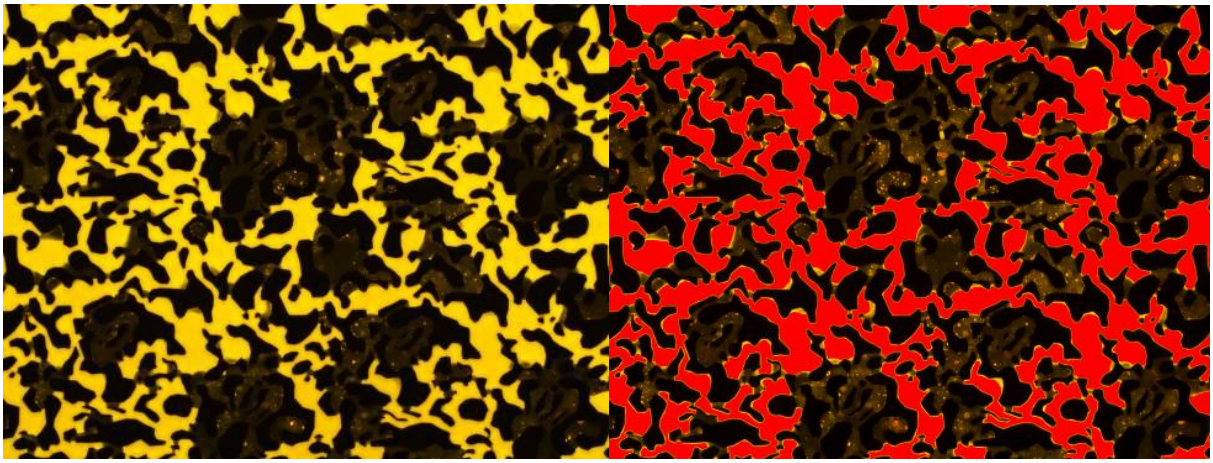

Figure 19ab: To the left is an original image taken with the blue filter, and to the right, the same image where color thresholding has been applied.

5.4 CO_2 Gas Injection

CO_2 gas injection was performed on both 100 % water saturated and partially oil and water saturated micromodels. CO_2 gas injection was performed on water saturated micromodels to study the two-phase gas/water displacement processes, and on oil and water saturated micromodels to study 3-phase displacement processes, sweep efficiency and to compare the results to water injection as a secondary recovery process. Capturing and describing the displacement processes, both during two-phase and three-phase flow, was emphasized in the experiments.

Displacement of oil and water by CO_2 was a combination of both bulk displacement and diffusive processes, and the importance of these was studied by changing the boundary conditions in the same manner as during the imbibition and drainage experiments.

- With all ports open (Figure 15) the combined bulk and diffusive displacements were studied.
    - A significant differential pressure existed across the network, and the CO_2 gas could displace fluids by co-current flow. Less resistance for bulk displacement existed and this displacement mechanism was dominating.
- With opposite ports closed (Figure 16) bulk processes occurred at a much slower rate and the importance of diffusive processes could be investigated.
    - Bulk displacement of fluids by CO_2 gas mostly occurred in the area close to the injection channel while diffusive processes were increasingly important with increasing distance from the channel.

6 Experimental Results

This section describes the microscopic and macroscopic flow phenomena that were observed during different drainage and imbibition experiments. Many of the experiments were basic experiments where fundamental processes were studied, as they were the very first experiments performed at the newly established microfluidic laboratory. Verifying that different displacement processes occurred and could be visualized in the micromodels was as important for subsequent EOR experiments. Only parts of the pore network were captured in a single microscope image. As a consequence many of the processes during the experiments were repeated several times to fully understand the displacement mechanisms.

The results from the micromodel experiments are arranged by processes in a natural order, the order that had to be followed when performing the experiments at the laboratory. They will be presented starting with water imbibition, followed by primary drainage, before EOR processes are described. All experiments were performed with the micromodels in a horizontal position to reduce the effect of gravitational forces at ambient pressures and temperatures. All of the experimental images were captured with the micromodels in the same position: the injection channel was at the bottom and the production channel was at the top. Fluids were injected from bottom left, and depending on boundary conditions main production was towards the top, or towards the bottom right.

6.1 Spontaneous Imbibition

6.1.1 Initially Stable Radial Displacement

Spontaneous imbibition was performed in air-filled Berea B by injecting distilled water without fluorescent additives. Water was injected at an initial rate of 1 mL/h, and opposite ports were closed forcing counter-current displacement of air. At this rate and boundary conditions, a low Δp across the matrix was expected.

Table 4: Experimental specifics for spontaneous imbibition

Micromodel	Fluid in model	Injected fluid	Fluorescence	Injection rate	Boundary conditions
Berea B	Air	Water	-	1.0 mL/h	COP

When water entered the micromodel it filled the channel before imbibing into the matrix (Figure 20), where it displaced air in a radial pattern moving away from the injection port with a stable front (Figure 21). Water was hard to distinguish from air in the matrix due to lack of fluorescence, but the grains around the pores occupied by water were coated with water films making the grain walls appear thicker. A dotted white line illustrates the position of the water front in Figure 21. Water displaced air by a pore-to-pore filling mechanism where only a few pores and the surrounding throats were filled each time the water advanced. This did not occur in a continuous manner, but rather in pulses with a minor delay between each pore filling event. The pores were also filled in an even manner such that the radial front had almost the same distance from the injection port along the entire length. At the same time, water invaded the matrix in other parts along the injection channel by the same evenly distributed pore-to-pore filling mechanism (shown from a different experiment under similar conditions in Figure 22). No viscous or capillary fingering was observed early in the imbibition process meaning that only some of the largest air-filled pores were bypassed in the area swept by water, and the residual air saturation was low.

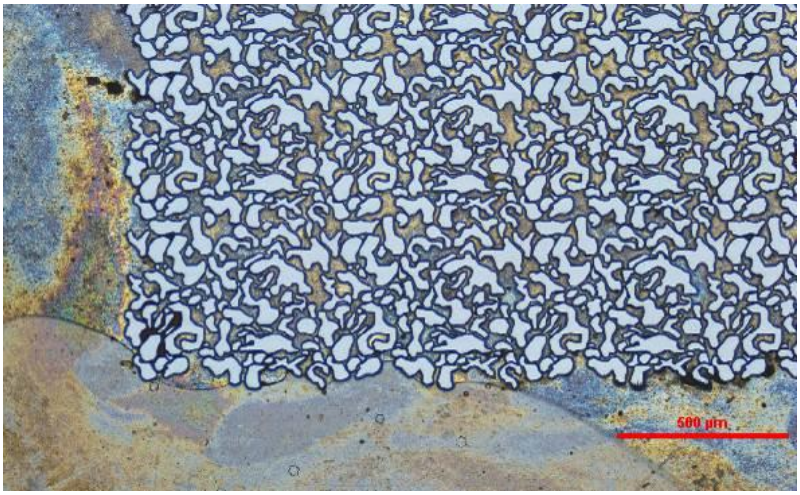

Figure 20: Water filling the channel before entering the matrix.

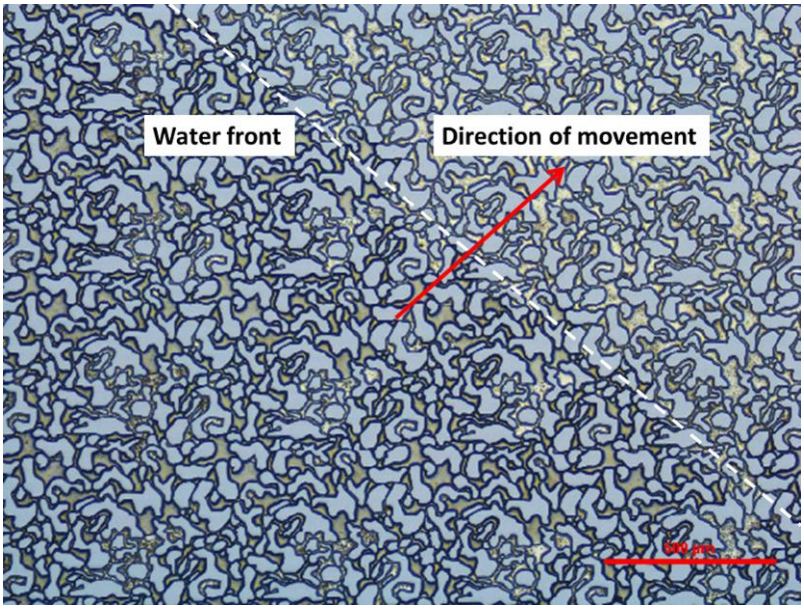

Figure 21: Water front advancing through the matrix displacing the air in a radial pattern away from the injection port.

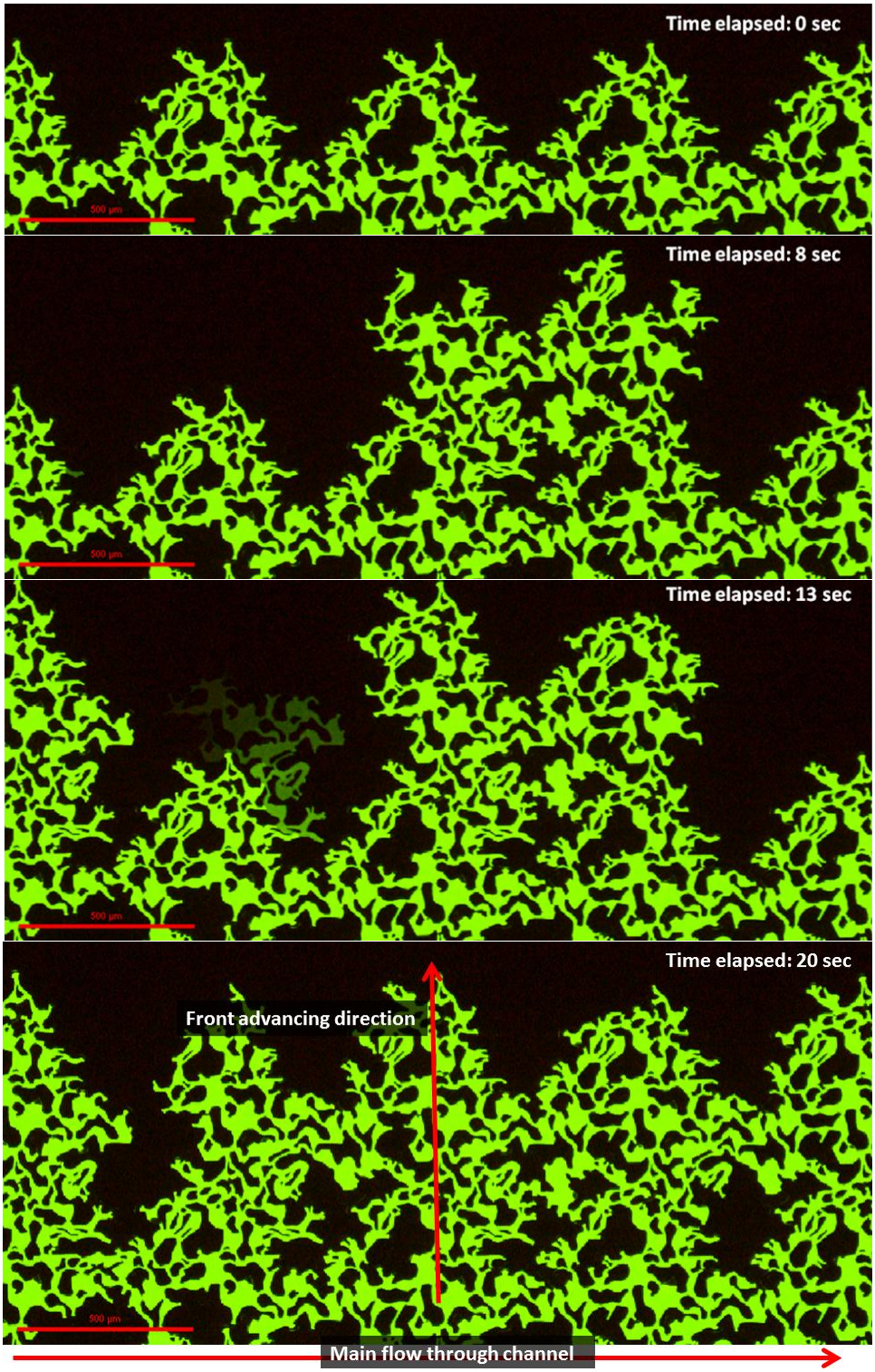

Figure 22abcd: Water front advancing through the matrix displacing air close to the injection channel.

The rate was increased to 2 ml/h and it was observed that water fingers developed both from the radial front and from areas along the injection channel where water had entered the matrix. The water fingers advancing from the middle of the matrix eventually advanced further than the water fingers originating from the radial front. Large volumes of air were bypassed in the matrix as the fingers advanced rapid towards the production channel without sweeping much of the pore space. Breakthrough of water to the air-filled production channel at the opposite side of the micromodel was by one of the large water fingers advancing from the middle of the matrix close to the point of injection. Air saturation was larger than 50 % at breakthrough. The large water finger that reached

the production channel is shown in Figure 23 where white dotted lines indicate the location of the water in the image.

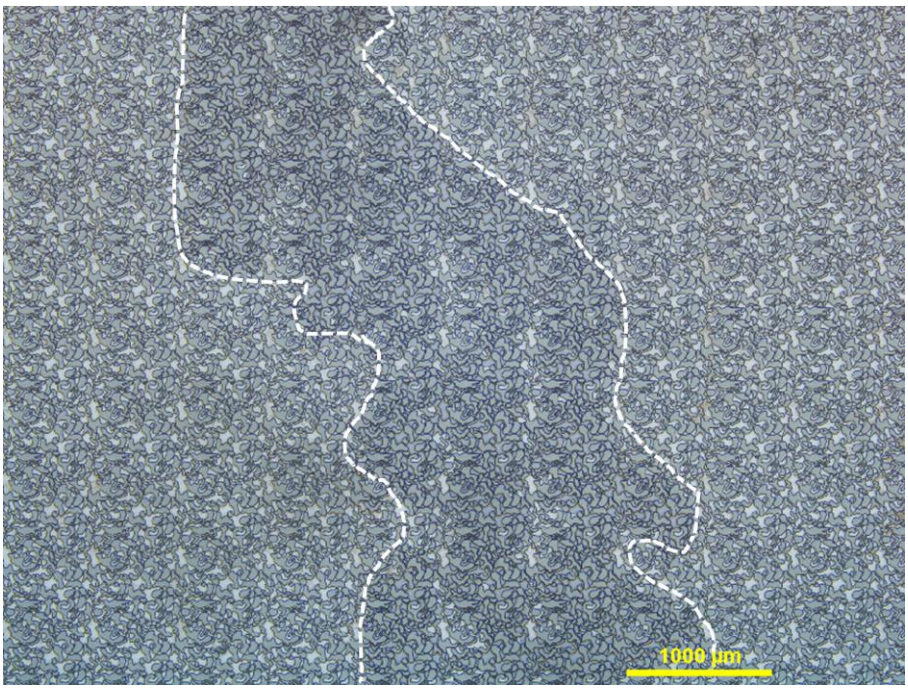

Figure 23: Large water finger developing during spontaneous imbibition, eventually reaching the production channel.

Water imbibition into air-filled pores continued after water breakthrough, even into pores occupied by discontinuous air. Water was not seen to invade air-filled pores by capillary imbibition from the production channel back into the matrix. The air phase remained continuous through an air path to the bottom right corner where air could escape. As a result, obtaining 100 % water saturation required several pore volumes of injected water.

The location where water entered the production channel was observed through the microscope, and details of the displacement could be visualized. When water reached the production channel it stopped at the edge of the matrix. This hold up of the water phase was a capillary pressure phenomenon as a result of the transition from a small pore space to an area of, in comparison, infinite size, referred to as end-effects. Figure 24 show the water advancement. Left: a water finger reaches the channel. Right: after 12 seconds water breakthrough in the channel occurs.

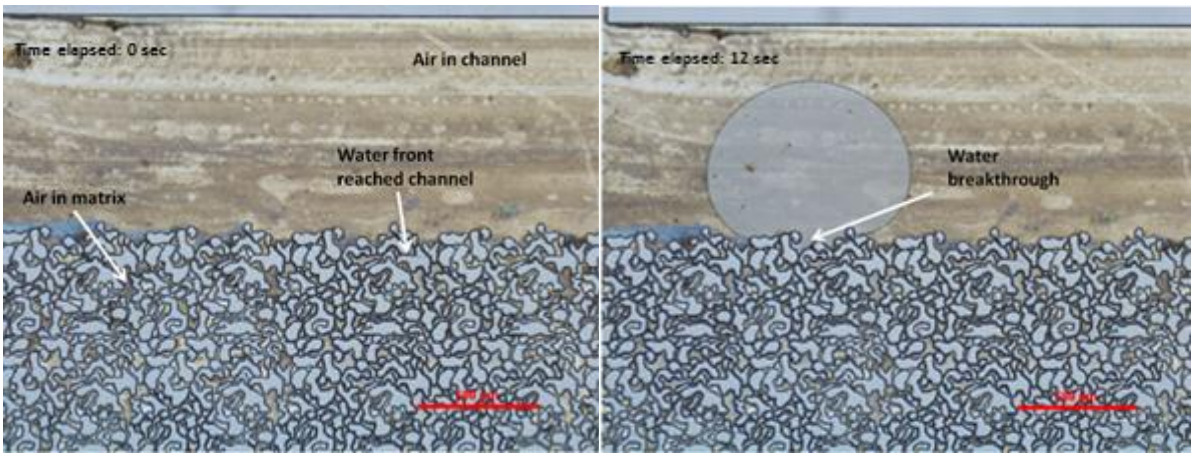

Figure 24ab: End-effects holding up the water phase in the transition zone between matrix and channel.

6.1.2 Immediate Unstable Capillary Fingering

Spontaneous imbibition was performed in micromodel Berea D by injecting fluorescent water when the model was filled with CO_2 gas with all ports open at an injection rate of 0.5 mL/h. Flow was studied through the blue fluorescence filter, which prevented the possibility to separate CO_2 from the matrix grains except where water filled the complete pore space.

Table 5: Experimental specifics for spontaneous imbibition

Micromodel	Fluid in model	Injected fluid	Fluorescence	Injection rate	Boundary conditions
Berea D	CO_2 gas	Water	FT175 1:400	0.5 mL/h	OPEN

A drop of oil from a previous experiment entered the micromodel from the NPT fitting unintentionally prior to water, possibly affecting the displacement process to some degree in the vicinity of the injection port. When water entered the micromodel this oil was pushed into the matrix at the bottom left corner while water filled the channel. Imbibition into the matrix was initiated in several places along the length of the channel, and almost immediately did a long water finger develop on the left side of the network which advanced straight towards the opposite channel. This water finger is shown in Figure 25, which has been created by combining three snap-shot photos into one large image. The injection channel was just below the area captured in the image, and was captured approximately 20 seconds after water initially imbibed into the matrix, indicating the speed of the advancing water finger.

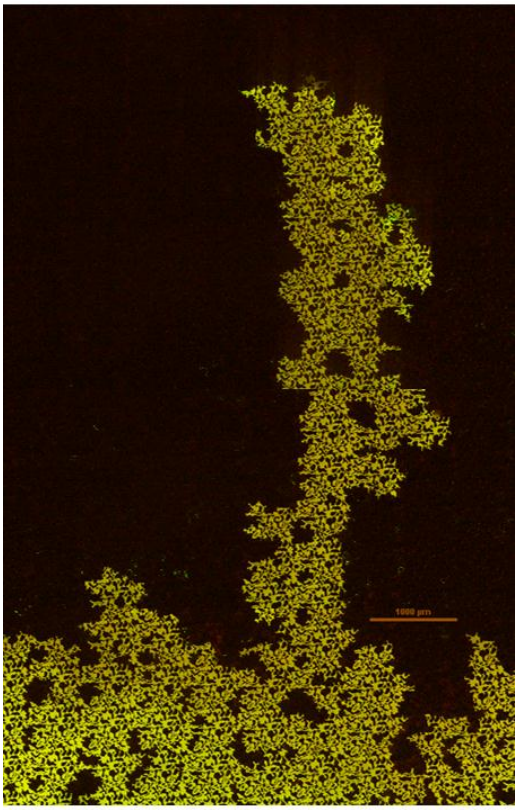

Figure 25: A large water finger developed immediately after water imbibed into the matrix.

No stable radial moving front was observed in the matrix in this experiment as was in the experiment described in section 6.1.1. Instead, many water fingers advanced in a chaotic pattern through the matrix. These water fingers also advanced by filling clusters of pores in a pulse-like manner, but the pulses occurred more frequently with less delay between each pulse, and the clusters that were filled were many times larger compared to those during a radial displacement. The rapid advancement of

water fingers made the total displacement rate of CO_2 from the matrix high as they existed over most of the length of the pore network. Merging of large water fingers and trapping of large areas of CO_2 occurred occasionally, which left a high residual CO_2 saturation in the matrix at breakthrough. Displacement of trapped discontinuous CO_2 areas was also observed. The image sequences in Figure 26 and Figure 27 show capillary fingers advancing normal to, and even in the opposite direction of, the main flow direction, showing the chaotic imbibition pattern. Figure 28abc show the slow imbibition of water into a large cluster of pores occupied by discontinuous CO_2. Even though water was injected from bottom left, imbibition of the cluster occurred both from the top and the bottom. CO_2 was not observed to displace water by double displacement mechanisms in any nearby location as the water advanced into trapped clusters, indicating that the water advanced by compression and dissolution of CO_2.

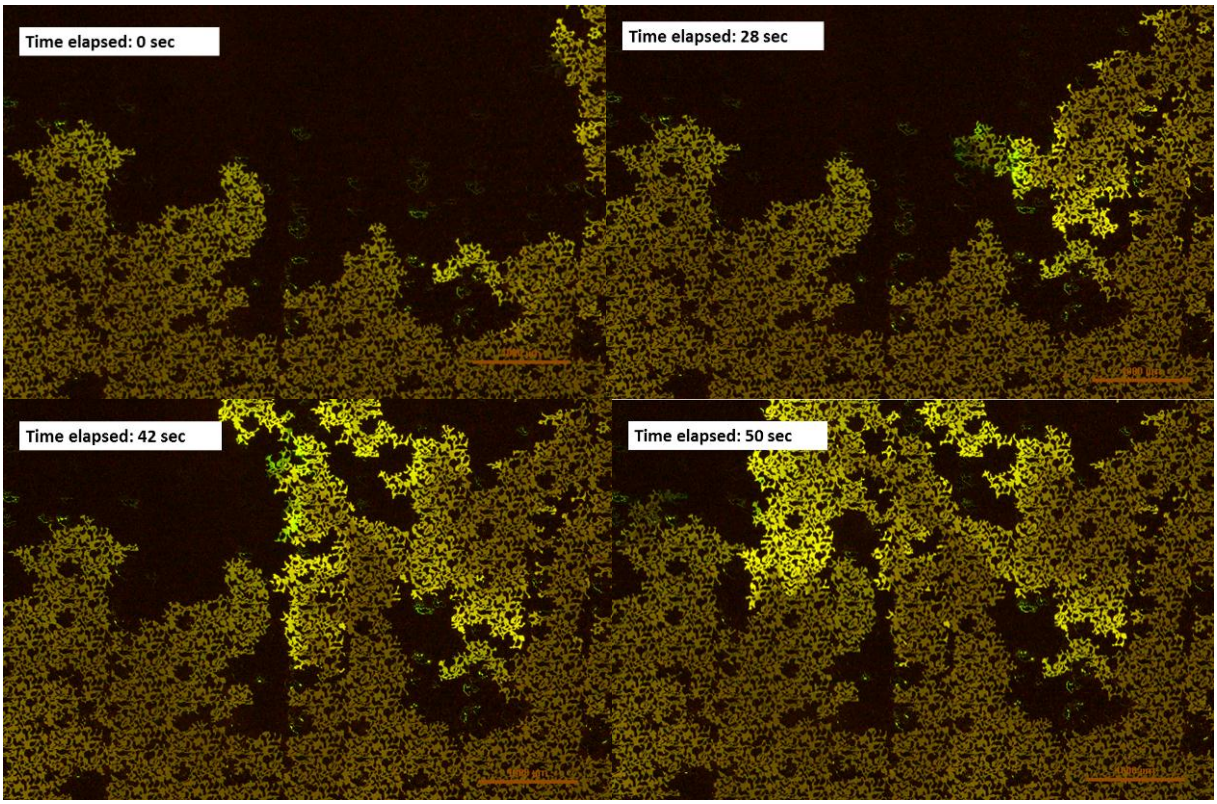

Figure 26abcd: Capillary finger advancing normal to the main flow direction.

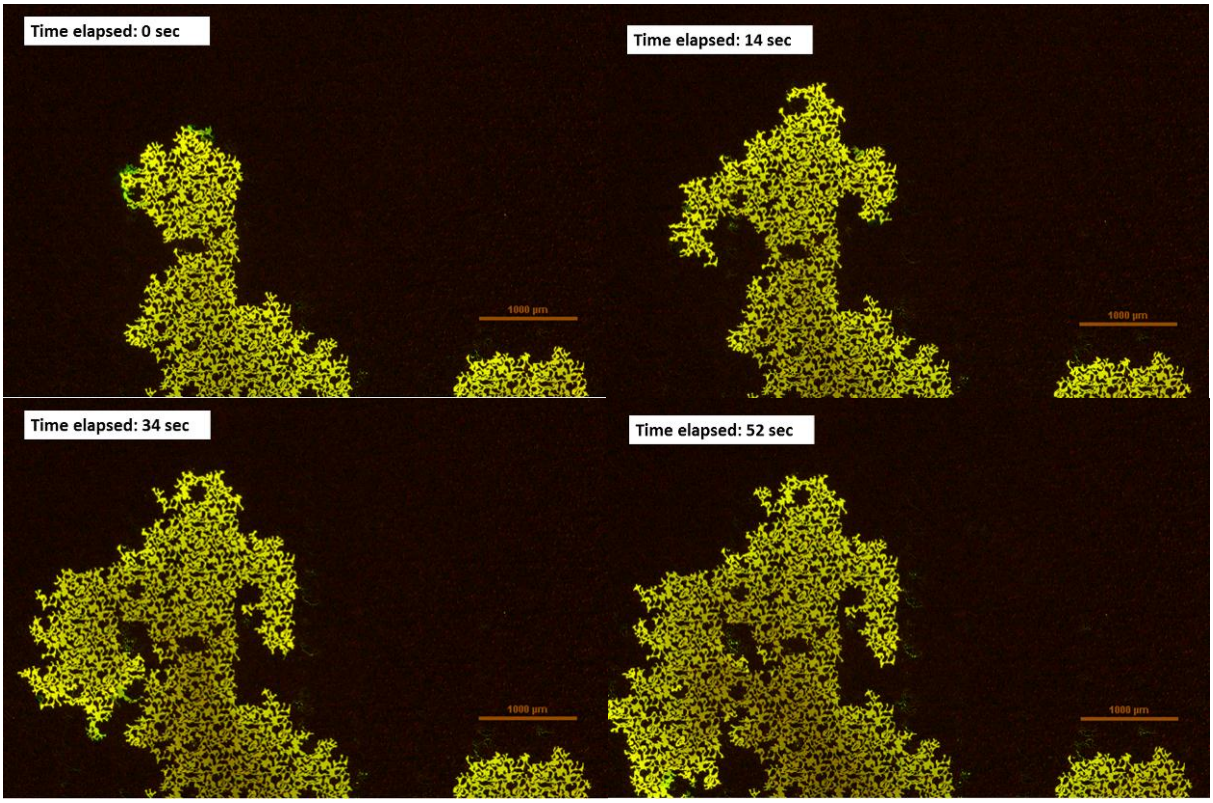

Figure 27abcd: Capillary finger advancing in the opposite direction of the main flow.

Water reached the production channel first through one of the water fingers when the CO_2 saturation was high in the matrix. Capillary hold up of the water phase was not observed as water flowed straight into the production channel (Figure 29a). Water in the channel imbibed back into the matrix in some locations, filling a few pores before coming to a halt (Figure 29b). After water breakthrough in the production channel CO_2 production continued at a reduced rate. Water fingers were still advancing in the matrix, and as trapped clusters of CO_2-filled pores were imbibed by water, the displacement was still efficient until large parts of the matrix had been filled.

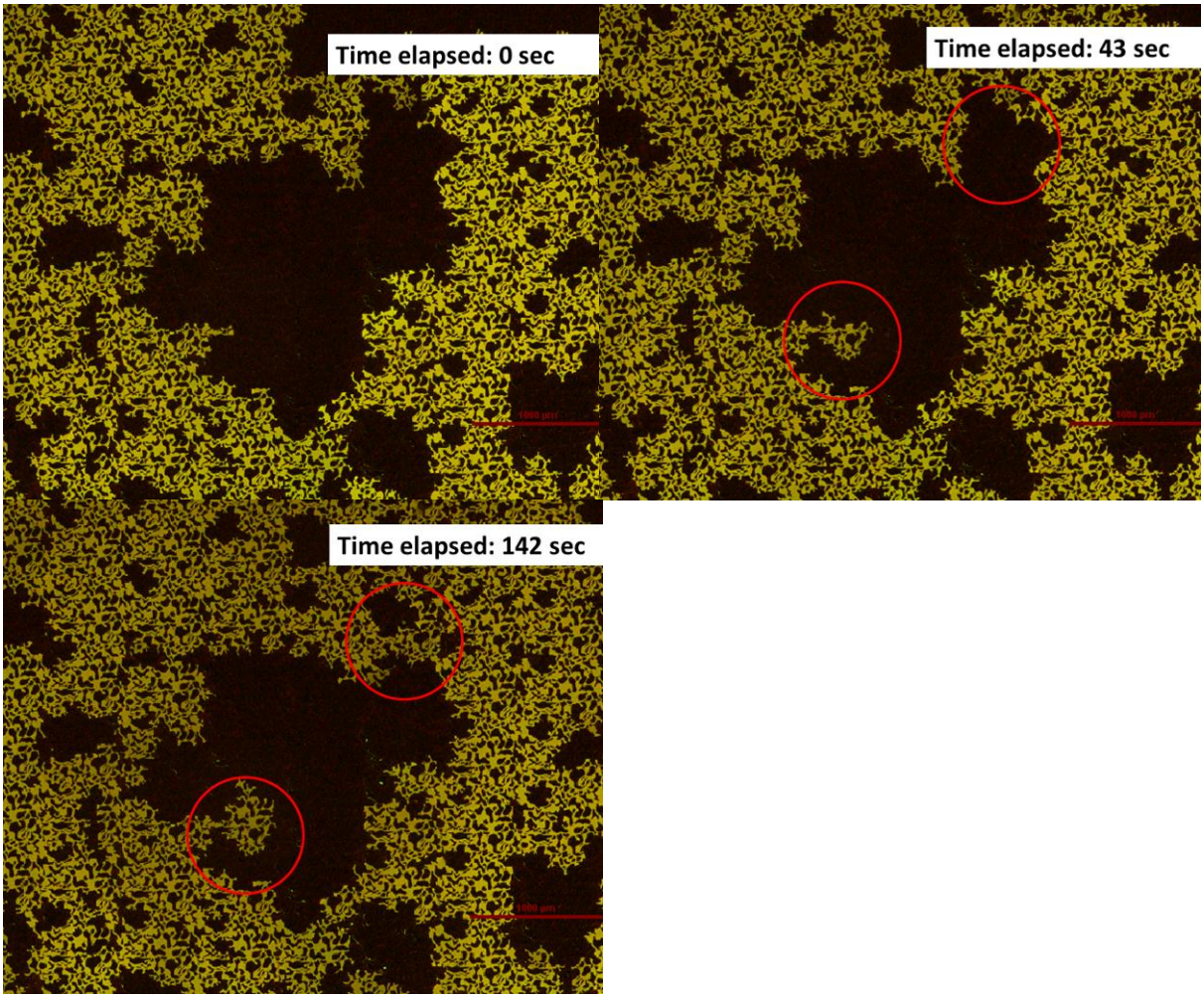

Figure 28abc: Water displacing trapped CO_2.

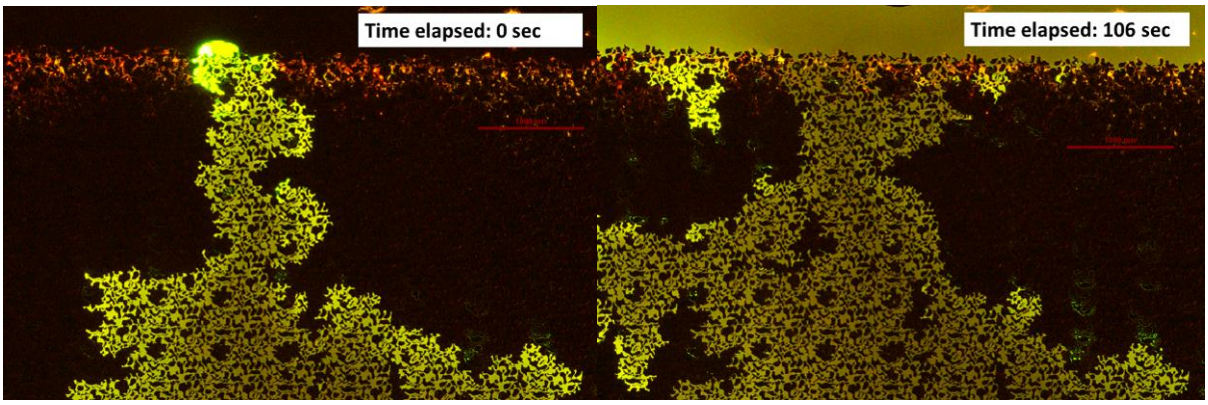

Figure 29ab: Water reentering the matrix from the channel near the initial breakthrough.

6.1.3 Water/Gas Displacement Mechanisms

Immediate capillary fingering was observed during spontaneous imbibition in air-filled micromodel Berea D. Fluorescent water was injected at a constant rate of 0.5 mL/h with all ports open.

Table 6: Experimental specifics for spontaneous imbibition

Micromodel	Fluid in model	Injected fluid	Fluorescence	Injection rate	Boundary conditions
Berea D	Air	Water	Fluorescein 1:200 000	0.5 mL/h	OPEN

The water finger pattern appeared immediately when water entered the matrix, similar to the previous spontaneous imbibition experiment described in section 6.1.3. The irregular finger pattern during water advancement left large amounts of trapped air in the network. Initially, air could escape the micromodel through continuous flow paths to the production channel through co-current flow, and counter-current flow of air to the water-filled injection channel was not observed. Figure 30ab show a capillary finger that displaced air counter-currently in the matrix towards the injection channel, without air entering the channel. Later however, it was observed that air was displaced to the injection channel when water completely surrounded and entrapped it, and no escape path through the matrix was easy accessible. In order to flow to the production channel it would have to flow through numerous connected water fingers, and thus escaping to the bottom channel was easier. Trapped air escaping to the bottom channel is shown in Figure 31 and it can be seen that water flowing in the channel from left to right directed the air towards the production port.

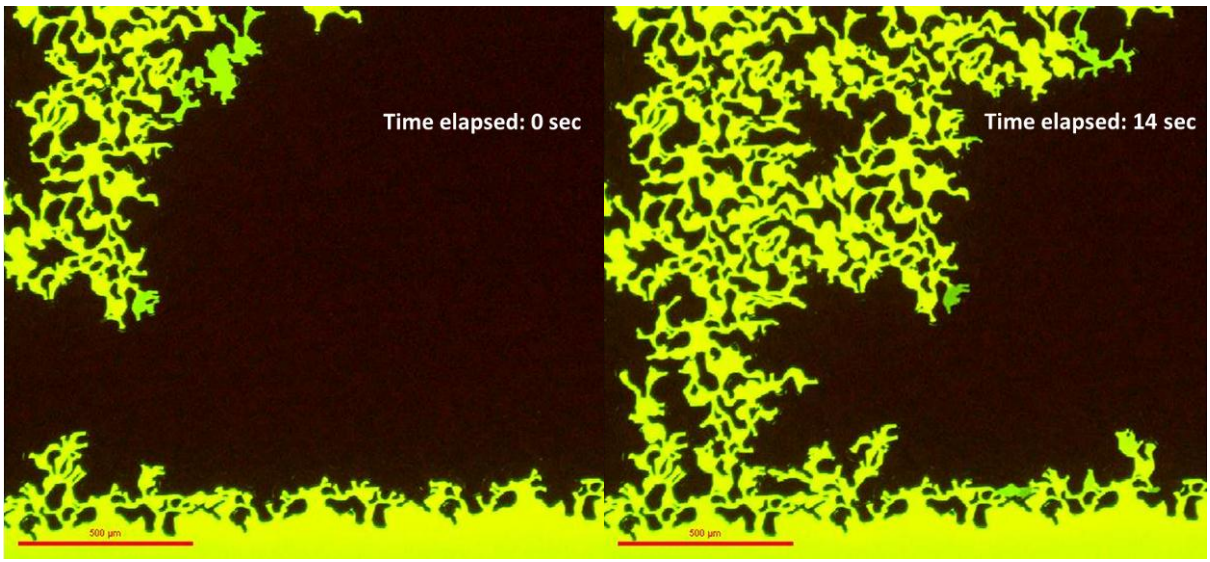

Figure 30ab: Water displacing air counter-currently in the matrix by capillary fingering without air entering the water-filled injection channel.

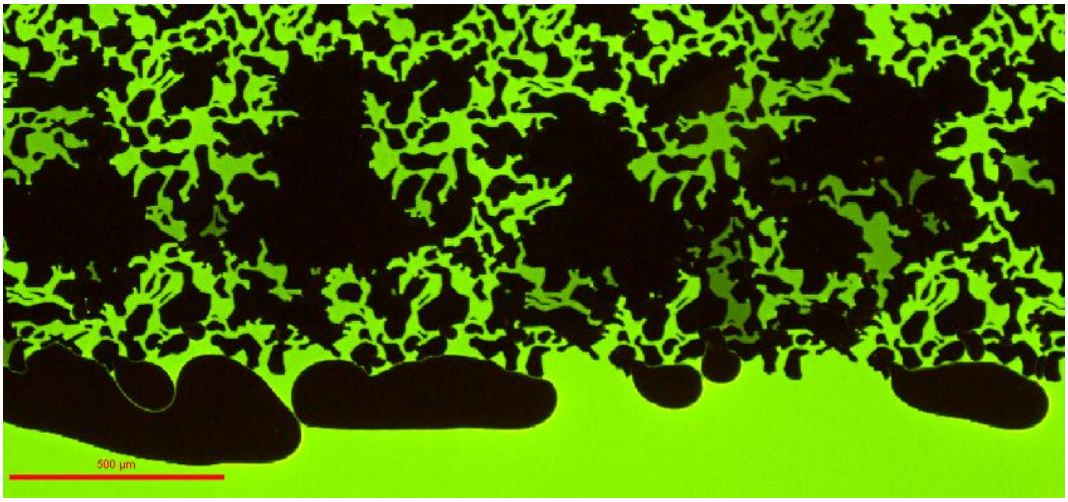

Figure 31: Discontinuous air displaced by water counter-currently to the injection channel.

The air entering the injection channel in Figure 31 flowed from larger, bypassed air-filled clusters of pores, and the bubbles expanded slowly as the air flow to the channel was continuously. Eventually, only small, discontinuous air bubbles existed in the matrix and the continuous flow of air stopped. The last remaining air was then removed by two processes:

- As single gas bubbles displaced to the channel
- By diffusive processes and dissolution into the water phase

Displacement of single gas bubbles to the channel was the main mechanism initially. This did not mean that dissolution was not contributing early in the displacement process: both events were present during the entire experiment, but bubble displacement was more dominant at higher air saturations. Bubbles advanced through the matrix by movement that alternated between stagnation and rapid jumps and "popped" out of the matrix in an instant movement when they reached the channel. The last pores filled with air, however, were capillary trapped in the matrix and not displaced to the channel. A higher water phase pressure would be required in order to mobilize the last bubbles of air, and as this was not obtained, dissolution was the only way to reach 100 % water saturation.

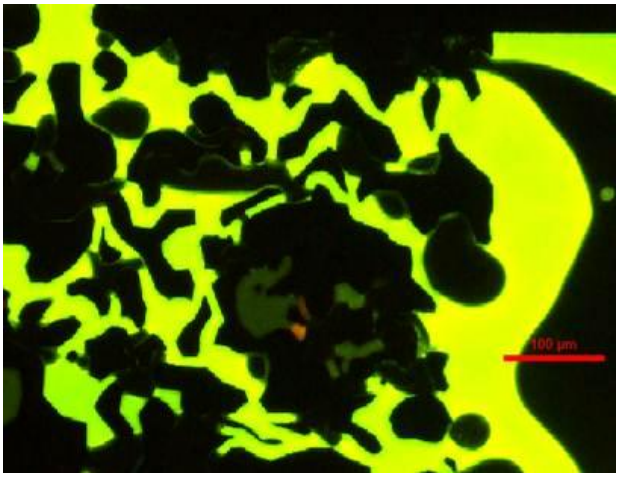

Figure 32: Displacement of air as isolated bubbles to the injection channel on the right edge of the pore network.

The dissolution rate of air was very slow, however, and finding an appropriate time interval to capture images of the process was difficult. Either nothing happened between two images, or all air

was dissolved from one image to the next. Another experiment was therefore performed where CO_2 was used as the gas phase and focus was on capturing the dissolution process. This experiment is described in the following section.

The amount of CO_2 dissolved in water at 25 ^{o}C and 1 atm (≈1 bar) is 1.45g/L, while the concentration of air in water is 0.023 g/L at the same conditions (www.engineeringtoolbox.com, 2012). Hence, removing the CO_2 by dissolution was expected to be much faster than dissolution of air in the equivalent experiment. Therefore, micromodel Berea D was filled with CO_2, and fluorescent water was injected with all ports open.

Table 7: Experimental specifics for spontaneous imbibition

Micromodel	Fluid in model	Injected fluid	Fluorescence	Injection rate	Boundary conditions
Berea D	CO_2 gas	Water	Fluorescein 1:800 000	2.0 mL/h	OPEN

The dissolution rate increased with CO_2, and the process was captured when images were taken two seconds apart. Dissolution of CO_2 into the water phase is shown in Figure 33a-d, where images were taken at a fixed position in the matrix at 20x magnification. Both grains and CO_2 gas bubbles appeared black, but were easily distinguished from another in the vicinity of water due to water films coating the grains. The CO_2 was dissolved in a few minutes in the selected area, and the model reached 100 % water saturation in a shorter time compared to when air was the displaced fluid.

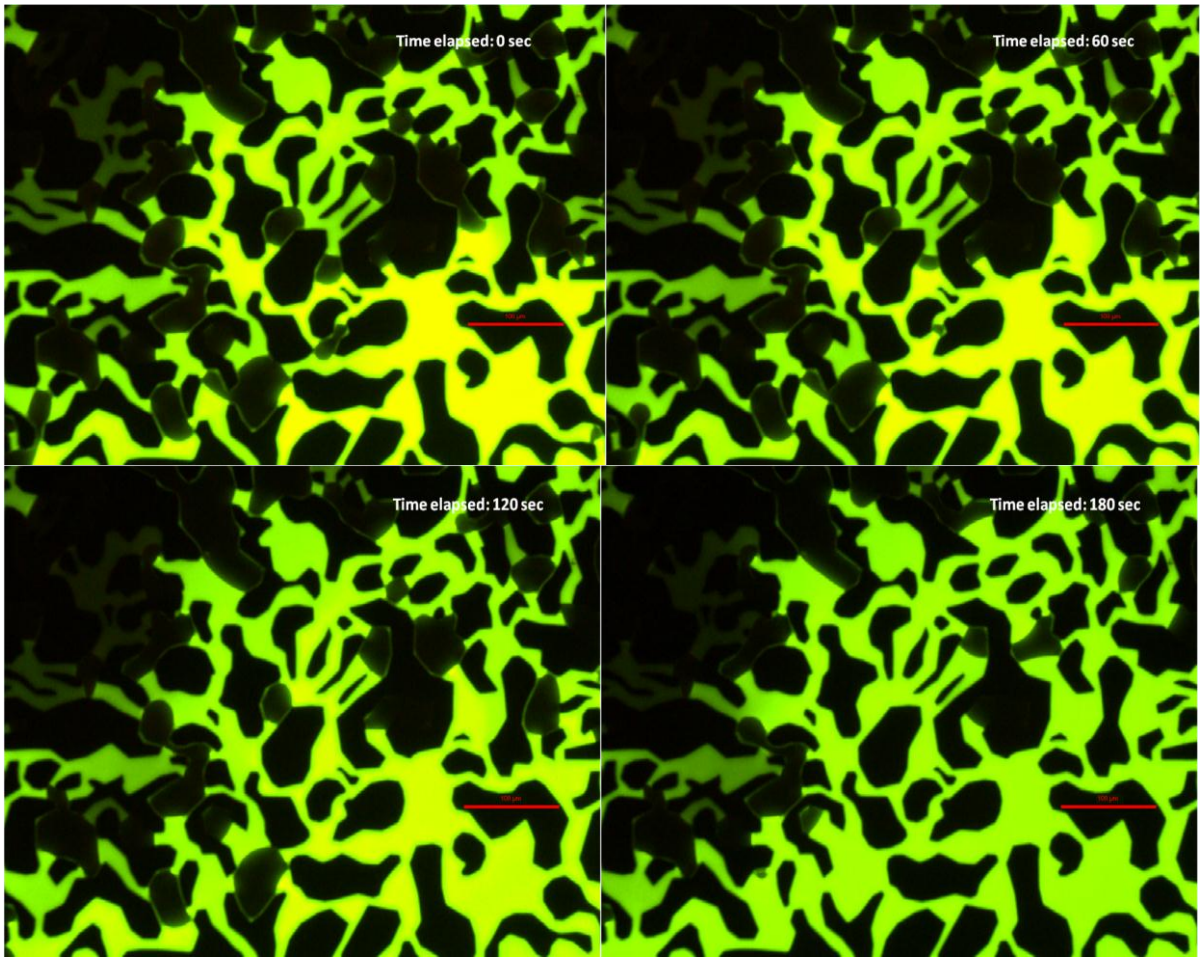

Figure 33abcd: Dissolution of CO_2 gas in the matrix during water injection.

6.2 Primary Drainage with Oil

6.2.1 Threshold Pressure Measurement

Oil does not invade a water-wet matrix unless the viscous forces applied exceed the capillary threshold pressure. Finding the capillary threshold pressure where sufficiently large viscous forces existed for oil to invade the matrix was attempted in several primary drainage experiments, but as this value was found to be very low, only some were successful. One of these was a primary drainage experiment in micromodel Berea F saturated with fluorescent water. The opposite ports were closed before injection was initiated, and oil was injected at an initial rate of 0.5 mL/h.

Table 8: Experimental specifics for threshold pressure measurement during primary drainage with oil

Micromodel	Fluid in model	Injected fluid	Fluorescence	Injection rate	Boundary conditions
Berea F	Water	Oil	Fluorescein 1:800 000	Stepwise increased	OPEN

As oil reached the injection port in the NPT fitting the pressure increased to 0.27 bars, which dropped to 0.10 bars when oil entered the micromodel and filled the injection channel without entering the matrix. The injection rate was reduced to 0.1 mL/h corresponding to a pressure of 0.06 bars before the opposite ports were opened. The rate was maintained until a stable pressure was recorded, and increased stepwise until oil entered the matrix at 4 mL/h, corresponding to a pressure of 0.27 bars.

Figure 34ab show images taken at 2x magnification before and after oil entered the matrix. In the first image oil was seen to fill the injection channel with water in the matrix. Retention of fluorescent additives was seen in the entrance zone of the matrix from the channel, possibly affecting the threshold pressure measurement. Figure 34b was taken after oil had entered the matrix. A repeated drainage pattern of oil appeared when it entered the matrix, and the causes for this pattern will be discussed in later sections of primary drainage experiments.

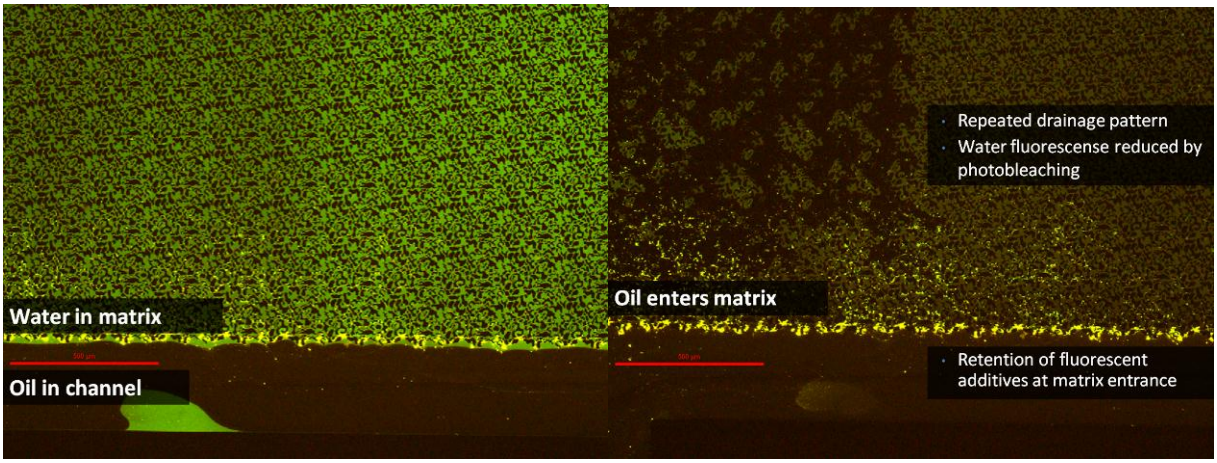

Figure 34ab: Images taken before (left) and after (right) oil entered the matrix during threshold pressure measurement in Berea F.

6.2.2 Developed Capillary Fingering

The large flow pattern and sweep efficiency during primary drainage determined the irreducible water saturation, and therefore also the maximum oil saturation. Several experiments were performed where the larger flow pattern was observed, but unfortunately, a hard drive failure limited the available experimental images to support the observations described in this section.

Primary drainage was performed in micromodel Berea G saturated with water with all ports open. Oil was injected at a constant rate of 1 mL/h and entered the matrix immediately after filling the injection channel.

Table 9: Experimental specifics for primary drainage with oil

Micromodel	Fluid in model	Injected fluid	Fluorescence	Injection rate	Boundary conditions
Berea G	Water	Oil	Fluorescein 1:800 000 Nile Red 1:500 000	1.0 mL/h	OPEN

The initially displacement pattern showed good macroscopic sweep in the matrix from bottom left towards top right, but a significant volume water remained in the swept area as some small water-filled throats were not invaded causing clusters of water-filled pores to be trapped. The drainage pattern was repeated in the matrix in that the same pores were swept by oil, indicating that a preferred pore filling pattern for the oil existed, controlled by capillary pressure. As oil injection continued, the macroscopic sweep efficiency became poorer as oil fingers developed. These oil fingers reached the opposite channel at an early point when the water saturation in the micromodel still was high. The flowing nature of these oil fingers resembled that of capillary fingers, as they advanced in all directions and swept larger areas than what was typical for viscous fingers. The displaced water was mainly produced into the production channel, but some water production was also observed in the injection channel. The remaining water saturation after the oilflood was measured to 37.9 %. Figure 35 shows the fluid configuration after oil injection in the selected area during calculation of fluid saturations taken at 10x magnification. The water phase has been tagged red, oil is yellow and grains are black.

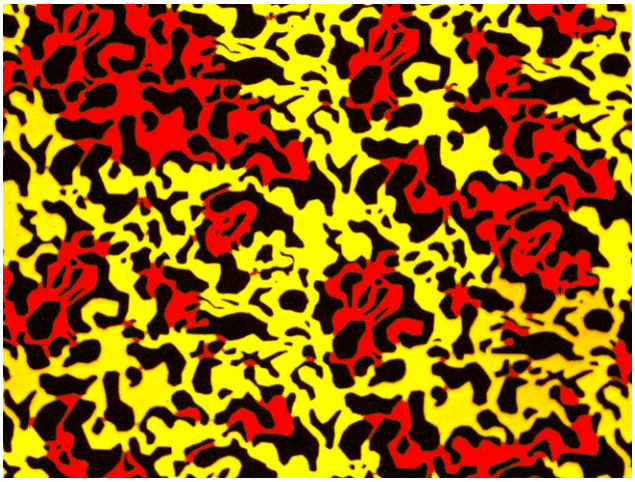

Figure 35: Color thresholding for calculation of fluid saturations in an area swept by oil.

6.2.3 Developed Capillary Fingering

Primary drainage was performed in water saturated micromodel Berea G using a constant injection rate of 1 ml/h. The opposite ports were closed during the entire experiment, forcing counter-current displacement of water.

Table 10: Experimental specifics for primary drainage with oil

Micromodel	Fluid in model	Injected fluid	Fluorescence	Injection rate	Boundary conditions
Berea G	Water	Oil	Fluorescein 1:200 000 Nile Red 1:100 000	1.0 mL/h	COP

After filling the injection channel, oil entered the matrix when the pressure exceeded the threshold pressure. The displacement of water in the matrix was by a pulse-like filling mechanism where oil invaded clusters of pores in discrete jumps. The clusters were filled evenly in a radial pattern moving away from the injection port with no observed fingering, and an oil front was observed in the matrix. The overall filling mechanism was therefore slow and stable, while the individual cluster filling was varying between stagnation and instant jumps. Figure 36a-d show the radial displacement pattern as oil advanced in the matrix. Only a few clusters were filled in the 38 seconds between the first and the last images were captured showing that the displacement process was fairly slow, and these clusters were filled evenly distributed such that the front advanced stably. Invasion of oil into the matrix along other parts of the injection channel, as was seen in spontaneous imbibition experiments, was not observed in this experiment. However, the oil front eventually adopted a concave shape in the matrix as the oil front advanced slightly faster along both the edge of the pore network towards the production channel (can be seen in Figure 36a-d), as well as along the injection channel in the matrix. Oil in the matrix and in the injection channel was seen to connect in some locations creating new continuous oil paths where oil continued to advance into the matrix.

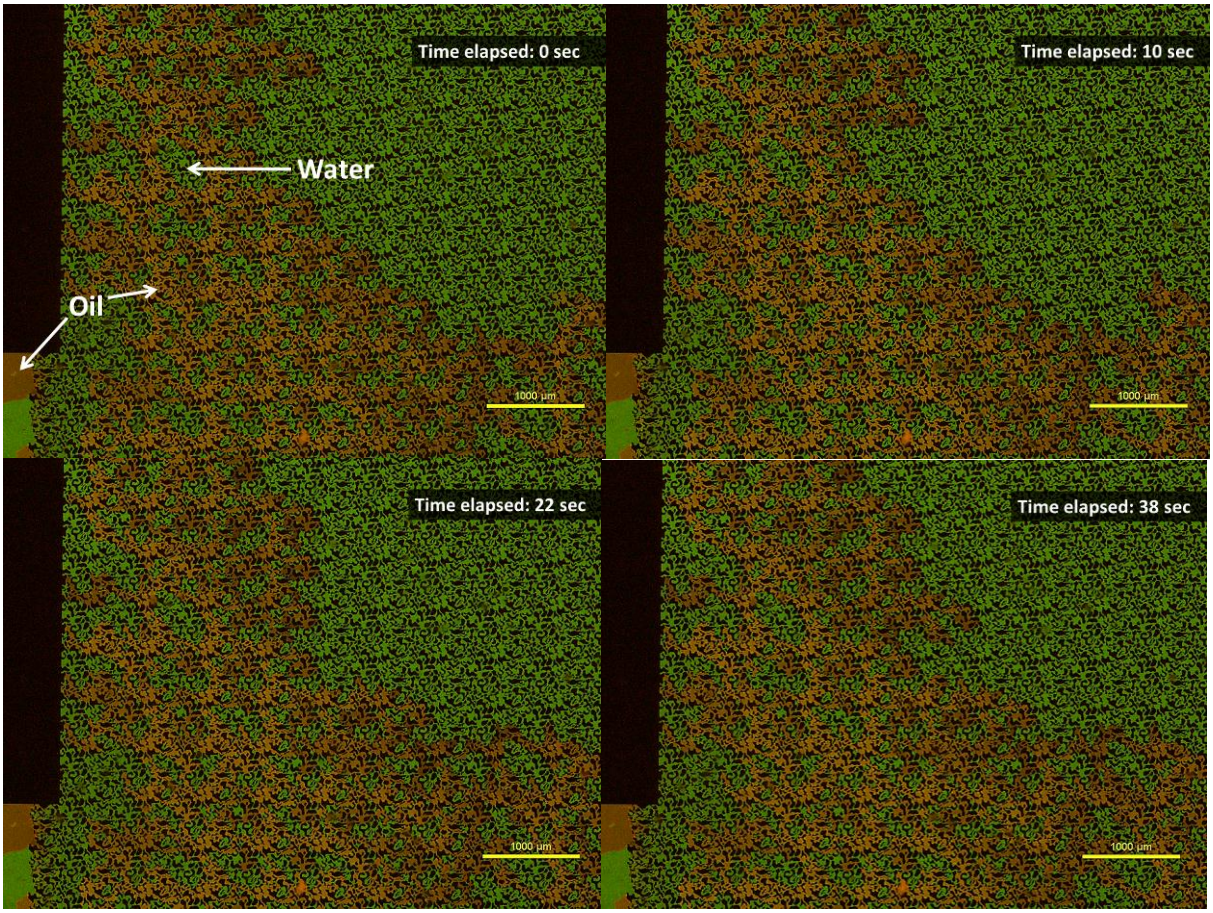

Figure 36abcd: Radial displacement pattern in the matrix with a good sweep.

A repeated drainage pattern was observed, and capillary forces causing oil to preferably flow through the largest available throats was assumed to control the flow. The filling order of pores and throats for this pore pattern was equal in almost every cluster filling event, which meant that the same pores were unswept and remained occupied by water. The oil advanced by cluster filling processes both from the upper and the lower part of the front, which eventually joined together in the middle. On occasions, cluster filling events were not distributed evenly along the front, and oil was allowed to advance further in the upper and lower parts of the front. What appeared as small oil fingers were created, and these oil fingers advanced towards each other and merged together in a short time. When they did, a larger area of water was trapped, which remained immobile as oil injection continued at a constant rate. Two small oil fingers that have merged and trapped water are shown in Figure 37.

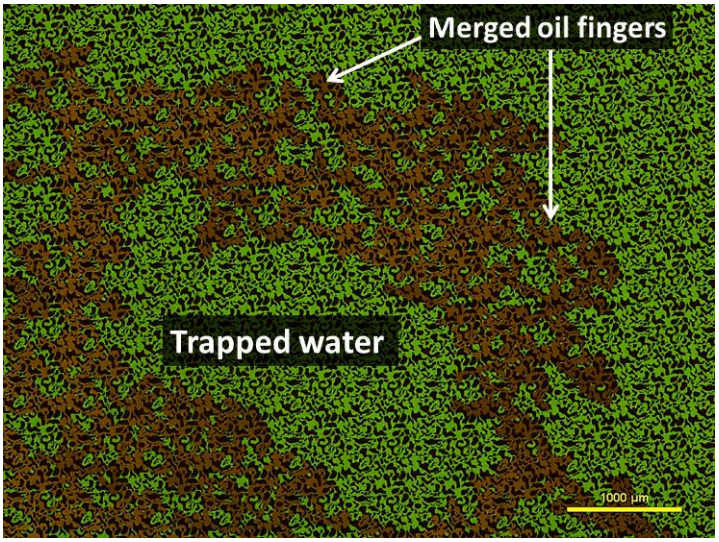

Figure 37: Small oil fingers have merged and trapped a large area occupied by water.

The radial pattern was reestablished after the trapping event in Figure 37, but it was not kept throughout the experiment as the front advanced through the matrix. Several large fingers developed that originated from both the upper and lower part of the radial front, and other parts along the injection channel where oil in the matrix had connected to oil in the channel earlier. Pulse-like filling of clusters of pores were the filling mechanism also as these fingers advanced. The preferred filling direction was towards the closed production channel, but individual cluster filling events occurred in all directions. Figure 38 show a large finger that developed from the upper part of the radial front, created from three images taken at 2x magnification. It can be seen that smaller fingers also existed as parts of the larger finger, and that they had advanced in other directions than the general flow direction.

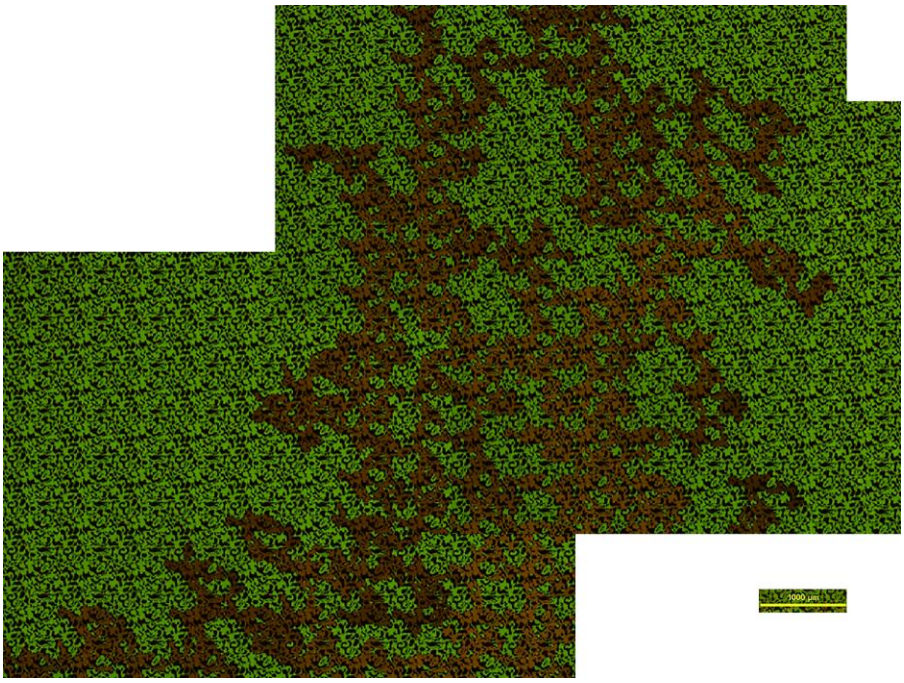

Figure 38: Large capillary finger advancing from the upper part of the front towards the production channel. Three images taken at 2x magnification have been merged together in this figure.

Water was displaced to the injection channel counter-currently as the opposite ports were closed. Initially, water flowed through continuous paths to the injection channel along most of its length, but

as injection continued and oil was forced into the matrix, most of these flow paths were blocked. Eventually, a continuous water path only existed to the rightmost edge of the injection channel, which is shown in Figure 39. This flow path was expected to last as long as the displacement rate of water was greater than what could be displaced through sheer film flow.

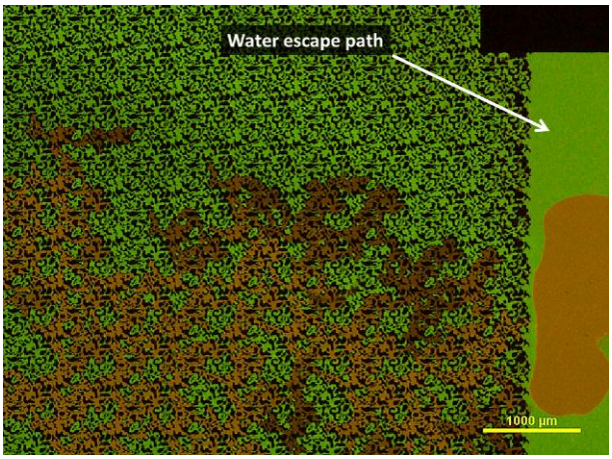

Figure 39: Continuous flow path for water to the injection channel during counter-current displacement.

Oil entered and filled the opposite water-filled channel when the oil fingers approached, and water was forced back into the matrix. From this time, oil advancement in the matrix stopped, and the injected oil flowed in the injection channel only. Large areas remained unswept by oil, both between oil fingers, and in the upper right corner of the micromodel where the fingers had yet reached. An injection rate increase to 6 mL/h with a corresponding pressure increase caused oil to start flowing in the matrix again. This time, thinner oil fingers were created than the initial ones. Pore clusters were still filled in every direction along these fingers, but to a less extent against the main flow direction than before the rate increase. The displacement rate of water after the pressure increase was low, which made it possible for oil to block the last continuous water flow path (Figure 40). The remaining water had to be displaced through film flow, or if a rapid pressure increase was performed, through double displacement events. It was also observed that initially trapped water had been displaced after the pressure increase.

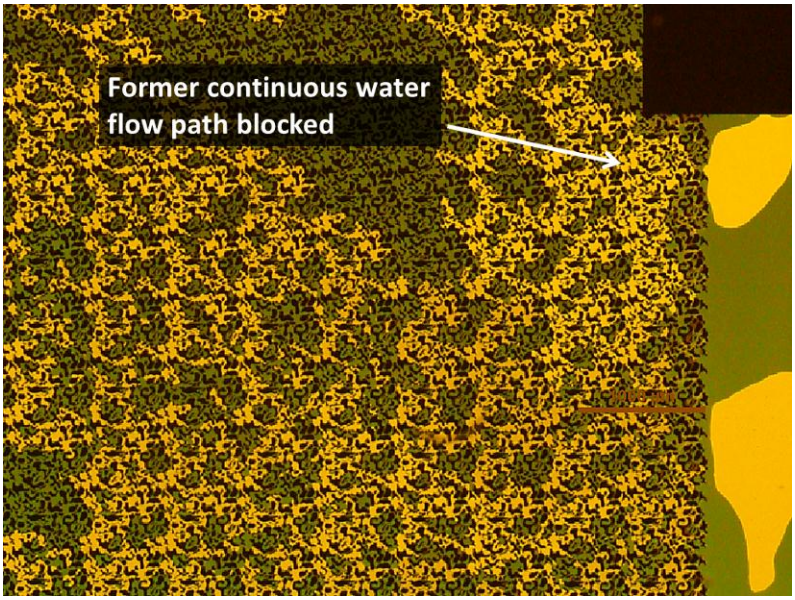

Figure 40: Oil has advanced to block the continuous water flow path observed in Figure 39 as a result of an increased injection rate. Previously trapped water has also been mobilized and displaced.

6.2.4 Stable Displacement

Primary drainage was performed in water saturated micromodel Berea D with all ports open where oil was injected at a constant rate of 0.8ml/h.

Table 11: Experimental specifics for primary drainage with oil

Micromodel	Fluid in model	Injected fluid	Fluorescence	Injection rate	Boundary conditions
Berea D	Water	Oil	FT175 1:400 Nile Red 1:500 000	0.8 mL/h	OPEN

Oil entered the matrix when the threshold pressure was exceeded and filled the matrix by a cluster filling mechanism in a radial displacement pattern, as was seen with a closed production channel. The filling process was captured at 2x magnification, and is shown in Figure 41a-c. This image sequence was taken at a distance that was further from the point of injection than the image sequence in Figure 36, in where fingering was dominating the flow pattern. Clusters of pores were filled by the pulse-like mechanism, but they were only allowed to advance a short distance from the front position, which meant that few of the large areas of trapped water were created. The macroscopic sweep was therefore almost optimal over a great distance in the matrix. Water was still left due to bypassing on the pore level, and similar pores were unswept and a repeated drainage pattern created. Also, drainage of water by film flow was observed in numerous trapped water-filled clusters, making the irreducible water saturation fairly low.

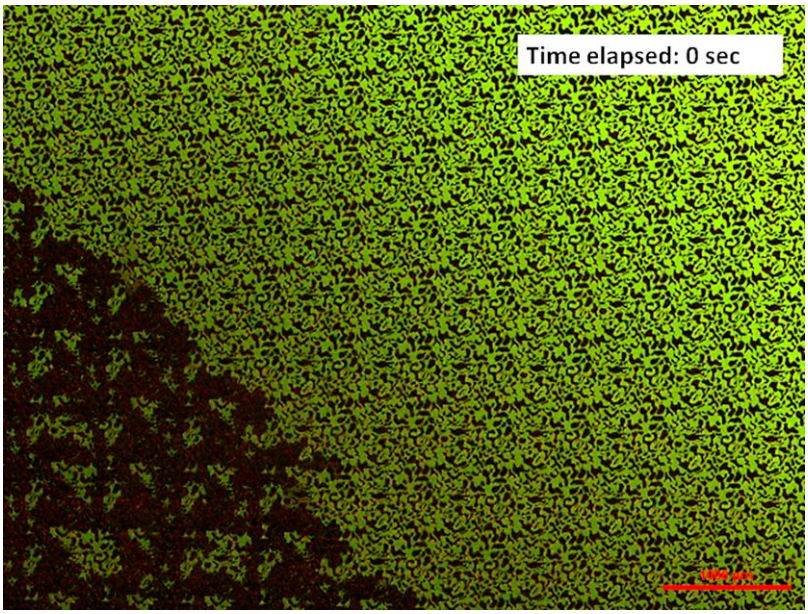

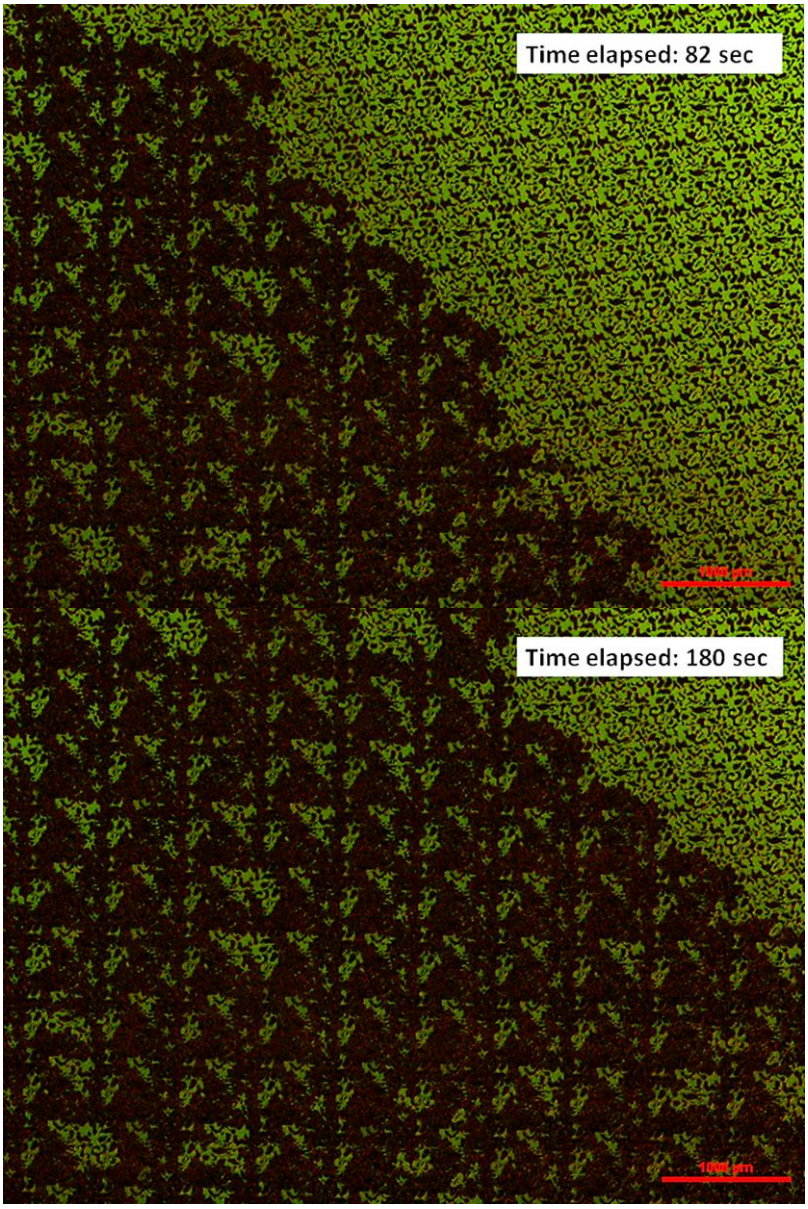

Figure 41abc: Radial displacement pattern during primary drainage with all ports open.

Counter-current displacement of water was observed early in the experiment as water entered the oil-filled injection channel (Figure 42ab). At this time, only a small part of the pore space was invaded by oil, and most water existed in continuous paths to the production and injection channels. However, some of the bypassed water was drained by film flow, and preferentially displaced to the oil-filled injection channel. Figure 42ab also show how the initial displacement pattern created an oil finger along the injection channel that later connected with oil in the channel. It was not the opposite process of oil entering the matrix from the channel that had occurred.

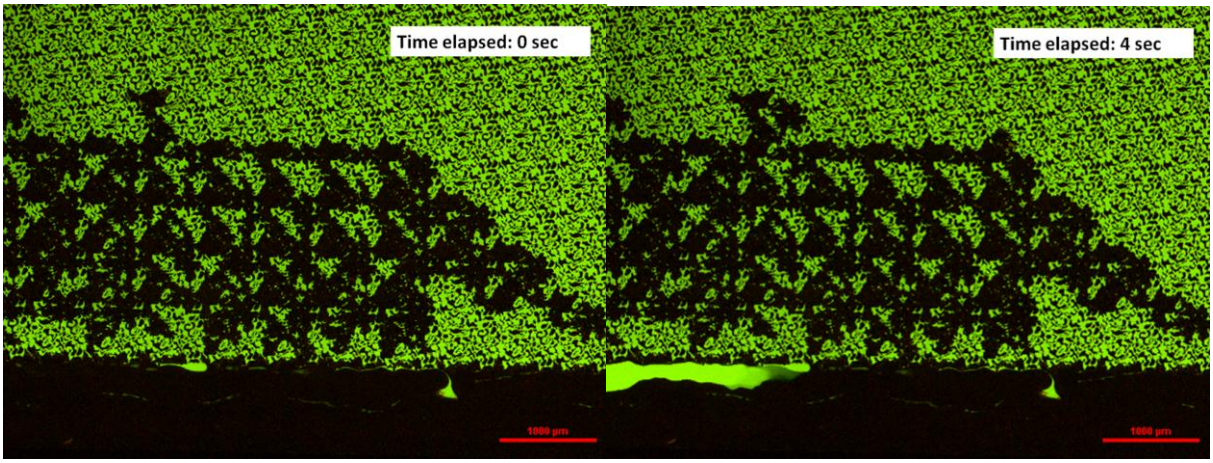

Figure 42ab: Counter-current displacement of trapped water through film flow.

As oil advanced in the matrix the radial pattern developed into a single large oil finger advancing towards the production channel. This was not a finger that appeared to develop from an unstable displacement as it was large enough to fill almost 1/4th of the pore network, and the displacement efficiency of this finger was the same as during radial displacement. At the edges of this broad oil finger, however, merging of small oil fingers leaving behind larger areas of trapped water was observed on occasions, which is shown in Figure 45. As the large finger approached the production channel, it was observed that smaller fingers were advancing from other parts along the injection channel where the oil had connected earlier (Figure 44). These oil fingers did not reach far into the matrix from the injection channel, however, and at oil breakthrough in the water-filled production channel water existed in most of the upper right part of the matrix as the broad finger did not extend into this region. Oil fingers still advanced after breakthrough, and trapped water was still being displaced by film flow.

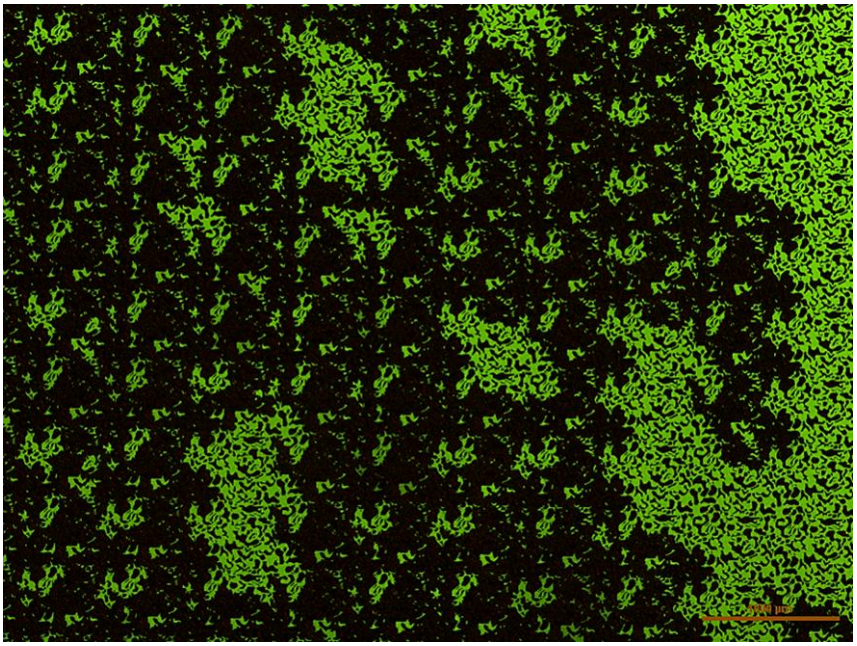

Figure 43: Larger areas of trapped water at the edge of a broad oil finger. The main flow direction of the oil finger was from bottom to top, and it swept 1/4th of the pore network.

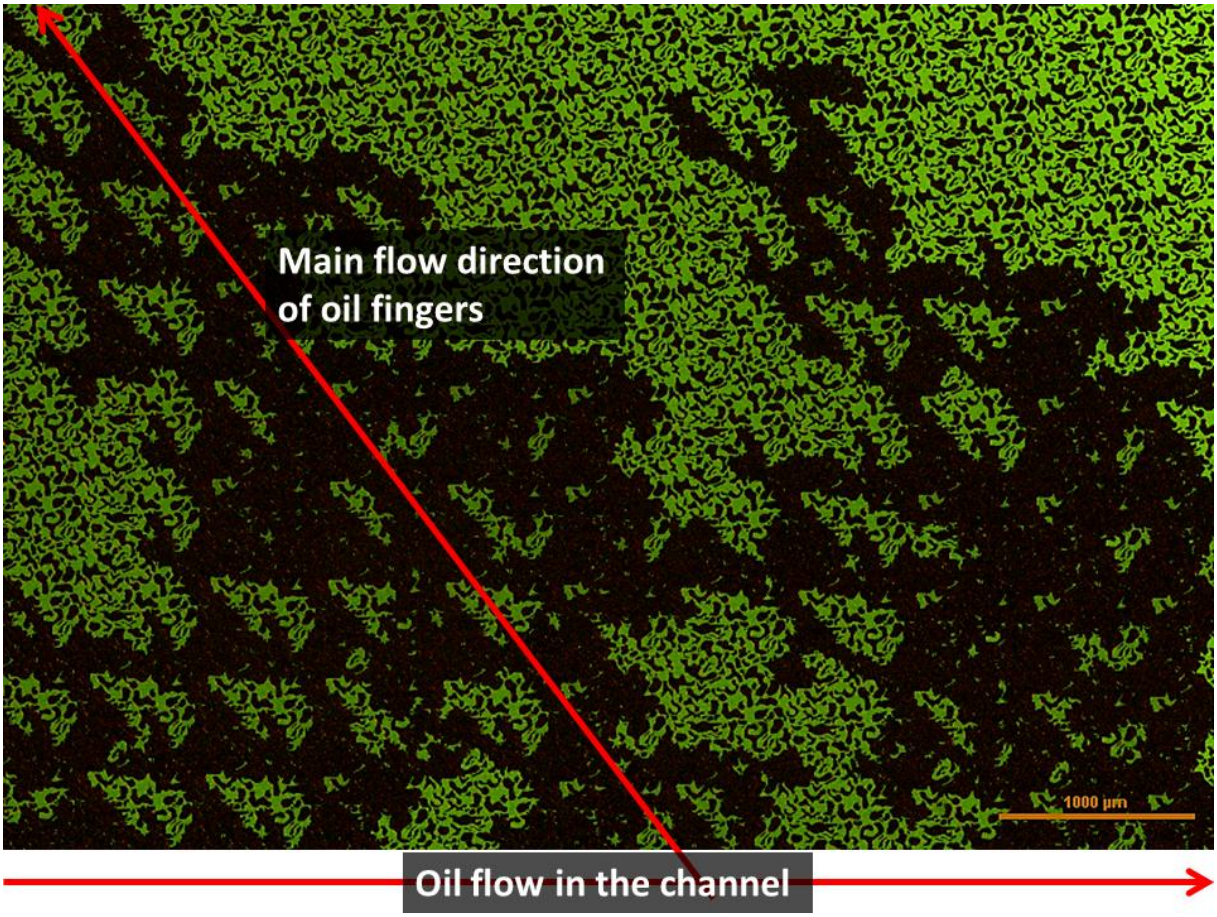

Figure 44: Smaller oil fingers advancing from the injection channel as a result of oil being continuous from the channel to the matrix.

6.2.5 Pore Level Displacement Mechanisms

Primary drainage in water-filled micromodel Berea G with all ports open was performed by injecting oil at a constant rate of 1 ml/h.

Table 12: Experimental specifics for primary drainage with oil

Micromodel	Fluid in model	Injected fluid	Fluorescence	Injection rate	Boundary conditions
Berea G	Water	Oil	Fluorescein 1:800 000 Nile Red 1:500 000	1.0 mL/h	OPEN

Observing pore level displacement mechanisms in the matrix was the focus in this experiment, and oil was observed to displace water by two main pore level mechanisms:

1. Piston displacement
    - Stable moving fluid interface
    - Haines' jump
2. Film flow

Piston Displacement

When water could exit a pore freely through a continuous water flow path, and a sharp fluid interface existed as oil displaced water, the process was defined as a piston displacement process.

Piston displacement could be subdivided into two events, depending on the stability of the fluid interface as it was advancing. When the fluid interface maintained a stable configuration throughout the entire movement, the displacement was defined as a regular piston displacement event. When the geometry of the pore network made it impossible for the fluid interface to maintain its stability, a rapid jump to the next stable position was performed by a Haines' jump. The ratio of the size of the pore to the size of the throat, the aspect ratio, determined to a large degree whether the interface remained stable when it entered a pore. Normally, an instant Haines' jump occurred at high aspect ratios, while the slower piston displacement was favored at low aspect ratios.

Figure 41a-d show a sequence of images taken at a selected location in the matrix at 5x magnification. The images were captured halfway in the matrix filling process, before oil breakthrough to the water-filled production channel and after the initial radial displacement, when capillary fingering was more dominant. In the image sequence, a pore has been highlighted that was drained by a piston displacement mechanism. From the first to the second image (Figure 45a-b), most of the highlighted pore was filled with oil instantly by a Haines' jump when the fluid interface became unstable as it entered the large pore. The water had the possibility to be drained from this pore through a continuous water flow path through three pore throats. The oil was then seen to trap some of the water in this pore by blocking the exit throats, inhibiting piston displacement of the remaining water. The remaining water therefore had to be drained by film flow, which can be seen in the last images (Figure 45b-d). This film flow was slower than the bulk flow during piston displacement, and the water displaced by this method took 8 additional seconds, making the total time it took to drain the pore 10 seconds.

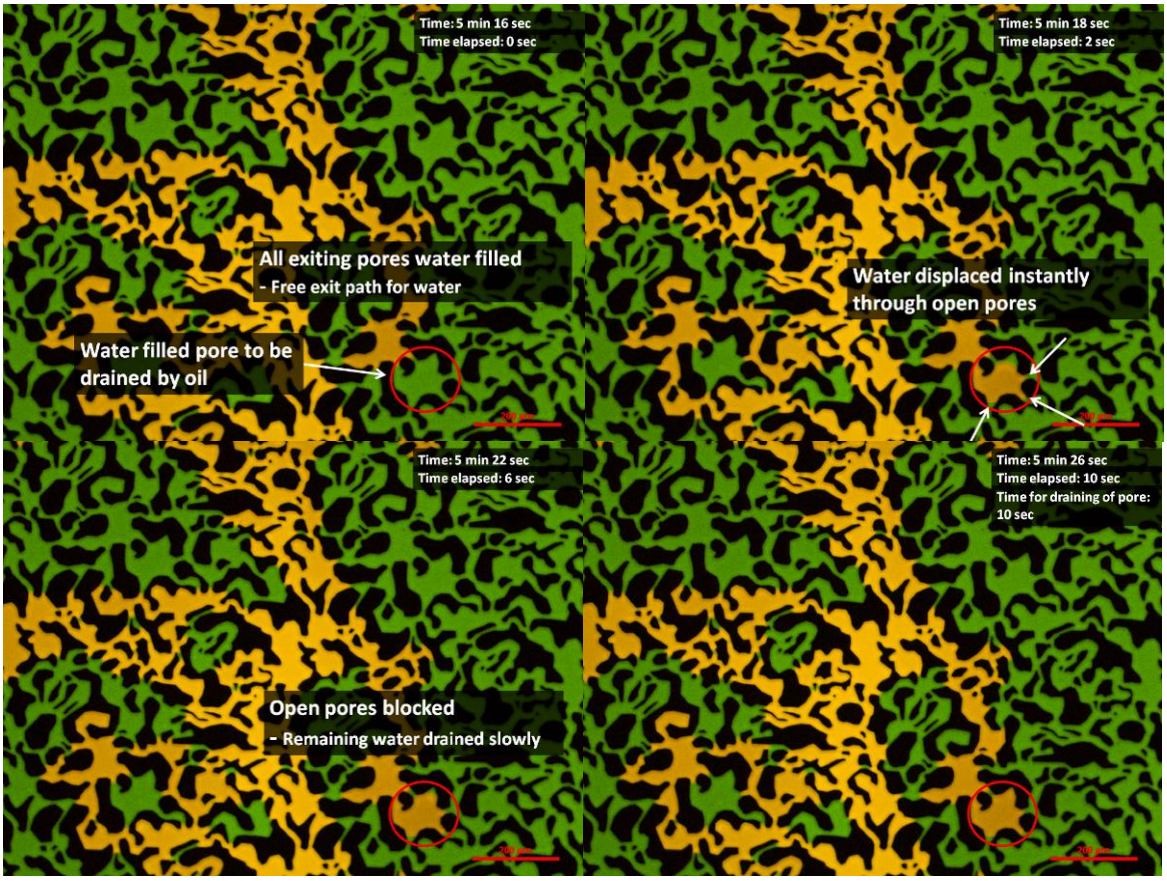

Figure 45abcd: Piston displacement event during primary drainage.

Film Displacement

As pores were invaded at different times due to different capillary entry pressures and an irregular oil finger pattern, some pores containing water were trapped by oil with no continuous flow. Once the oil phase pressure increased sufficiently to drain these pores water had to escape through film flow along the surface of the grains. This process was significantly slower than piston displacement processes as the volume of the films through which water had to flow, was magnitudes smaller than through bulk flow through throats. The films were often too small to be visualized in the microscope, and the flow direction of the displaced water could not be identified.

Figure 46a-e show a sequence of images where film displacement was observed, taken at the exact same position in the pore network as the piston displacement event described above, but occurred 1 minute later in time. A trapped water-filled pore with identical geometry to that in the piston displacement sequence is highlighted. This pore therefore contained the same volume of water, which means that the displacement speed of the two processes were directly comparable when this pore later was drained by film flow. The oil started invading the pore in the first image in the sequence (Figure 46a). The next image (Figure 46b), obtained 22 seconds later, show that the advancing fluid interface was stable during the displacement. The time from the oil entered the pore up to this point was already twice as long as it took to drain the similar pore when most of the water was displaced by Haines' jump. The stable advancing fluid interface indicated that the capillary pressure increased steadily in this process. The total capillary pressure reduction, however, may have fluctuated due to Haines' jump processes elsewhere in the pore network. It was also seen that the oil phase was flowing in the middle of the pore with water situated along the surface of the grains. This confirmed that the micromodels were more wetting towards water. While the highlighted pore was being invaded by oil, other pores in near vicinity, where free exit paths for the water existed, were fully drained of water (Figure 46c). This observation indicated that it was not a reduced total drainage rate that slowed the process, but the slow film flow mechanism. The last image shows that the pore was drained in almost 2 minutes, which made the process approximately 12 times slower than the piston displacement process.

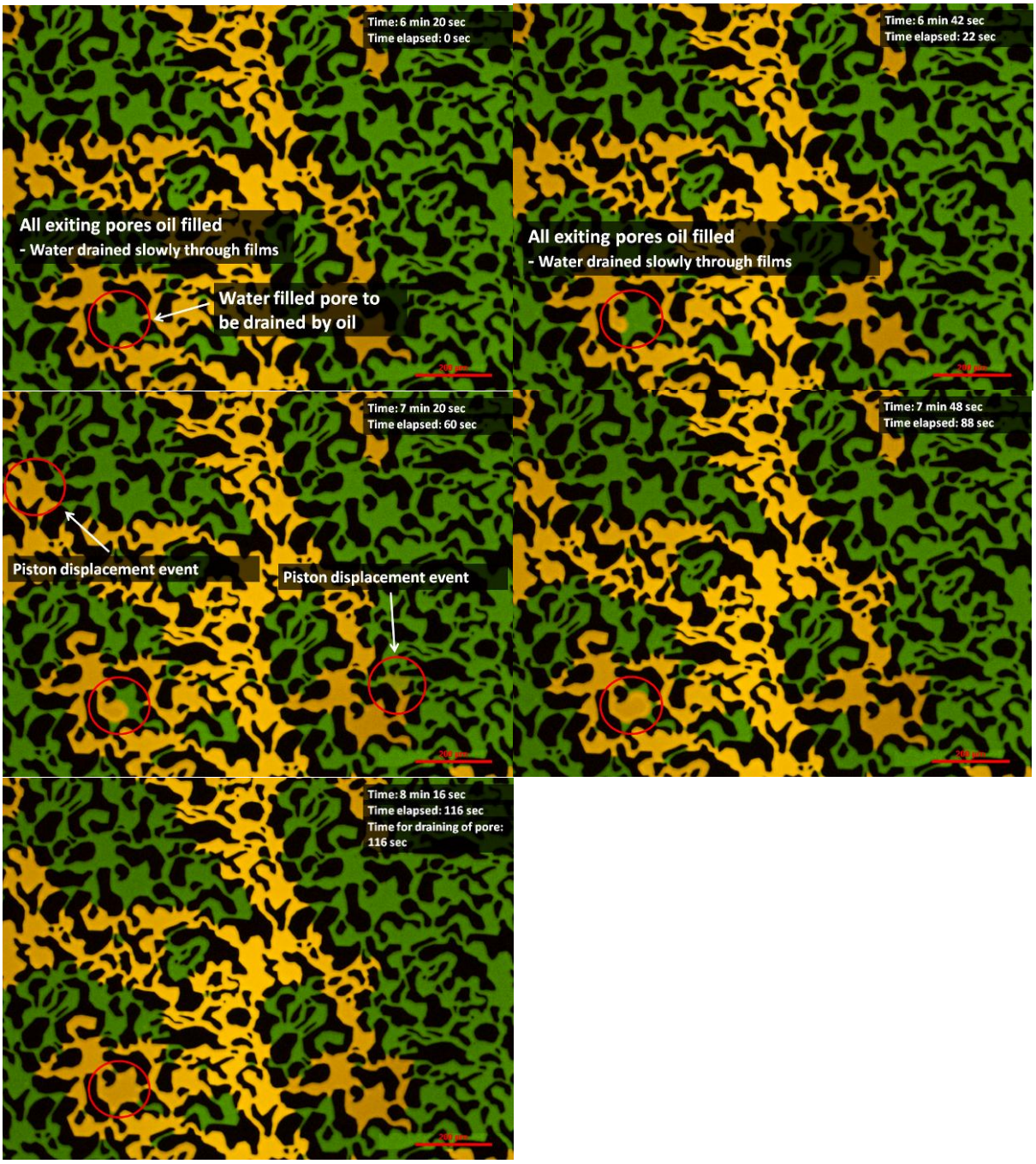

Figure 46abcde: Film displacement event during primary drainage.

Two-phase Double Displacement

In addition to piston displacement and film flow during oil-water displacement, another noteworthy mechanism involving both of the processes was observed. Even though oil was the only fluid that was injected, water was seen to displace oil from several pores in the matrix. This was most likely water that was displaced by oil elsewhere in the matrix with no continuous flow paths through the network that had reached a sufficiently high phase pressure to imbibe into oil-filled pores. When a pressure increase mobilized initially trapped water in volumes too large to be drained simply by film flow, water was forced to displace oil from nearby pores through bulk flow and piston displacement events. This flow mechanism was identified as a two-phase double displacement event, which is not to confuse with three-phase double displacement events where a phase displaces another that displaces a third. These events will be discussed during three-phase CO_2 experiments in section 6.4.

The photobleaching property of Fluorescein was beneficial in observing the two-phase double displacement events. When the focus of the camera was kept at the same place in the micromodel for a long time, water that came from other parts of the micromodel had a stronger fluorescent color, and was easily distinguished from the stationary water in the imaging sequences.

6.3 Primary Drainage with CO_2

Primary drainage was performed in water-filled micromodel Berea D with CO_2 as the non-wetting phase to study the two-phase CO_2 gas/water displacement processes on the pore level, and the large flow pattern. The contribution from diffusive processes on the displacement efficiency and drainage pattern was also investigated. Displacement events in this process will be similar to those during CO_2 storage in water aquifers, although the pressure and temperature regimes are different. The production port in the injection channel was closed while the opposite ports were open, and CO_2 was injected at a constant pressure of 0.25 bars.

Table 13: Experimental specifics for primary drainage with CO_2

Micromodel	Fluids in model	Injected fluid	Fluorescence	Injection pressure	Boundary conditions
Berea D	Water	CO_2 gas	Fluorescein 1:200 000	0.25 bars	CLP

CO_2 displaced water in the matrix in a radial pattern from bottom left towards top right (Figure 47a-d). It was, however, not by a pore-to-pore filling mechanism, as was observed in the opposite process when water displaced gas in a radial pattern, but rather by pulse-like cluster filling mechanisms, as observed in primary drainage experiments when oil was the non-wetting fluid. Small scale fingering and merging of CO_2 clusters was observed to trap clusters of water-filled pores. There appeared to be a "base" pattern of unswept pores that was created as the CO_2 clusters merged (Figure 47d). On occasions, some additional water-filled pores in this base pattern were invaded. The same base pattern could be identified in primary drainage experiments with oil, but invasion of additional water-filled pores was more common here (Figure 41). The size of the bypassed area that appeared after each cluster merging left large volumes of water in the matrix, even though the radial displacement pattern introduced an even front propagation and good sweep. A repeated drainage pattern was created as the same clusters of pores were filled during the front propagation through the matrix. Some film flow events were also observed, but these events were limited to draining of single water-filled pores, trapped cluster of pores were not observed to be drained by film flow prior to CO_2 breakthrough. Figure 47b-c show two CO_2 fingers merging and trapping water, while two small pores were drained by film flow simultaneously.

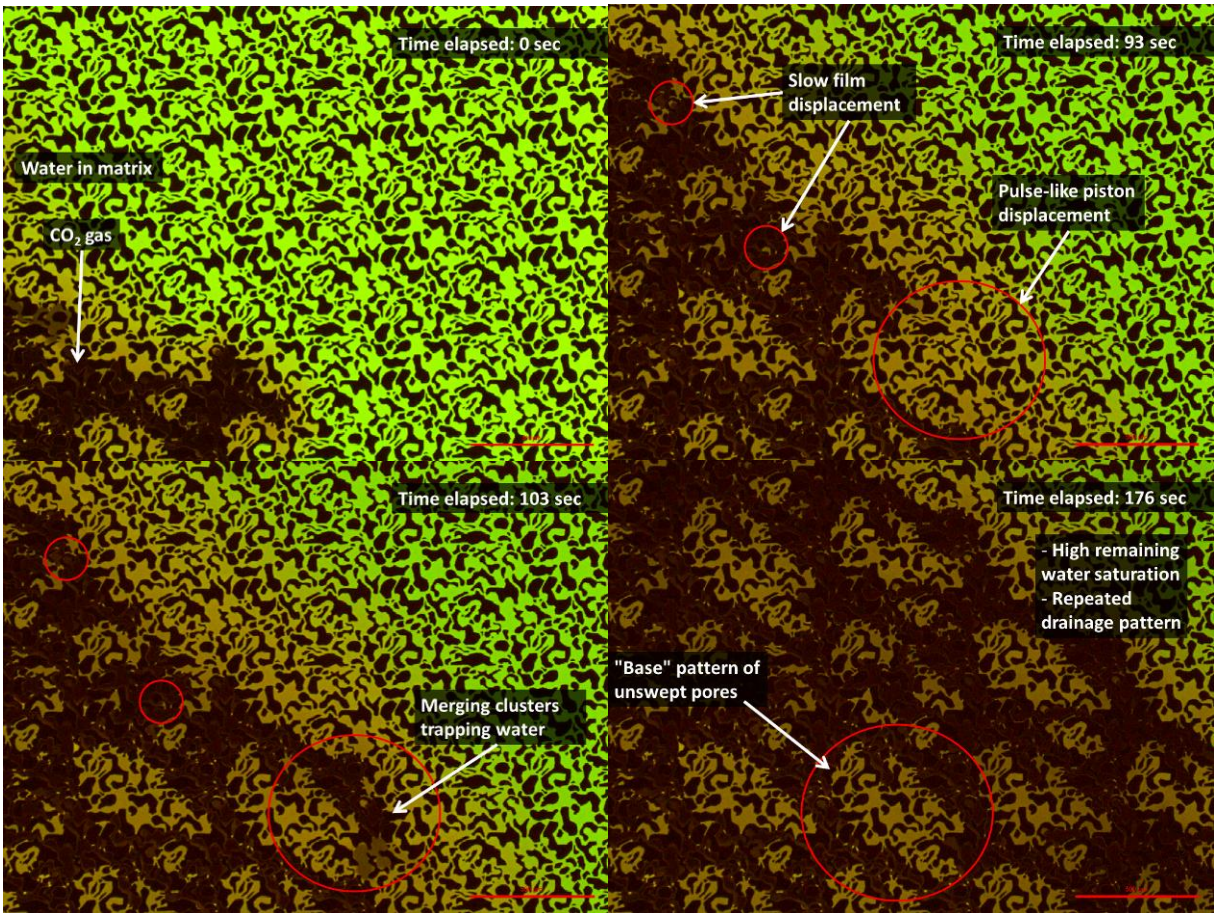

Figure 47abcd: Radial displacement of water during primary drainage with CO_2 by pulse-like filling mechanisms.

As injection continued, the CO_2 front eventually spread out and large fingers developed. Some of these reached the production channel while other parts of the pore space were unswept. The displacement rate of water was significantly reduced as most of the injected CO_2 flowed to the production channel through continuous CO_2 flow paths. The macroscopic fingering and the pore level bypass of water left the water saturation high at breakthrough (> 50%). All water was removed from the matrix eventually, even the initially trapped water, by both bulk displacement and diffusive processes. These processes were slow, however, as it took several days to remove all the water from the micromodel.

6.3.1 Pore Scale Displacement Mechanisms

The pore level displacement mechanisms during primary drainage with CO_2 were similar to those observed when oil was displacing water. Both piston and film displacement were observed, which is shown in the image sequence in Figure 48a-d. The image sequence was taken at a location in the matrix where a large CO_2 finger was advancing. The highlighted cluster of pores in Figure 48a was drained by a piston displacement event instantly by a Haines' jump displacement, and the CO_2 advancement stopped as small water-filled throats or trapped water blocked all available flow paths from this pore cluster. The CO_2 gas in this location had advanced in periodic pulses up to this point. Each time small throats stopped the advancement, the pressure build up eventually initiated another piston displacement event where CO_2 moved to fill more cluster of pores. After the piston event of the highlighted cluster, this periodic advancement stopped, and only film flow was observed. This meant that the drainage rate of water was greatly reduced, which can be seen in Figure 48c-d, as in

92 seconds only minor volumes of water was displaced. This indicated that the CO_2 phase pressure did not increase sufficiently in this pore to continue advancing.

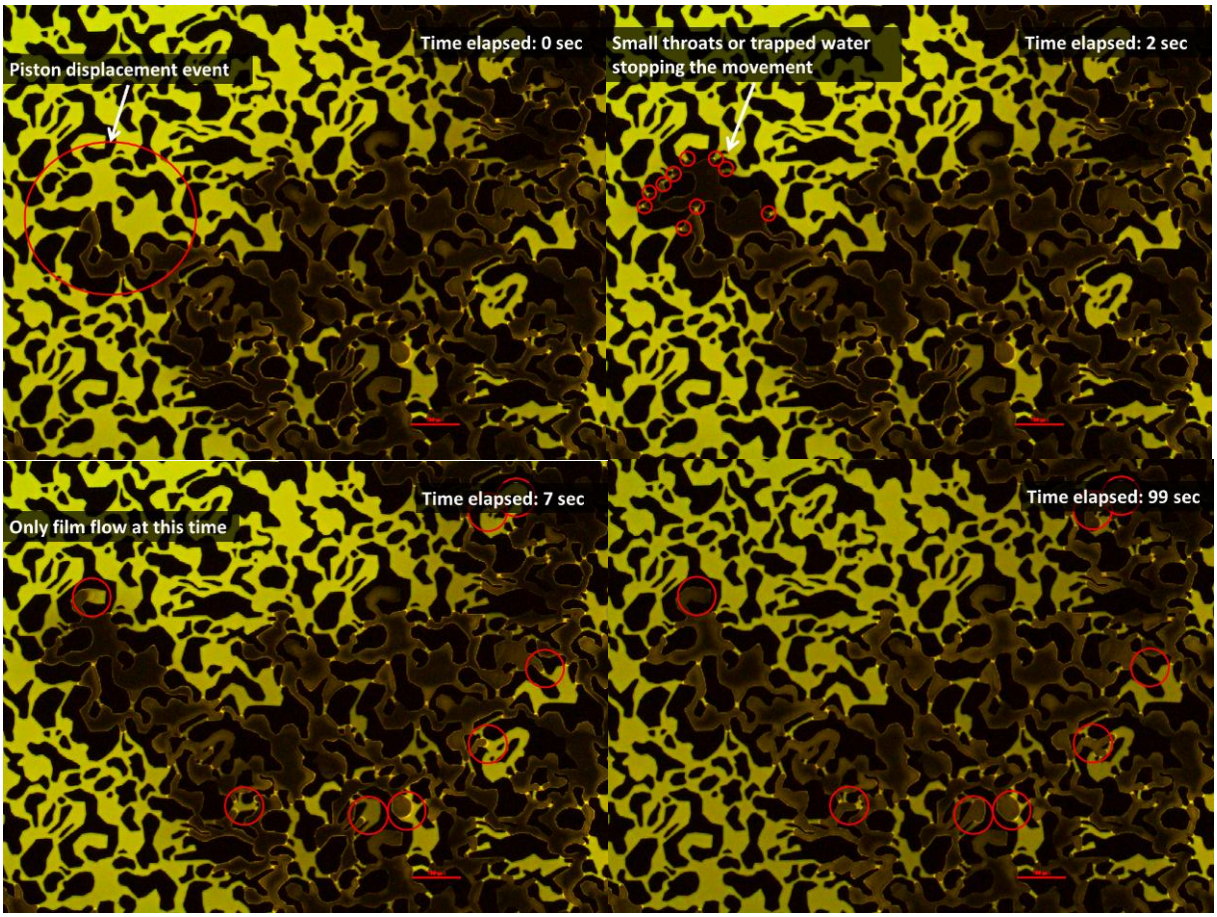

Figure 48abcd: Pore level displacement events during primary drainage with CO_2.

6.4 *Contact Angle Measurements*

The wetting preference of the silicon micromodels was easily identified visually from the fluid configurations during spontaneous imbibition and primary drainage experiments, since water preferred to flow in narrow pores and throats, and water films coated the matrix grains. Qualitative measurements of the wettability of the micromodels could be obtained by measuring the contact angle between water and the non-wetting phase. This was done in several experiments performed in the sections 6.1 and 6.2. However, the exact position of the fluid interfaces where the contact angles were measured was not clearly identified, and the shape of the fluid interfaces was influenced by uneven geometries in the pores space. Therefore, obtaining exact values representative for the system as a whole by this method would be misleading, and the values will only be used to indicate the wettability of the micromodels.

Advancing CO_2/Water Contact Angle

During a spontaneous imbibition experiment with fluorescent water and CO_2, the fluid interface was curved with water having the largest contact area with the grains. The advancing CO_2/water contact angle, ϑ_{gw}, was measured on a retreating CO_2 bubble between two grains at nearly straight surfaces ensuring that the orientation of the bubble was least affected by an uneven geometry (Figure 49). The contact angle was measured to approximately 73 and 78 degrees, indicating a slightly water wet surface.

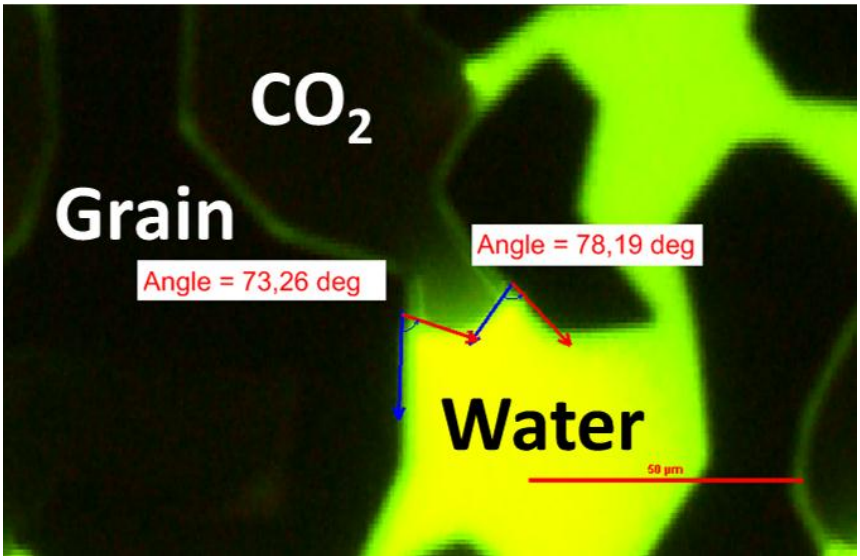

Figure 49: Measurement of the advancing contact angle between water and CO_2.

Receding Oil/Water Contact Angle

The receding oil/water contact angle was measured in primary drainage experiments at selected oil-water interfaces in locations where it was least influenced by the pore geometry. ab show the receding contact angle measured at advancing interfaces from two different experiments. The receding oil-water contact angle was found to be between 15° and 20° in this process, indicates that water is strongly wetting to oil in the silicon micromodels.

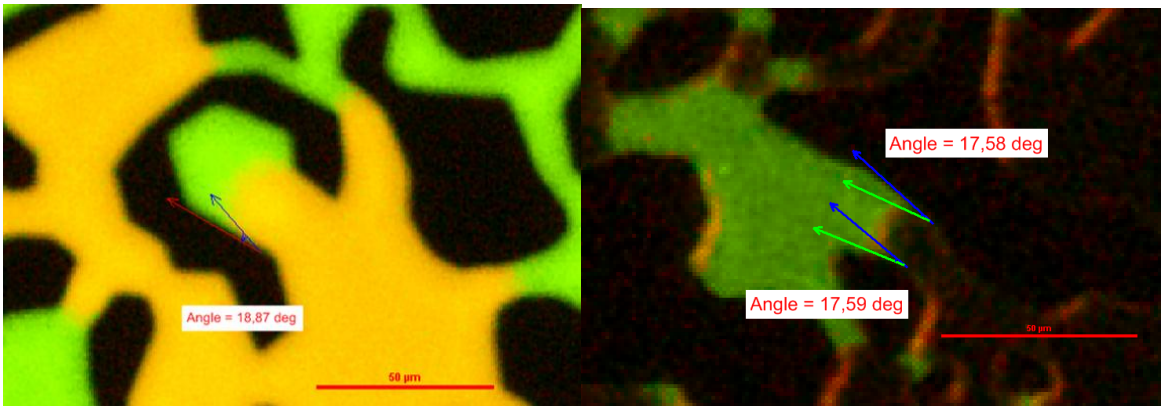

Figure 50ab: Receding oil-water contact angles measured at advancing fluid interfaces.

Receding CO_2/water Contact Angle

The receding CO_2/water contact angle was measured during primary drainage with CO_2 on a fluid interface in a narrow channel. It was found to be approximately 15^o showing that water was strongly wetting to CO_2 in this process.

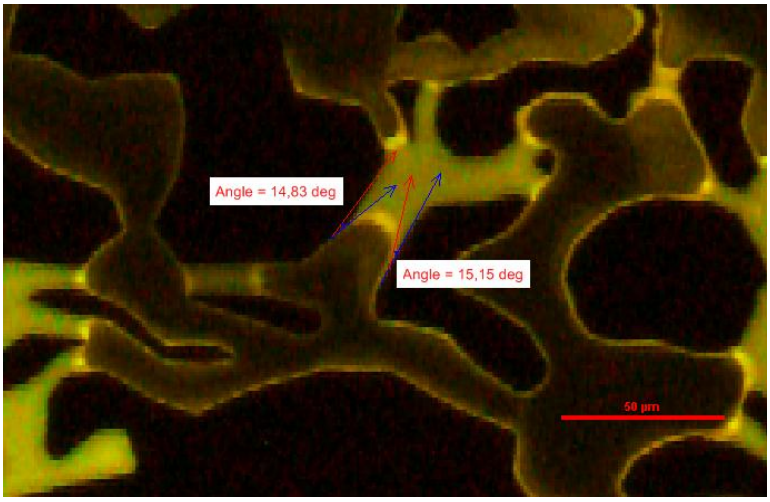

Figure 51: Measurement of the receding CO_2/water contact angle.

6.5 Three-Phase CO_2 Gas Injection

6.5.1 Pore Level Events during CO_2 Injection in Partially Waterflooded Zones

Three-phase flow during CO_2 injection in partially waterflooded zones was studied by injecting CO_2 at a constant pressure of 1.5 bars in micromodel Berea B partially filled with oil and water.

Table 14: Experimental specifics for CO_2 in partially waterflooded zones

Micromodel	Fluids in model	Injected fluid	Fluorescence	Injection pressure	Boundary conditions
Berea B	Water and oil	CO_2 gas	Fluorescein 1:800 000 Nile Red 1:500 000	1.5 bars	OPEN

Before CO_2 flooded the location where the pore level displacement events were captured, water was occupying the smallest pores and throats, while oil was in the largest pores, and most of the pore space was saturated with oil. The location in the pore network where pore events were captured was situated close to the injection channel, and as a high injection pressure was applied (1.5 bars), large parts of the pore space were filled by CO_2 in a few seconds. CO_2 was observed to enter the large oil-filled pores first, while water remained stationary, causing the oil saturation to quickly decrease. CO_2 flowed in the matrix without creating a continuous path as it bypassed parts of the pore space closer to the injection channel, and came to a rest in large oil-filled pores further in the matrix. This lead to all three phases existing in numerous discontinuous clusters after a short time, and these discontinuous phases moved back and forth in all directions in a chaotic manner. An image showing the fluid configuration early in the process, taken at 10x magnification, can be seen in Figure 52. In the image water is green, oil is yellow, CO_2 is dark brown, and grains are black.

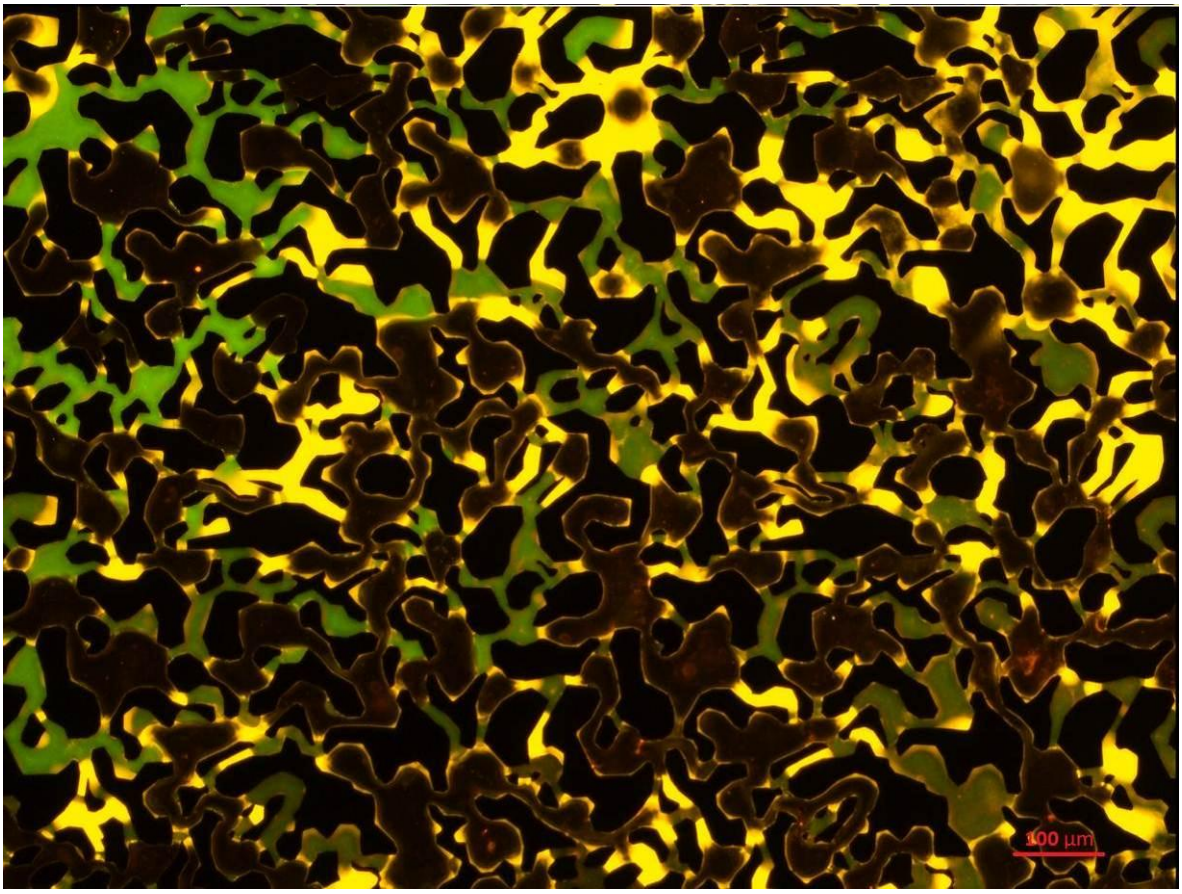

Figure 52: Fluid configuration during CO_2 flooding in a partially oil- and water-filled micromodel.

Figure 52 shows that CO_2 was occupying the largest pores, oil was in the large pores and throats that the CO_2 had not yet invaded, and water was mainly in the smallest pores and throats. It was also observed that in locations where the water phase was continuous over several pores, as for instance in the upper left corner, even larger pores were occupied by water. This was related to displacement events during the previous water imbibition cycle and will be discussed in chapter 7. Oil was displaced to narrower throats and to the outer edges of the pores during the filling process, as CO_2 flowed into the middle of the oil-filled pores and expanded outwards. The oil was never completely removed from the pores, but surrounded CO_2 as an oil film. In fact, water was never seen in direct contact with CO_2 because of this oil layer between the water and CO_2 phase, hence oil was spreading in this system. This layer was capable of conducting oil by the same means as the water films that coated the grains. This meant, however, that even when water and oil were trapped and discontinuous, escaping through water films and spreading layers was possible.

The pore level displacement events that lead to the fluid configuration in Figure 52, and that was observed as CO_2 injection continued, differed slightly from those observed during spontaneous imbibition and primary drainage experiments. CO_2 advanced by these pore-level mechanisms:

- Piston displacement
- Snap-off
- Haines' jumps
- Double/Multiple displacement

Piston displacement always occurred to some extent before and after a Haines' jump or a snap-off event, but few pores were seen to be completely drained with a stable moving CO_2/oil interface. When CO_2 faced water-filled or oil-filled throats, the flow stopped while the CO_2 phase pressure

increased, until the capillary pressure was overcome and the throat was invaded. When it reached the pore on the opposite side of the throat, the larger geometry caused the fluid interface to become unstable, and CO_2 spontaneously filled the available space to reach a stable position. The way the pore was filled in this process separated Haines' jumps from snap-off events.

In a Haines' jump event, the spontaneous movement of CO_2 displaced all of the oil except for the spreading layer from the pore, and the CO_2 was continuous to the pore from which it had entered during the whole process (can be seen in Figure 54f). The oil was drained from the pore almost instantly as a sharp fluid interface existed throughout the movement. Snap-off occurred when CO_2 could not remain continuous during this spontaneous movement. As CO_2 entered the large pore, a bubble snapped-off from the exit of the throat that advanced instantly into the middle of the oil-filled pore (can be seen in Figure 54d-e). From here it expanded outwards and displaced the oil through the continuous spreading layer, or by piston displacement through adjacent throats. This expansion continued until only the spreading layer remained, which typically took a few to tens of seconds. Neither the spreading oil layer of oil, nor water films could be seen in completely CO_2 saturated regions. Whether these films had been removed through diffusive processes, or were present and able to conduct fluids, was not observed.

Whether a Haines' jump or a snap-off event occurred in the displacement process of oil by CO_2 depended mainly on the aspect ratio, which is the relative size of the pore and throat involved in the displacement. However, fluid configurations in the pore space were also observed to affect the process. Especially important was whether the displaced oil was trapped, or if it had a continuous flow path through nearby pores and throats. It was observed that when oil was trapped, a sharp CO_2/oil interface was preferably kept throughout the movement, and the pore was drained by Haines' jump or piston displacement depending on the stability of the fluid interface. Haines' jump occurred most commonly, and stable piston displacement was only observed when single trapped oil-filled pores were drained, and oil was displaced through spreading layers. During a Haines' jump, the displaced oil could move on to displace both water and CO_2 from nearby pores if the amount oil that were moved in a short time was too large to be drained through spreading layers (seen in Figure 54f). Snap-off events occurred most commonly if CO_2 displaced oil that could be removed by bulk flow through a continuous oil path (seen in Figure 54c and Figure 54d-e), but it was also the most common mechanism when the trapped oil clusters were large.

Water was also mobilized in the CO_2 injection process even though it was never directly displaced by CO_2. Instead, it was displaced through double or multiple displacement events where CO_2 displaced oil that displaced water, which again moved on to displace oil, or was removed by flow through water films. This meant that in every water displacement event, oil was also transported. Multiple displacement events where water displaced oil rather than escaping through film flow were observed frequently, and these displacement events also occurred with stable advancing fluid interfaces or by rapid jumps. This is illustrated in Figure 53a-f where water advanced in the pore network and displaced CO_2 surrounded by a spreading layer of oil. Initially, the fluid interfaces moved stably with no observed fluid movement in nearby pores (Figure 53a-b). When it reached an unstable position, it performed a Haines' jump to the next stable position, and in this movement, fluid redistribution in nearby pores was observed (Figure 53c-d). This occurred as the sudden change in fluid configuration affected the local pressure distribution. The equilibrium position was only temporary until the fluid interface reached a new unstable position and performed a larger jump (Figure 53e-f). A significant volume of CO_2 was displaced in this jump, and a greater fluid redistribution followed.

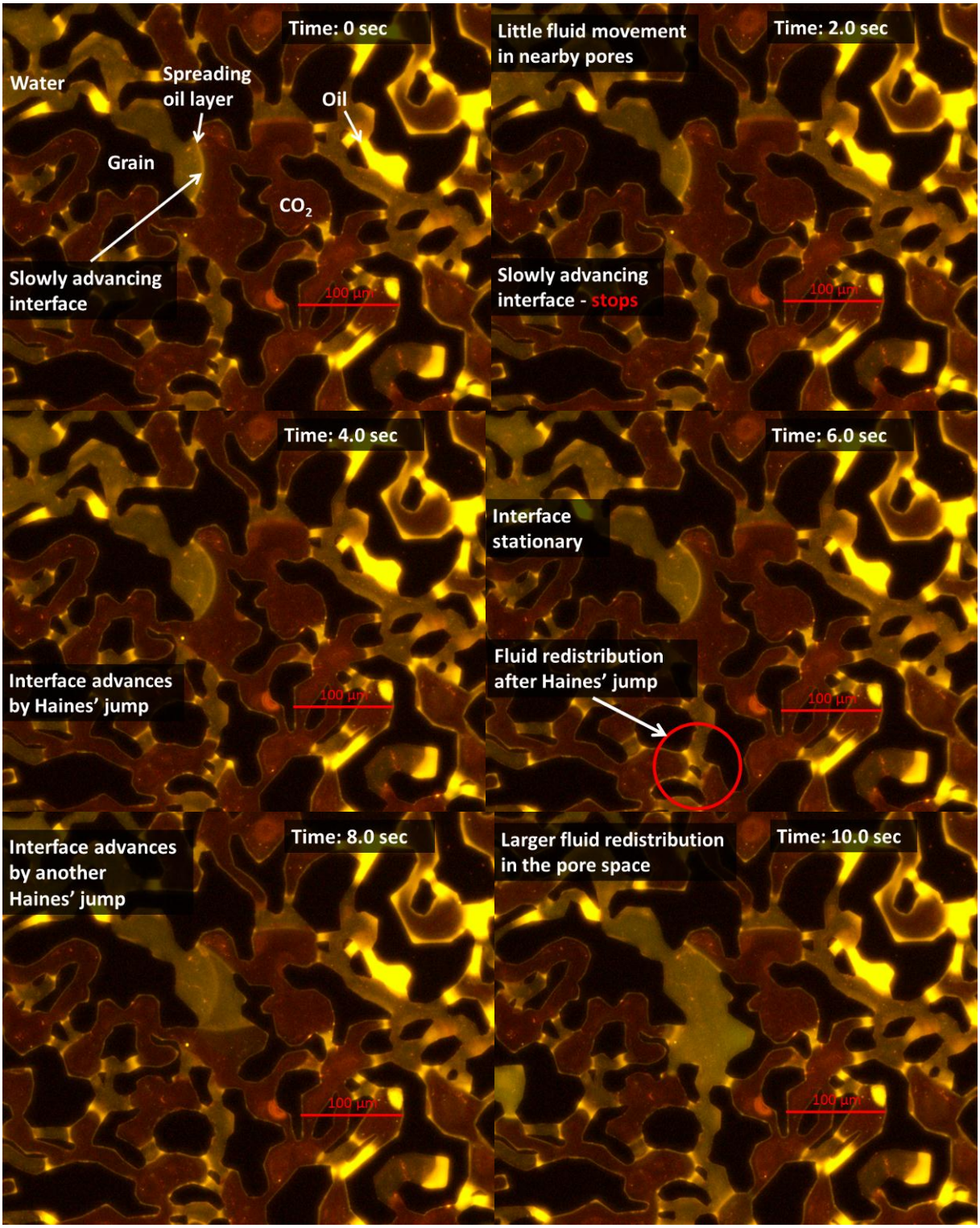

Figure 53abcdef: Water displacing CO_2 surrounded by a spreading layer of oil, both by stable piston displacement and Haines' jump, during CO_2 injection.

6.5.2 Pore Level Displacements during CO_2 Injection at Irreducible Water Saturation

The multiple displacement events with the advancing water interface in Figure 53 were captured at high CO_2 saturation and fluid movement was generally slow. Due to the high injection pressure and the proximity to the injection channel of the studied area, the pore level processes were fast and chaotic in the initial displacements when CO_2 flooded the area. As the camera only could capture images every 2 seconds, the displacement events where CO_2 displaced oil by Haines' jump or snap-off were not fully visualized in the time-lapse images. CO_2 injection into oil-filled micromodel Berea D at irreducible water saturation was performed to study displacement of water and oil by CO_2 injection at a lower displacement rate. A lower injection pressure was applied, and a location situated further away from the injection channel was selected in order to achieve this. The lower water saturation in this experiment compared to that described in section 6.5.1 meant that the oil phase initially existed in more continuous cluster of pores in this experiment. The experimental specifics are given in Table 15.

The initial fluid saturations prior to CO_2 injection were 75.5 % oil and 24.5 % water in the area fully swept by oil. Some small bypassed and unswept areas of water also existed so that the average water saturation was somewhat higher for the entire micromodel. CO_2 was injected at a constant injection pressure of 1 bar, and pore level displacement processes were captured at an advancing CO_2 front in the matrix.

Table 15: Experimental specifics for CO_2 in an oil-filled micromodel at irreducible water saturation

Micromodel	Fluids in model	Injected fluid	Fluorescence	Injection pressure	Boundary conditions
Berea D	Water and oil	CO_2 gas	FT175 1:400 Nile Red 1:100 000	1.0 bars	OPEN

The time-lapse sequence in Figure 54a-h show many of the pore scale fluid displacement events that was observed in three-phase flow during CO_2 injection, some of which has already been described in section 6.5.1. A selected area close to the CO_2 front has been highlighted in Figure 54a-h where both water and oil existed as discontinuous phases. CO_2 was injected from bottom left and displaced water and oil towards top right in a radial pattern where observations were made. The discontinuous oil closest to the CO_2 front was displaced first through spreading layers, both by a stable piston interface and by Haines' jumps (Figure 54a-b). The discontinuous water in the adjacent pores was stationary at this time. If the direction of the advancing front was to be kept, this water should be displaced next, but instead oil at the opposite side of the water-filled pores was drained. The oil-filled pores that were invaded could be displaced through continuous oil paths, and the displacement was by CO_2 bubbles that snapped off into the middle of the pores and expanded outwards. Oil was displaced towards the trapped water, which was drained from the pores through film flow (Figure 54c-d). More oil-filled pores were drained by snap off mechanisms as the CO_2 front advanced, and eventually, oil in the vicinity of the CO_2 front became trapped, and had to be drained by spreading layers. Haines' jump therefore replaced snap-off as main displacement mechanism for the remaining layers (Figure 54e-g). After the CO_2 front had passed the highlighted area, all the water had been removed by film flow, but some oil was still left. The remaining oil was later removed by diffusion, or through spreading layers, if these were still present (Figure 54h).

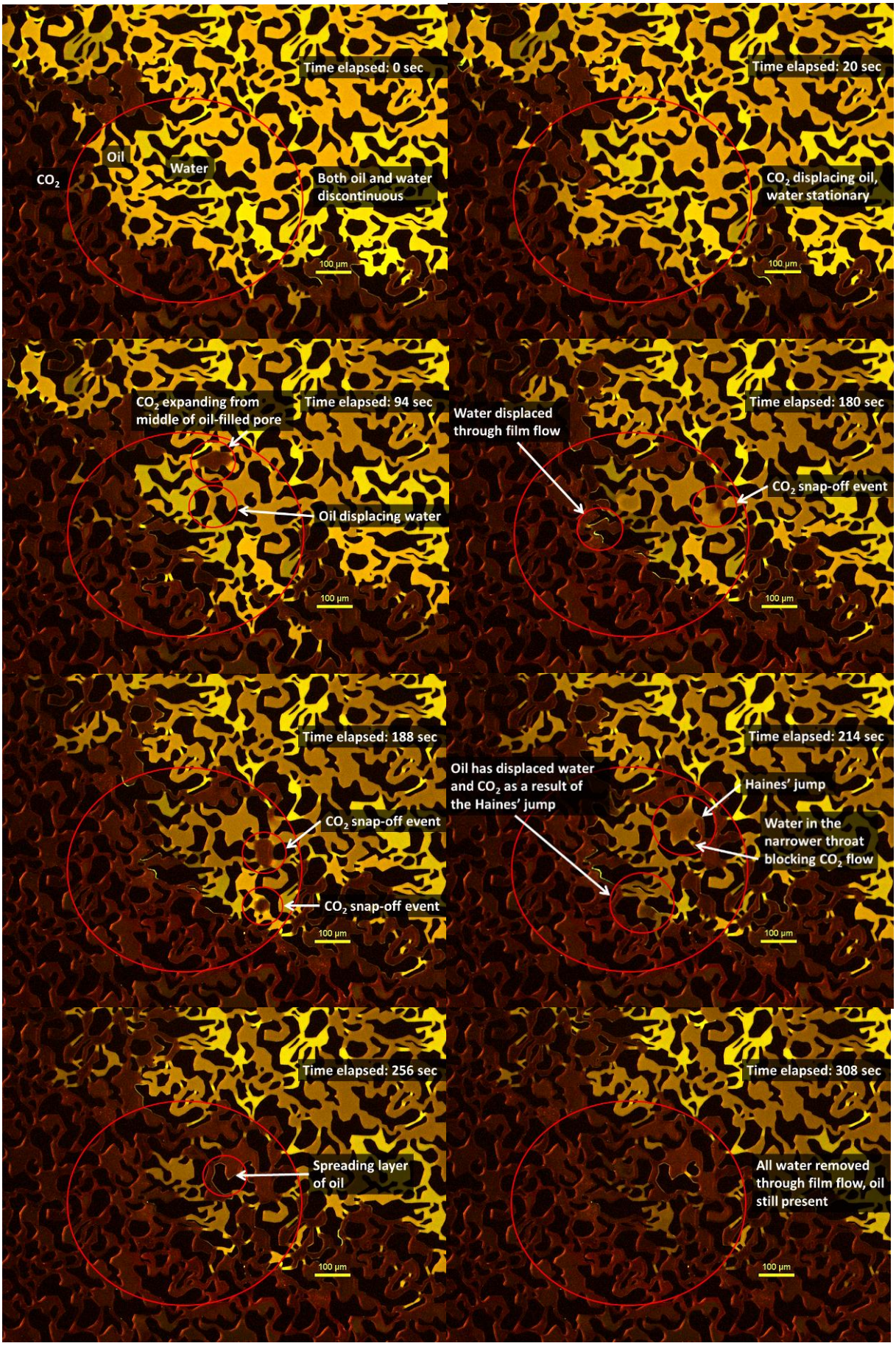

Figure 54abcdefgh: CO_2 displacing oil and water at the advancing front in the matrix.

CO_2 injection was allowed to continue for a day at a constant injection pressure of 1 bar. At this time, CO_2 had displaced all of the oil and water in most parts of the matrix, and a clear CO_2 front existed close to the opposite channel diagonally away from the point of injection, which is shown in Figure 55. Very slow bulk displacement processes was observed at this time, and diffusive processes may have been increasingly important at low displacement rates. The front was not entirely sharp, as some pores were still occupied by oil in the region swept by CO_2. As water was not observed in this region, flow through fluid films may have been an important displacement mechanism in the CO_2 swept area. If water films and spreading layers existed, both water and oil could have been drained through film flow. However, the spreading oil layer was most likely easier removed through diffusive processes with CO_2, and the oil may have become hydraulically disconnected before all was removed. It was also seen that CO_2 fingers had advanced through the region still occupied by oil and water to the opposite channel through bulk displacement processes, and that some fluids were still flowing through these fingers.

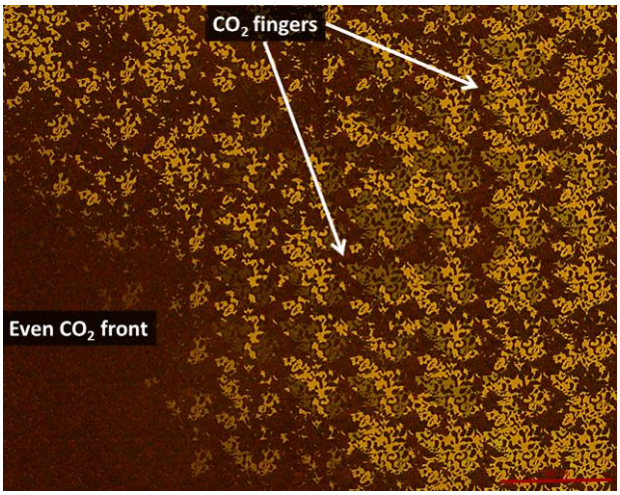

Figure 55: A slow advancing CO_2 front close to the production channel, located diagonally away from the point of injection.

6.5.3 Fracture/Matrix Interactions during CO_2 Injection in Partially Waterflooded Zones

Fracture/matrix interactions during CO_2 gas injection was studied in micromodel Berea G partially filled with oil and water. CO_2 injection was performed at a constant injection pressure of 0.5 bars, and the opposite ports were closed.

Table 16: Experimental specifics for CO_2 injection in partially waterflooded zones

Micromodel	Fluids in model	Injected fluid	Fluorescence	Injection pressure	Boundary conditions
Berea G	Water and oil	CO_2 gas	Fluorescein 1:800 000 Nile Red 1:500 000	0.5 bars	COP

The water saturation was slightly above the irreducible water saturation (S_w=0.45) in the matrix close to the injection channel when CO_2 entered the micromodel. CO_2 filled the injection channel before displacing fluids in the matrix. Both oil and water were present in the injection channel when CO_2 entered, and it was observed that CO_2 followed the oil phase in the channel while bypassing water. This is shown in Figure 56.

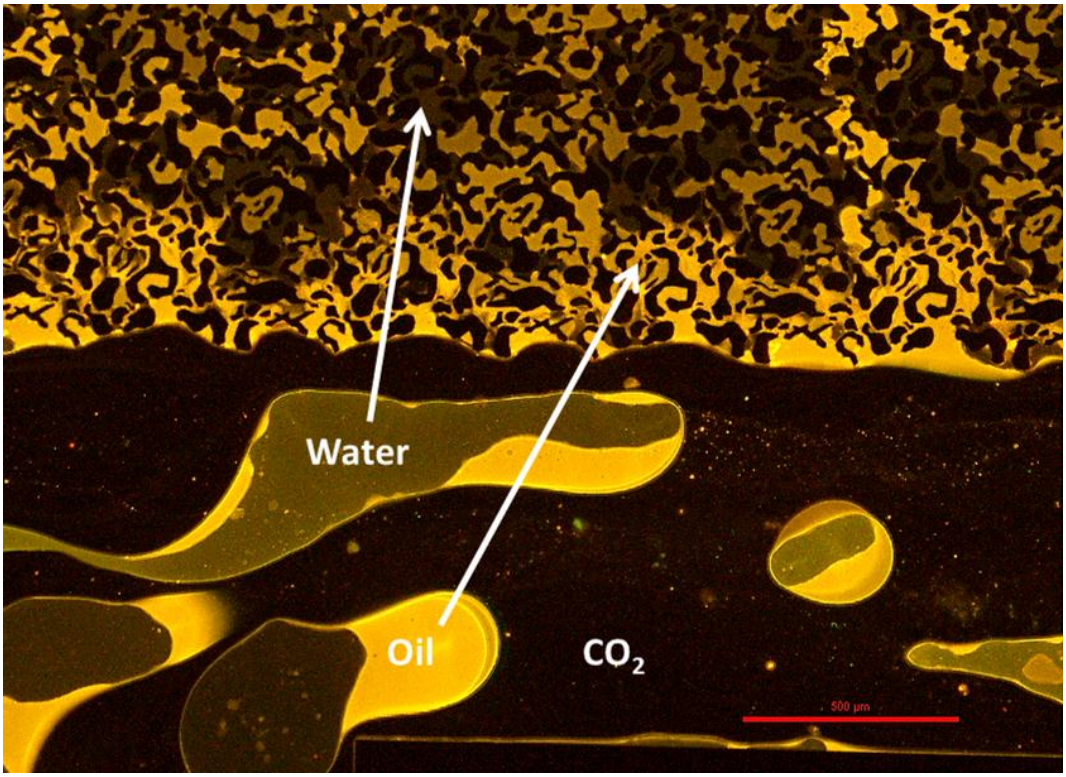

Figure 56: CO_2 gas in the channel (dark black) displacing oil with Nile Red (orange) and bypassing water with Fluorescein (initially green). CO_2 has not yet entered the matrix, and the dark fluid there is fluorescent water that has suffered from photobleaching.

A spreading oil layer was always present between CO_2 and water also in the injection channel. When CO_2 entered the matrix the oil-filled pores were preferably drained, while water remained stationary, as was observed for displacements further inside the pore network. Continuous CO_2 paths from the channel to the matrix were not created initially, as continuous oil paths present before CO_2 invasion into the matrix only existed over the range of a few pores. Instead, wherever CO_2 faced water-filled throats that disconnected oil-filled clusters of pores, it performed a rapid jump past the throats into the middle of the oil-filled pores by the snap-off mechanism. The CO_2 appeared as discontinuous bubbles in the matrix as a result of the displacement process, which can be seen in Figure 57. These bubbles were not as stationary as was seen at the slow moving CO_2 front described in section 6.5.2, but instead they continued advancing further into the matrix, and were replaced by new CO_2 bubbles. Oil reentered the pores when CO_2 exited, only to be displaced again when another CO_2 bubble appeared. The oil was therefore in many places only moved back and forth over a short distance between each arriving CO_2 bubble. It was observed that all of the bubbles that entered the matrix tended to flow in the same flow paths, even though neither CO_2 nor oil was continuous through these paths.

Continuous oil paths over several pores existed in the transition from the channel to the matrix, through which oil flowed at a higher rate than it could through spreading layers. It was observed that oil was displaced at a high rate to the injection channel shortly after CO_2 had entered the matrix through these paths, and an oil layer was created along the outer edge of the matrix in the channel. After a few seconds of CO_2 injection this layer was removed, as the volume oil displaced to the injection channel was lower than that transported to the production port by the CO_2 flowing in the channel (Figure 57). Even though this layer was removed, oil was still displaced through the same paths to the channel, only in smaller volumes.

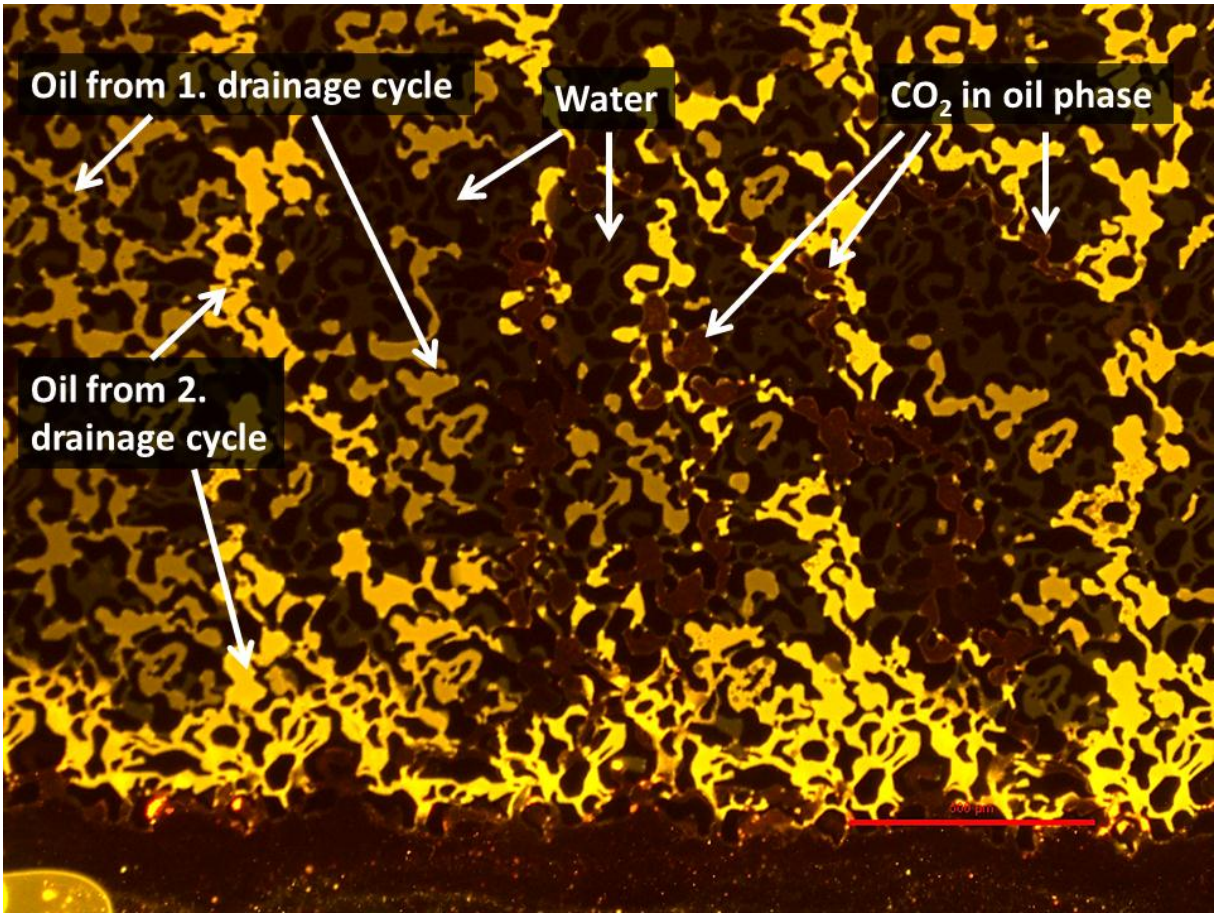

Figure 57: Discontinuous CO_2 in the matrix flowing in oil-filled pores.

An even CO_2 front in the matrix developed over several hours (Figure 58). This front was oriented normal to the injection channel, spanning across the network, and only oil was observed to remain in the area swept by CO_2.

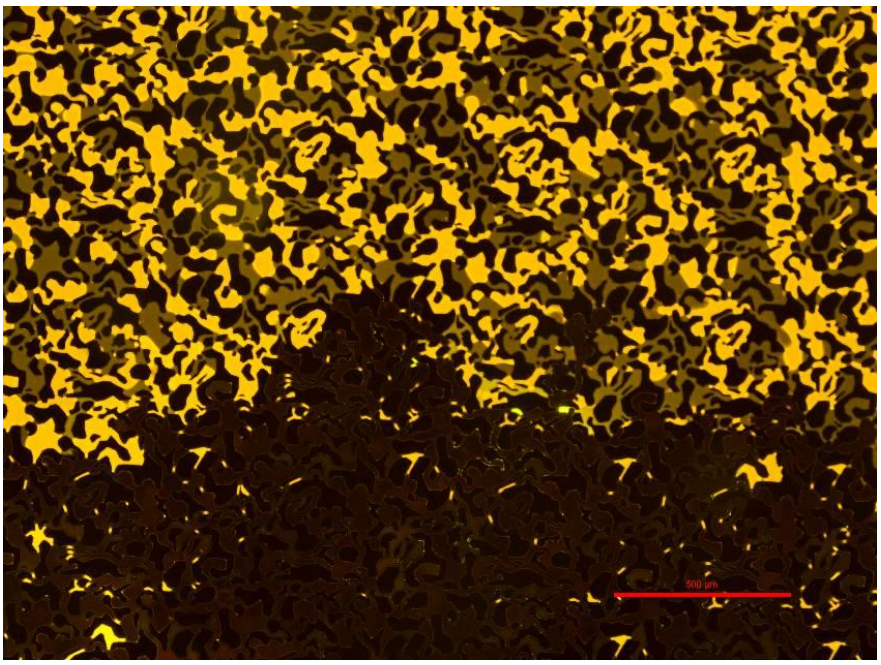

Figure 58: CO_2 front in the matrix after one day of injection.

6.5.4 Fracture/Matrix Interactions during CO_2 Injection at Irreducible Water Saturation

The importance of bulk displacement processes in fracture/matrix interactions at larger differential pressures across the pore network was investigated by injecting CO_2 at a constant pressure of 1 bar into micromodel Berea D, filled with oil and water at irreducible water saturation (S_{wi}=0.24). The experimental specifics are listed in Table 17.

Table 17: Experimental specifics for CO_2 in oil-filled micromodels at irreducible water saturation

Micromodel	Fluids in model	Injected fluid	Fluorescence	Injection pressure	Boundary conditions
Berea D	Water and oil	CO_2 gas	FT175 1:400 Nile Red 1:100 000	1.0 bars	OPEN

The CO_2 filled the injection channel first, before it continued straight into the matrix displacing oil, similar to the CO_2 injection with the production channel closed, described in section 6.5.3. However, CO_2 advanced both further and faster in comparison, and the displacement rate of oil was higher. CO_2 entering the matrix from the channel can be seen in Figure 59a-b. Continuous CO_2 paths in the matrix were not created even at this high flow rate, as the CO_2 moved through the matrix as discontinuous bubbles. It was observed that these bubbles followed the same flow paths, some of which can be seen in Figure 59b. Bulk displacement processes occurred in the matrix in the vicinity of the injection channel also here, meaning that the fracture/matrix mechanisms were the same. However, the increased flow rate through the matrix, and the increased range of the invading CO_2, resulted in a significant different macroscopic displacement.

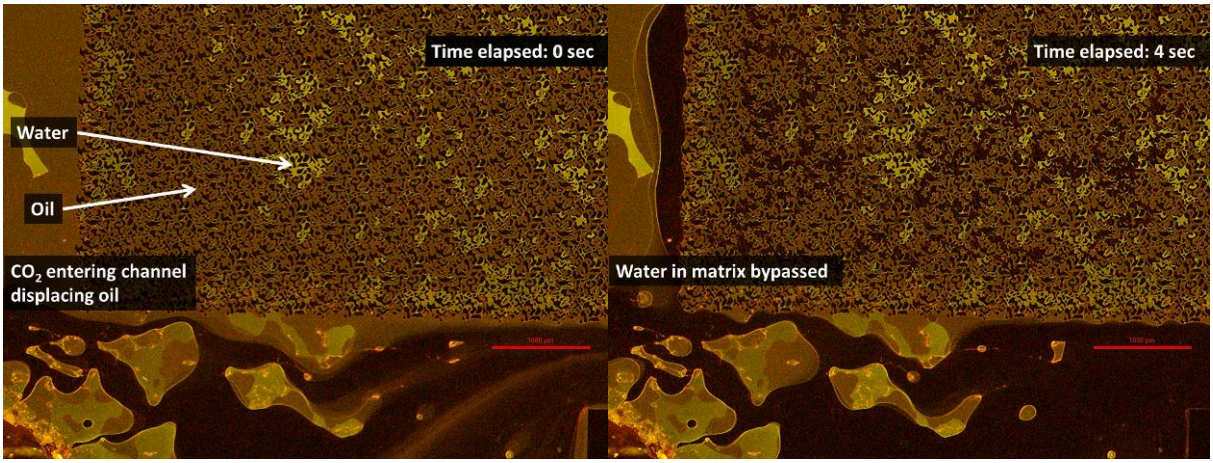

Figure 59ab: CO_2 entering an oil-filled micromodel at irreducible water saturation and instantly creating flow paths that transported CO_2 into the matrix beyond the view of the image.

6.5.5 Fracture/Matrix Interactions during CO_2 Injection in Partially Waterflooded Zones

Fracture/matrix interactions were also studied in the production channel by injecting CO_2 gas at a constant pressure of 1 bar in micromodel Berea G, partially filled with oil and water, where the water saturation was relatively high (> 50 %). The experiment was performed with all ports open, such that a significant differential pressure across the matrix existed. The experimental specifics are given in Table 18.

Table 18: Experimental specifics for CO_2 in partially waterflooded zones

Micromodel	Fluids in model	Injected fluid	Fluorescence	Injection pressure	Boundary conditions
Berea G	Water and oil	CO_2 gas	-	1 bar	OPEN

CO_2 advanced fast through the matrix to the opposite channel through preferred flow paths, and some CO_2 bubbles were capillary trapped in the matrix when the direction of preferred flow paths shifted. Even though the water saturation was higher than the oil saturation in the matrix, oil was still being produced efficiently. This was because it was transported as spreading layers together with CO_2 bubbles, and also displaced by water through multiple displacement events. As CO_2 flowed through the matrix, redistribution of water and oil occurred frequently. This pore level redistribution of fluids was observed to change the preferred CO_2 flow paths. An image sequence showing how fluid redistribution on the pore scale shifted a CO_2 flow path is shown in Figure 60a-h. Initially, CO_2 flowed to the production channel on the left side in the image sequence. Two identical large pores have been highlighted in Figure 60b, the leftmost was filled with oil through which the CO_2 was currently flowing, and the rightmost was filled with both water and oil. As CO_2 flowed through the matrix, redistribution of fluids caused the left pore to be filled with water, which effectively blocked the current CO_2 flow path. At the same time, oil invaded the pore on the right side, and a new flow path was created through this pore. A CO_2 bubble was capillary trapped in the original flow path when the flow shifted (appears in Figure 60e and is highlighted in Figure 60h).

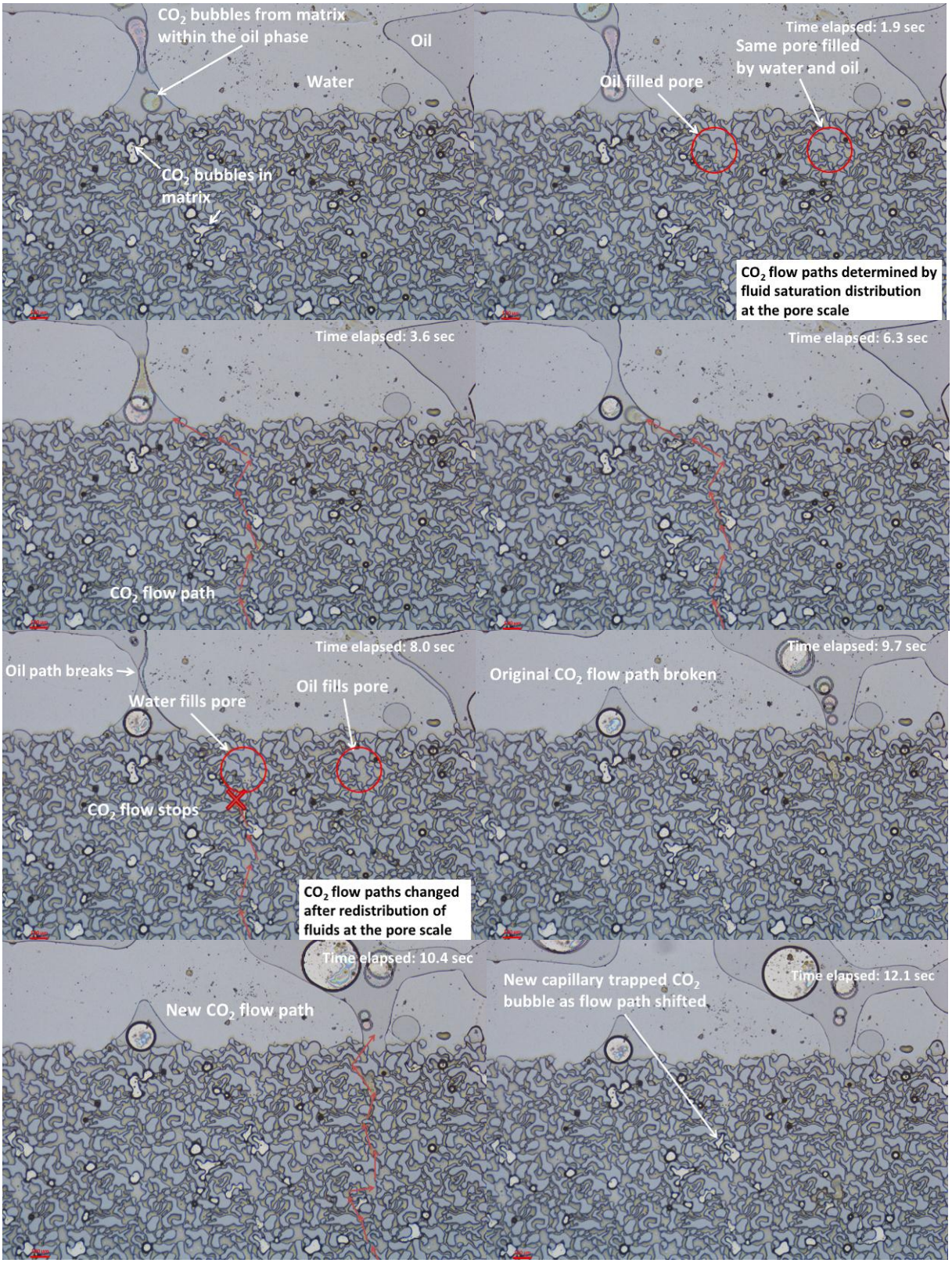

Figure 60abcdefgh: Fluid redistribution at the pore scale shifted a CO_2 flow path in the matrix during CO_2 injection in an oil- and water-filled micromodel.

The exact displacement mechanisms at the pore level causing the CO_2 flow path to shift is shown in Figure 61, where the area around the highlighted pores has been enlarged.

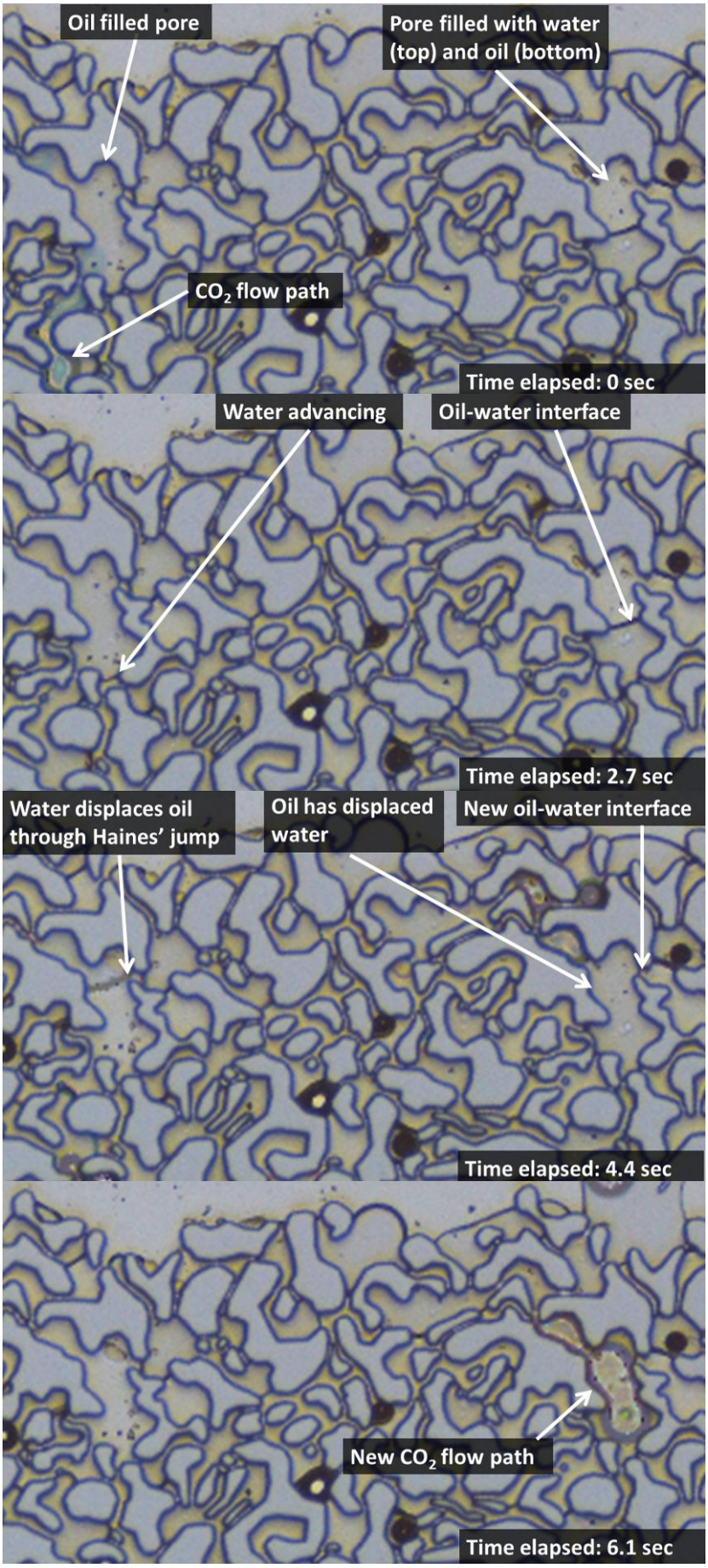

Figure 61abcd: Fluid displacements at the pore level causing a CO_2 flow path to shift.

The CO_2 flow path initially existed through mainly oil-filled pores, only interrupted by small water-filled throats. CO_2 was flowing through these pores without filling them as oil flowed back into the pores after CO_2 exited. The left pore in Figure 61a was contributing to the flow path when it was filled with oil. At some point, water in nearby throats advanced into this pore and displaced the oil. The large pore geometry caused the fluid interface to reach an unstable position, and the pore was instantly filled by a Haines' jump. At this time, the oil-water fluid interface had already advanced to fill the right pore with oil through an instant Haines' jump (Figure 61c). This caused the CO_2 flow to shift, and a new path was created through the right oil-filled pore (Figure 61d).

7 Discussions

7.1 Spontaneous Imbibition

Spontaneous imbibition of water in 2D micromodels was expected to be capillary dominated due to the small dimensions of micromodels. To support this assumption, simple estimates of the mobility ratio and the capillary number during water/air and water/CO_2 gas displacements was calculated. When assuming equal end-point relative permeabilities of water and air/CO_2, and using the fluid viscosities from Table 3, the mobility ratios at 20 ^{o}C can be estimated to:

$$M_{w/air} \approx \frac{\mu_{air}}{\mu_{water}} = \frac{0.01813cP}{1.002cP} \approx 0.0181$$

$$M_{w/CO_2} \approx \frac{\mu_{CO_2}}{\mu_{water}} = \frac{0.01469cP}{1.002cP} \approx 0.0147$$

Both of the approximated mobility ratios are much smaller than 1, which favors a stable displacement with no viscous fingering. Including the end-point relative permeability values would have given even lower mobility ratios as the micromodels were water-wet. The true flow velocity through the network is needed to estimate the capillary numbers in the displacements. If all the injected water flowed through the pore network, the volumetric flow rate, Q, was equal to the injection rate. When the production port in the injection channel was open, main flow was directed through this port, and lower flow rates through the pore network existed. The capillary number was estimated for expected flow rates during spontaneous imbibition, which range from 0.1 mL/h to 1 mL/h. When ignoring the tortuous flow paths through the network, and the reduced effective cross-sections of the pores due to water films, the true velocity can be estimated as follows:

$$v \approx \frac{Q}{A\phi} \qquad \textbf{(12)}$$

where *A* is the cross-sectional area of the pore space in the flow direction, estimated to the length of the channel times the etching depth. With the true flow velocity, the air/water and CO_2/water interfacial tensions from Table 3, and porosity of the silicon micromodels of 0.52, the capillary numbers are obtained from Equation (9) and presented in Table 19.

Table 19: Estimated capillary numbers for water/gas displacements at different flow rates

Volumetric flow velocity [mL/h]	True flow velocity [m/s]	N_c, Water/CO_2	N_c, Water/Air
0.1	$4.27*10^{-5}$	$6.02*10^{-7}$	$5.87*10^{-7}$
1.0	$4.27*10^{-4}$	$6.02*10^{-6}$	$5.87*10^{-6}$

The low estimated capillary numbers and mobility ratios support the expectations of capillary dominated flow. A very high injection rate would be required for viscous fingering to occur, and any instabilities is expected to appear through capillary fingering in both water/air and water/CO_2 displacements. As no experiments were performed directly to measure the capillary numbers by controlling the flow rate through the matrix, the estimates include large uncertainties and are only meant to be indicative. Discussions of observed fluid displacement processes and mechanism during spontaneous imbibition experiments follow below.

Flow Regimes during Spontaneous Imbibition

When looking at the larger flow patterns during the spontaneous imbibition experiments two different flow regimes were observed in several experiments. In the first flow regime, water advanced in an initial radial displacement pattern away from the point of injection, where the front spread out evenly in the pore space. Simultaneously, water imbibed into the matrix in other parts along the injection channel, also advancing with a stable front towards the production channel. At some point at higher water saturation in the matrix when the distance from the water front to the point of injection increased, fingers developed and dominated the displacement pattern with the fastest advancing fingers in the middle of the matrix. The second flow regime was identified by water advancing in a completely ramified pattern with fingers advancing in all directions immediately as it entered the matrix. It appeared that water late in the first flow regime was flowing by the same conditions as it was from the start in the second flow regime.

Stable Flow Regime

The flow regime that resulted in a radial displacement pattern was observed when a low differential pressure across the matrix existed, and the flow rate through the matrix was low. This was achieved by applying a low injection rate and closing the production channel, such that main flow was directed through the injection channel, and counter-current displacement of gas was forced. As a change in flow pattern was observed as the water front advanced in the matrix, it was suspected that viscous forces contributed in the displacement, as gravity forces were assumed negligible. To investigate this, a spontaneous imbibition experiment where no viscous forces across the matrix were expected, was performed in the following way:

- Micromodel Berea D was saturated with CO_2 to 100 % saturation
- The production channel was closed, and distilled water was injected through bottom left corner.
- Injection was stopped when water entered the injection channel, and water was allowed to capillary imbibe into the matrix.

When water entered the injection channel, it capillary imbibed into the matrix close to the injection point, and advanced through the matrix slowly with a stable front, similar to that during radial displacement in the first flow regime. However, water did not imbibe into the matrix in other parts along the injection channel. As water advanced through the matrix, it was clear that a radial pattern did not develop. Instead, a single broad finger advanced towards the production channel, sweeping a large area of the left side of the micromodel. This did not appear as a finger that originated from any unstable displacement, but appeared to be confined to a limited area because water was only accessible in this part of the micromodel. Very little CO_2 was left in the area swept by water, and no large CO_2-filled clusters were bypassed, as was seen during capillary fingering. The water front eventually stopped at some point in the matrix, before reaching the production channel.

The sweep efficiency in this simple experiment was comparable to sweep efficiencies in experiments conducted with closed production channel. A feature that also was similar was that no larger areas of CO_2 were trapped from merging of smaller water fingers at the water front. It was therefore suspected that the radial displacement pattern was close to capillary imbibition with little contribution of viscous forces in the flow direction across the matrix, and that a low imbibition rate prevented capillary fingers from developing. As the pressure drop in the water phase increased with increasing distance from the point of injection in the micromodels, more water flowed from the injection channel in that direction as the front advanced, and the flow rate increased. Breaking of the initial radial displacement pattern suggested that an unstable displacement occurred at higher flow rates. However, as the mobility ratio was very low, viscous forces were not expected to be significant

compared to capillary forces, even at high flow rates, which was assumed to be the cause that instabilities appeared in the form of capillary fingers. Contribution of viscous forces was observed as water entered the production channel. The much larger size of the channel (500 μm) compared to the pore throats (<20 μm) required that zero capillary pressure (from Equation 7) had to be obtained, before water could enter the channel. This would not be achieved by capillary imbibition as end-effect would cause a capillary hold up of water in the matrix. However, since water did not enter the channel immediately when it approached, but occurred after the water saturation and phase pressure had increased, the contribution of viscous forces was not considered to be great.

Capillary Fingering Flow Regime

The capillary fingering regime was observed when a significant differential pressure across the matrix existed, causing water to flow through the matrix at high flow rates. Viscous forces were assumed to contribute to the flow from the start, and flow was dominated by capillary fingering due to large capillary forces, resulting in trapping of large volumes of gas. Breakthrough to the production channel occurred immediately as the water approached, and in the vicinity of the breakthrough location it even flowed back into the matrix, suggesting that the water phase pressure was significant when it flowed through the matrix. It was observed that most trapped gas-filled clusters were invaded in the ramified finger regime, and this also suggested that higher viscous forces existed in the fluid displacements in this regime.

Pore Level Displacement Mechanisms

Pore level displacement events that were controlled by capillary pressure, could also be related to a pressure drop in the water phase as it advanced through the matrix in the two flow regimes. The condition for water to enter a pore can be explained on the basis of the capillary pressure equations (Equation 6 and Equation 7). When water faced gas-filled pores of larger sizes, a lower capillary pressure had to be obtained before water could enter, and this was achieved when the phase pressure of the water increased sufficiently. The following advancement of water lead to a minor pressure drop locally, as the distance from the injection port increased, and a larger volume became available for the water. The water flow stopped, and the same procedure was repeated.

In the radial flow regime, the water moved a short distance and filled few pores each time it advanced, which were followed by a minor pressure drop. However, the pressure increase was likewise slow, and once it increased sufficiently, water could only invade a few pores more in the next advancement. In the fingering regime where large clusters were filled in each advancing event, a larger pressure drop in the water phase occurred. However, as larger volumes of water flowed in the direction of the filling events at a high flow rate, the threshold pressure to continue advancing was reached faster, to a level where water could invade larger cluster of pores. This pulse-like advancement in both of the flow regimes meant that the water/gas interface advanced by instant Haines' jump at the pore level.

7.2 Primary Drainage

Prior to discussing the observed displacement processes during primary drainage, the mobility ratios and capillary numbers in oil/water and CO_2/water displacements can be estimated. The capillary numbers is estimated by equation (9) when oil was the non-wetting phase and equation (10) when this was CO_2. Mobility ratios can be estimated from Equation (11) for both cases. The mobility ratios were estimated with the assumption that end-point relative permeabilities of oil and CO_2 are equal to that of water, and the fluid viscosities are given in Table 3.

$$M_{o/w} \approx \frac{\mu_{water}}{\mu_{decane}} = \frac{1.002cP}{0.9135cP} \approx 1.089$$

$$M_{CO_2/w} \approx \frac{\mu_{water}}{\mu_{CO_2}} = \frac{1.002cP}{0.01469cP} \approx 68.21$$

The estimated mobility ratio for primary drainage with oil was close to unity, and the displacement was expected to be viscously stable. With CO_2 as the non-wetting phase, however, the estimated mobility ratio was 68, suggesting that a viscously unstable displacement could be expected. Table 20 shows the estimated capillary number for oil/water displacements at volumetric flow rates through the matrix of 0.1 mL/h and 1 mL/h. Greater flow rates than 1 mL/h across the matrix were in most cases not achievable without exceeding the differential pressure limitation of 2 bars. The capillary number for the CO_2/water displacements was estimated with a differential pressure across the flow length assumed to be equal to the injection pressure in the micromodels. To estimate a capillary number for the CO_2/water displacement process of a size comparable to that of oil/water however, the relative permeability of CO_2 must be included in the calculation. As no measurements of relative permeabilities were performed during the experiments, the capillary number was calculated for three relative permeability values. This introduced more uncertainties in the calculations, and the oil/water capillary number was also calculated for the same parameters for comparative reasons. The capillary numbers are shown in Table 21

Table 20: Estimated capillary numbers in primary drainage with oil at different injection rates

Volumetric flow velocity [mL/h]	Estimated true flow velocity [m/s]	N_c oil/water displacement
0.1	$4.27*10^{-5}$	$7.50*10^{-7}$
1.0	$4.27*10^{-4}$	$7.50*10^{-6}$

Table 21: Estimated capillary numbers in primary drainage with CO_2 and oil at different injection pressures

Relative permeability	N_c CO_2/water 0.2 bars	N_c CO_2/water 2.0 bars	N_c oil/water 0.2 bars	N_c oil/water 2.0 bars
0.1	$3.94*10^{-7}$	$3.94*10^{-6}$	$5.38*10^{-7}$	$5.38*10^{-6}$
0.5	$1.97*10^{-7}$	$1.97*10^{-6}$	$2.69*10^{-6}$	$2.69*10^{-5}$
1.0	$3.94*10^{-6}$	$3.94*10^{-5}$	$5.38*10^{-6}$	$5.38*10^{-5}$

The estimated capillary numbers show that capillary forces is significant when oil is the non-wetting phase in primary drainage, and that flow should be dominated by these forces when the favorable mobility ratio is taken into account. However, these estimates also indicate that viscous and capillary forces may become of comparable sizes at high flow rates, and high oil relative permeabilities. For drainage with CO_2, the capillary number estimates are of a magnitude suggesting that flow is not dominated by capillary forces at all flow conditions. With the highly unfavorable mobility ratio, viscous fingering may be introduced. For lower injection pressures, the displacement pattern may be stable depending on the magnitude of the viscous forces compared to capillary forces, and at high injection pressures, viscous forces should dominate. Nevertheless, viscous fingering is not expected to be visualized at the pore level, as the viscous pressure drop over a few pores is negligible compared to the capillary pressure drop across the CO_2/water interface. Over the complete pore space of the micromodels, however, the viscous pressure drop may be sufficiently large to introduce viscous fingering.

The experimental observations during primary drainage in this thesis can be related to viscous and capillary forces acting in the micromodels at different flow rates and boundary conditions. Similar

processes were observed when both oil and CO_2 was used as the non-wetting phase, and main processes will therefore be discussed for primary drainage with oil, while the observed differences when CO_2 was the displacing fluid will be discussed afterwards.

Flow Regimes during Primary Drainage with Oil

Two different flow regimes were also identified during primary drainage with oil. In the first regime, oil flowed in the matrix in a stable manner with a good sweep. Only small clusters of trapped water existed in the oil-swept area, and some of these trapped clusters were invaded. Oil fingers developed along the injection channel in locations away from where oil initially entered the matrix, but these did not dominate the flow pattern. In the second regime, an initially stable front was also observed moving radially away from the point of injection, but this pattern was disrupted quickly, and oil fingers developed. As these oil fingers reached and entered the production channel, no more water was displaced. In addition, no trapped water was seen to be displaced. The initial radial displacement pattern that appeared in both regimes suggested that viscous forces contributed to stabilizing the displacement process. It was found that the opposite of what was observed during spontaneous imbibition, that a low differential pressure and flow rate across the matrix stabilized the process, occurred during primary drainage with oil.

Stable Flow Regime

Oil flow stable regime was observed when production channel was open, and a significant differential pressure existed across the matrix. The displacement pattern at these conditions resembled the pattern observed during the spontaneous imbibition experiment described in the discussion section 7.1, where a single broad finger advanced to the production channel. The initial radial oil front advanced much faster than the radial front in the capillary fingering regime. Viscous forces appearing from a higher flow rate appeared to be sufficiently to balance the capillary forces, and achieve a stable displacement. It was therefore suspected that the large finger that advanced towards the production channel was a result of the direction of the largest pressure drop, rather than a result of an unstable displacement. Signs of instabilities late in this flow regime were manifested by smaller fingers originating from locations along the injection channel, and at the edges of the oil front. When oil in the matrix connected to the oil in the injection channel, the viscous pressure drop was reduced locally. Higher viscous forces enabled oil to advance into the matrix also in these areas, and it appeared that these fingers preferably advanced towards the larger, suggesting that the pressure drop was greatest in this direction (ref. Figure 44). Bypassing of water from merging of small fingers at the slow moving end of the large finger (Figure 43), suggested that viscous forces in these locations.

Capillary Fingering Flow Regime

The capillary fingering regime was observed when the production channel was closed, and flow rate through the matrix was slow. The radial pattern that appeared initially suggested that viscous forces balanced capillary forces also at these conditions. However, since small oil fingers were seen to merge and trap water early, it appeared that capillary forces were close to dominating the displacement. This was supported as oil fingers developed as the distance from point of injection increased, and a larger viscous pressure drop was expected. Also, no trapped water was displaced in this regime, and water displacement stopped after breakthrough to the production channel. From these observations, it appeared that oil followed the easiest available flow path through the network, decided to a large degree by the capillary pressure. The oil flow appeared to follow the principles of invasion percolation by entering pores of least capillary entry pressures consequently.

To produce more water after initial breakthrough, viscous forces had to be increased in the process, and it was observed that an increased injection rate resulted in additional water production.

Primary Drainage with CO_2

Primary drainage with CO_2 showed the same flow patterns as primary drainage with oil. The significant difference in mobility ratios in the two processes was seen to affect the irreducible water saturation, as higher water saturation existed behind the CO_2 front compared to behind the oil front. Direct comparison is done visually in Figure 62 where an image from primary drainage with CO_2, taken at 5x magnification, is placed on top of an image from primary drainage with oil at 2x magnification. Clearly more water was bypassed when CO_2 was the displacing fluid.

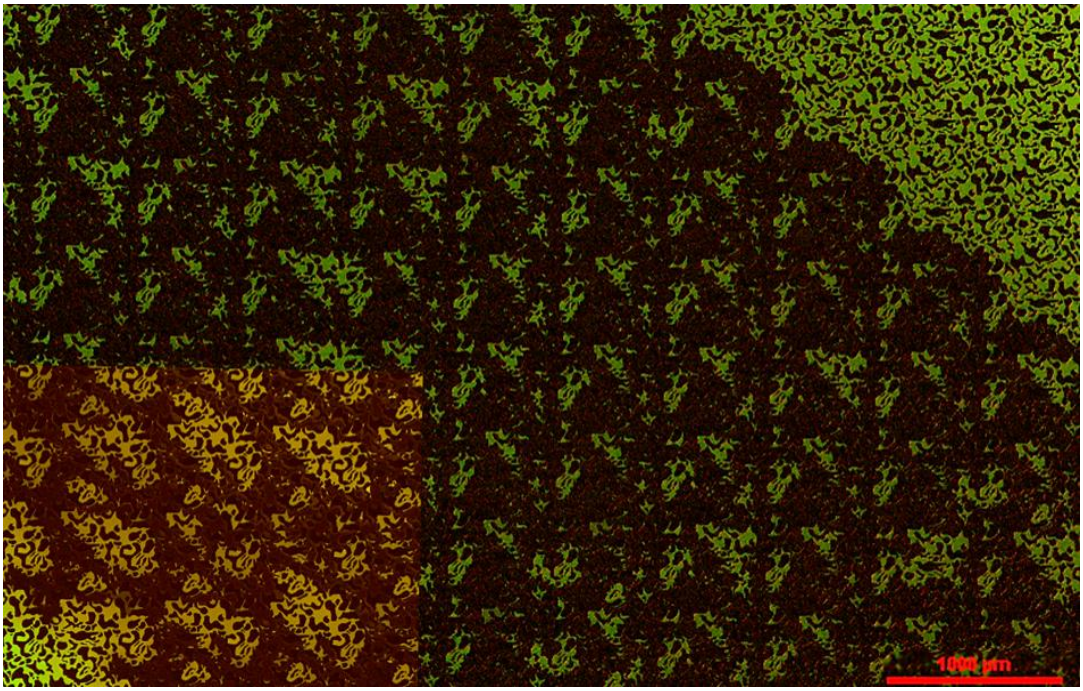

Figure 62: Comparison of sizes of trapped water-filled clusters during primary drainage with CO_2 and oil.

The pore level observations in the image sequence in Figure 48a-d, showing an advancing CO_2 finger, revealed a feature that was not observed during primary drainage with oil. When this small finger stopped advancing, the viscous pressure drop in the CO_2 phase was most likely too large to displace water from nearby pores by piston displacements. The following CO_2 invasion that displaced water through film flow in nearby pores only appeared when CO_2 was the non-wetting fluid. The color of the CO_2 changed from dark brown to light brown in this process, indicating that the concentration of CO_2 was decreasing. In Figure 63ab, a pore from the image sequence in Figure 48a-d has been enlarged, where this effect can be seen. The reduced concentration suggests that CO_2 entered the available pores and drained water through film flow as a result of gas expansion when the pressure decreased.

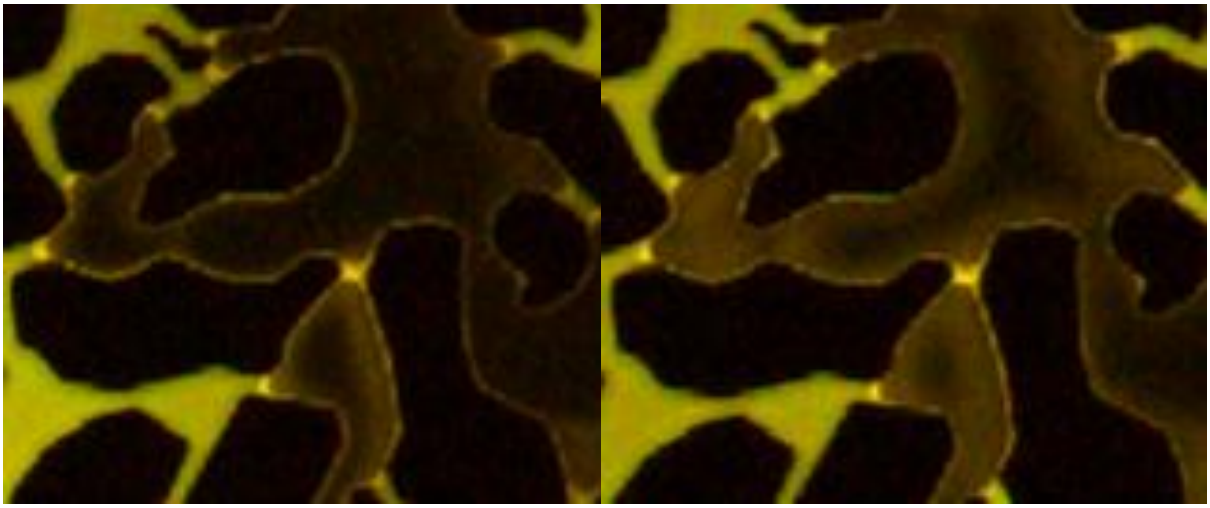

Figure 63ab: Decreasing CO_2 concentration after an initially advancing CO_2 finger stopped, when CO_2 drained water from nearby pores through film flow.

Properties measured during primary drainage experiments are listed in Table 22, and a summary of the observed flow regimes with the conditions that favored these are listed Table 23.

Table 22: Threshold pressure and contact angles measured during primary drainage.

Matrix threshold pressure for oil	CO_2/water receding contact angle	Oil/water receding contact angle
0.27 ± 0.2 bars	≈ 15°	≈ 18°

Table 23: Summary of flow regimes observed during spontaneous imbibition and primary drainage experiments.

Displacement process	Flow conditions	Flow regime	Characteristic features
Primary drainage	High Δp and high flow rate	Stable front	Good sweep Low S_{wi} in swept area Film flow of trapped water Production of water continued after breakthrough.
Primary drainage	Low Δp and low flow rate	Unstable capillary fingering	Poor sweep No film flow of trapped water Production of water stopped after breakthrough
Water imbibition	High Δp and high flow rate	Unstable capillary fingering	Poor sweep Imbibition into trapped gas clusters
Water imbibition	Low Δp and low flow rate	Stable front	Good sweep Low residual air saturation Little imbibition into trapped gas clusters Stability due to low capillary imbibition rate

7.3 Three-Phase Flow during CO_2 Gas Injection

Visualization of three-phase flow and fluid displacements during CO_2 gas injection at ambient conditions could be studied at a great range of saturations in partially oil- and water-filled micromodels. The two flow channels in the micromodels also allowed fracture/matrix interactions, resembling those in fractured reservoirs, to be studied. As experiments were conducted at ambient conditions, many of the properties that make CO_2 great for EOR measures, including reduction of oil viscosity, swelling of the oil and miscible displacement, could not be studied. The displacement processes were therefore more or less limited to immiscible three-phase flow.

It was seen that oil was preferably displaced as CO_2 was injected, even at high water saturations. For this reason, the total oil production was very efficient, especially at high oil saturations where larger oil-filled clusters existed in continuous paths to the production channels. A theoretical approach to explain the filling nature of the CO_2 can be done by looking at the capillary pressure equations, Equation 6 and 7, and comparing the required CO_2 phase pressure to invade oil- and water-filled pores with a given radius *r*:

$$P_{o_{CO_2}} = P_o + P_{c,go} = P_o + \frac{2\sigma_{go}\cos\vartheta_{go}}{r} \quad \text{(i)}$$

$$P_{w_{CO_2}} = P_w + P_{c,gw} = P_w + \frac{2\sigma_{gw}\cos\vartheta_{gw}}{r} \quad \text{(ii)}$$

Where $P_{o_{CO_2}}$ and $P_{w_{CO_2}}$ denotes the phase pressure of CO_2 to enter an oil-filled and a water-filled pore, respectively. The difference in phase pressures can be found by subtracting (ii) from (i), which gives:

$$\begin{aligned} P_{o_{CO_2}}(r) - P_{w_{CO_2}}(r) &= P_o + \frac{2\sigma_{go}\cos\vartheta_{go}}{r} - \left(P_w + \frac{2\sigma_{gw}\cos\vartheta_{gw}}{r}\right) \\ &= \frac{2\sigma_{ow}\cos\vartheta_{ow}}{r} + \frac{2\sigma_{go}\cos\vartheta_{go}}{r} - \frac{2\sigma_{gw}\cos\vartheta_{gw}}{r} \\ &= \sigma_{ow}\cos\vartheta_{ow} + \sigma_{go}\cos\vartheta_{go} - \sigma_{gw}\cos\vartheta_{gw} \end{aligned} \quad \text{(iii)}$$

Where $P_o - P_w = \frac{2\sigma_{ow}\cos\vartheta_{ow}}{r}$ has been used in the second step.

The interfacial tensions and contact angles are related to each other in the following way (Bartell, F.E. and Osterhof, H.J., 1927):

$$\sigma_{ow}\cos\vartheta_{ow} = \sigma_{go}\cos\vartheta_{go} - \sigma_{gw}\cos\vartheta_{gw} \quad \text{(iv)}$$

When (iv) is solved for $\cos\vartheta_{go}$ and substituted in (iii), this gives:

$$\begin{aligned} P_{o_{CO_2}}(r) - P_{w_{CO_2}}(r) &= \sigma_{ow}\cos\vartheta_{ow} + \sigma_{go}\left(\frac{\sigma_{gw}\cos\vartheta_{gw}}{\sigma_{go}} - \frac{\sigma_{ow}\cos\vartheta_{ow}}{\sigma_{go}}\right) - \sigma_{gw}\cos\vartheta_{gw} \\ &= \sigma_{ow}\cos\vartheta_{ow} + \sigma_{gw}\cos\vartheta_{gw} - \sigma_{ow}\cos\vartheta_{ow} - \sigma_{gw}\cos\vartheta_{gw} \\ &= 0 \end{aligned}$$

These simple calculations show that no difference in CO_2 phase pressure should be required to displace water rather than oil from identical pores. This is given if one considers a case where oil injection into water-filled porous media was performed, and stopped before the irreducible water saturation was reached. The obtained phase pressure of oil was large enough to invade water-filled pores of a given size, but not enough to invade infinitesimally smaller water-filled pores. Identical capillary pressures would exist in these pores as the differences in sizes were negligible. The pores would be invaded by oil simultaneously if this was achieved, assuming that all other conditions are equal.

CO_2 should not displace oil rather than water in the micromodels from pores of equal sizes. However, as oil was occupying most of the large pores in the matrix before CO_2 was injected, these were invaded first as the preference for CO_2 also was to enter larger pores, since wettability of the micromodels were in the order of CO_2 < oil < water. However, it was observed that even though larger pores were water filled, these were not preferably invaded. It appeared that whether CO_2 invaded a pore or not also depended on the fluid configurations, continuity of phases, wetting films and spreading layers. Of these factors, the spreading layer of oil was assumed to be the most important one. CO_2 was never in direct contact with water, which always had to be displaced through multiple displacement events. The spreading layers of oil and the wetting films of water also affected displacement processes by being able to conduct fluids even at low saturations.

Oil Production Mechanisms during CO_2 Injection

The pore level observations mentioned in section 6.4 were contributing factors to the faster production of oil than that of water, which was observed even at higher water saturations. The observation that oil existed in continuous paths from the matrix to the production channels, was considered to originate from zero capillary pressure existing in the channel, and a smaller phase pressure of oil compared to water was required to exit the matrix. Also, the higher displacement rate of oil from the matrix to the production channels ensured that enough oil was supplied. From the CO_2 experiments into partially oil- and water-filled micromodels described in section 6.4 it was evident that displacement processes were affected by the distribution of fluids in the micromodels, and especially the saturation history. This is best demonstrated when considering the fluid configurations in Figure 52. In that particular experiment (described in section 6.5.1), an additional imbibition cycle was performed after primary drainage, resulting in the water saturation in the micromodel being higher than S_{wi}. More important than the average water saturation in the micromodel, in terms of producing the oil, was the distribution of water. Water was continuous over larger clusters of pores in restricted areas of the matrix, where it could even occupy large pores. These pores had been filled during the last water imbibition cycle when a continuous water path from the injection channel enabled water to displace the oil from these pores. As CO_2 preferably entered the larger pores, more multiple displacement events of water occurred during CO_2 injection, and more discontinuous phases and shifting of CO_2 flow paths reduces displacement efficiency of oil.

The impact of phase continuity and local pressure distribution on pore level filling was seen during the fracture/matrix interaction experiment described in section 6.5.5. The original CO_2 flow path that existed through oil-filled pores was disrupted when multiple displacements caused water to enter a large oil-filled pore in this path. The resistance for CO_2 to flow in the original flow path increased as a consequence, since flow that initially involved two-phases and single displacement processes, now involved three-phase flow and multiple displacement events. Higher CO_2 phase pressure was required to displace oil back into the pore through which the original flow path existed, and an easier flow path elsewhere was found. The spreading layer of oil was found to contribute to the oil production by two different processes. Obviously, oil in spreading layers was produced together with

the CO_2, a mechanism that became increasingly important with decreasing oil saturation. In addition, the shifting of CO_2 flow paths away from the water-filled pores to the oil-filled pores was also assumed to be a mechanism that promoted oil production. Gas expansion was also observed, and could be an additional displacement mechanism, but this was not assumed to be significant.

Displacement Mechanisms during CO_2 Injection

The overall fluid distribution after a day of CO_2 injection, shown in both Figure 55 and Figure 58, indicated the relative importance of diffusive processes compared to bulk displacements. The even shape of the CO_2 fronts suggested that diffusive processes were contributing to the displacements, as even though main flow was directed away from the areas still unswept by CO_2, water and oil were continuously removed. However, as oil was present in the area fully swept by CO_2 while water was not, flow through films may have been more important than diffusive processes. The solubility of CO_2 in n-decane at 1 atm (≈ 1 bar) and 25°C was found in the literature to be 1.583 mL CO_2 per mL decane/CO_2 solution (Wilcock, R.J., Battino, R., Danforth, W.F. and Wilhelm, E., 1978). With a density of CO_2 at the same pressure and temperature of 0.001808 g/mL (NIST Chemistry WebBook, 2012) this gives a solubility of CO_2 in decane equal to 3.16 g/L. The same value for water was found to be 1.45 g/L earlier, which indicates that CO_2 should dissolve more easily in the oil phase. The residual oil in the CO_2 swept area was therefore considered to be an effect of the spreading layer being removed through diffusive processes before all oil drained. Water films were still present since water had been removed, or at least they existed for a longer time after the CO_2 front had passed.

A summary of the displacement mechanisms that were observed during CO_2 injection in partially oil- and water-filled micromodels are listed in Table 24 for both water and oil displacements. The different mechanisms have been linked to whether the displaced fluids were trapped or not, but it should be noted that the link only means that a given mechanisms was preferred. Snap-off events during CO_2 displacement of oil occurred more often than piston displacement if the trapped clusters were large. The typical displacement speed has also been indicated for the processes in the table. This does also depend on pressure and flow rate, and is only meant to be comparable for the different mechanisms. The values represent displacements at lower flow rates and pressures when the mechanisms could be fully observed, and describe the time it took to drain the invaded pore by CO_2, not the overall displacement speed. The displacement of trapped oil was therefore faster than displacement of continuous oil, even though the total displacement rate most likely was larger in the latter case.

Table 24: Summary of displacement mechanisms observed during CO_2 injection and three-phase flow

Displaced fluid	Trapped/not trapped	Displacement mechanism	Displacement speed
Water	Trapped	Double or multiple displacements	Tens of seconds to minutes
Water	Not trapped	Double or multiple displacements	Tens of seconds
Oil	Trapped	Haines' jump	Instantly
Oil	Not trapped	Snap-off	Seconds to tens of seconds

Part 3: Conclusions and Future Work

8 Conclusions

From the experimental observations during spontaneous water imbibition, primary drainage and CO_2 gas injection and three-phase flow, these conclusions can be made:

General Conclusions

- An experimental setup was built where flow in micromodels could be performed and studied, and where both liquids and gases could be injected at ambient pressures and temperatures.
- Multiphase flow could be visualized by the use of a microscope and a camera, and fluids were easily distinguished by the use of fluorescent additives.
- With silicon micromodels that had adopted properties of real porous rocks, study of flow processes similar to those in real reservoirs was possible.
- Control on flow processes was possible by adjusting flow rates and injection pressures, and changing the boundary conditions by closing and opening production ports.

Spontaneous Imbibition

- Two flow regimes were found during spontaneous imbibition. In the first regime water flowed stably through the matrix at a rate controlled by the imbibition rate, with good sweep efficiency. In the second regime the water supply to the matrix was large enough to introduce capillary fingering, and low sweep efficiency was achieved.
- The differential pressure and the flow rate across the matrix affected by which regime water flowed. For low values water flowed by the stable regime, and for large values water flowed by the fingering regime.
- During spontaneous imbibition, counter-current displacement, end-effects, and dissolution of gas into the water phase could be studied, and the gas/water advancing contact angle was measured.

Primary Drainage

- Two flow regimes were also found during primary drainage. In the first regime, oil flowed with a stable front at a relatively high rate with good sweep efficiency. In the second regime, oil flowed in a sparse fingering pattern with poor sweep efficiency and early breakthrough.
- Flow was in the stable regime when a significant differential pressure and flow rate existed across the matrix. At low flow rates, the capillary fingering regime was followed.
- Displacement of water on the pore scale was, in the order of decreasing speed, by the following processes: stable and unstable piston events including double displacement events, drainage through film flow, and also mobilization due to gas expansion when CO_2 was the non-wetting phase.
- Counter-current displacement and bypass of water from merging of both small and large fingers could be visualized and investigated, and measurements of threshold pressure, oil/water and CO_2/water receding contact angles and fluid saturations could be performed.

Three-Phase CO_2 Injection

- N-decane was found to be spreading in a water/n-decane/CO_2 system at ambient conditions, forming a spreading layer between water and CO_2.
- The spreading layer of oil and water films along the matrix grains ensured that both fluids could flow in hydraulically connected paths even at low saturations.
- Wetting order of the silicon micromodels was found to be in the order of CO_2<oil< water, meaning that CO_2 preferably entered the large pores that commonly was filled with oil, even if it had to pass water-filled throats in the process.
- CO_2 displaced oil through piston displacement events, both with a stable moving fluid interface and by instant Haines' jumps, and by bubbles flowing into the middle of oil-filled pores by a snap-off mechanism and expanding outwards.
- Whether a piston displacement or snap-off event occurred depended on the pressure drop in the displacement process, and whether the oil in the invaded pores were trapped or continuous affected the magnitude of the pressure drop. Haines' jump was favored in displacement of trapped oil, and snap-off events in displacement of continuous oil.
- CO_2 was never in direct contact with water due to the spreading oil layer, and water was always displaced through multiple displacement events.
- The filling nature of CO_2 created numerous discontinuous clusters of all three phases, which moved around in a chaotic manner as local pressure distribution changed in the matrix.
- CO_2 flowed in preferred flow paths mainly through oil-filled pores, and redistribution of discontinuous fluids in the matrix could interrupt and shift these flow paths.
- The spreading layer of oil contributed to an efficient oil production during CO_2 injection. Oil was displaced both together with the CO_2 and through bulk flow to production channels, even if oil existed mostly in discontinuous clusters in the matrix.
- When the oil saturation in the preferred CO_2 flow paths became low, the CO_2 found new paths through other oil-filled pores, also ensuring an efficient oil production.

9 Future Work

As fundamental processes were studied in this thesis, and as part of the objective was to identify the displacement mechanisms and fluid flow processes, more investigation in each of the topics that has been touched in this thesis is required. Some suggestions of further work in the Berea micromodel at ambient conditions follows below:

- Experiments with better control on flow parameters for further investigation of the physics affecting the displacement in the micromodels.
- Better estimated of capillary numbers and mobility ratios should be obtained, which enables the possibility to study the fluid flow regimes as function of these.
- Experiments with CO_2 gas injection where recovery efficiency is better investigated.
- N-decane should be replaced with a more viscous oil to study CO_2 flooding more relevant to reservoir conditions
- Mobility control on the CO_2 gas by injecting CO_2 foam. CO_2 foam feasibility studies were performed during the writing of this thesis where an AOS-surfactant was used as the foaming agent. CO_2 foam was injected and observed in the micromodels, but difficulties in generating stable foam in the pore space was the main obstacle. The stability of the CO_2 foam can be increased by using suited foaming agents, and CO_2 foam experiments should be performed.

Multiphase flow in micromodels was studied at ambient pressure and temperature conditions in this thesis. This limited the fluid displacement processes to immiscible flow at conditions different from those in oil reservoirs. Modification on the experimental setup so that experiments can be conducted at elevated pressures and temperatures will enable study of fluid flow at reservoir conditions. Currently, a micromodel designed for high pressure is under development at the Dept. of Physics and Technology, which has been pressure tested up to 80 bars. This enables visualization of miscible displacement of oil by CO_2 injection, and displacements during oil production with both supercritical and liquid CO_2 should be investigated.

As most of the research attention at the Dept. of Physics and Technology is on oil recovery from carbonate rocks, development of micromodels based on these rocks is an ongoing progress. A pore network constructed from thin-section of a limestone is under development, and visualization of fluid displacements in these rocks should also be performed.

10 Notations

g = Gas
o = Oil
w = Water
V_b = Bulk volume of porous rock
V_p = Pore volume of porous rock
ϕ = Porosity
p = Pressure
P_i = Phase pressure of fluid *i*
P_c = Capillary pressure
θ = Wetting angle
μ = Viscosity
σ = Interfacial tension
Q = Volumetric flow rate
v = True flow velocity
A = Cross-sectional area
L = Length
r = Radius
K = Permeability
K_i = Effective permeability of fluid *i*
k_r = Relative permeability
k^o_r= End-point relative permeability
λ = Mobility
M = Mobility ratio
N_c = Capillary number
I = Amott-Harvey wettability index
W = USBM wettability index
REV = Representative elementary volume

11 References

AMOTT, E. 1959. *Observations Relating to the Wettability of Porous Rock*.

ANDERSON, W. G. 1986a. *Wettability Literature Survey- Part 1: Rock/Oil/Brine Interactions and the Effects of Core Handling on Wettability*. SPE Journal of Petroleum Technology**,** 1125-1144.

ANDERSON, W. G. 1986b. *Wettability Literature Survey- Part 2: Wettability Measurement*. SPE Journal of Petroleum Technology**,** 1246-1262.

AYIRALA, S. C., XU, W. & RAO, D. N. 2006. *Interfacial Behaviour of Complex Hydrocarbon Fluids at Elevated Pressures and Temperatures*. The Canadian Journal of Chemical Engineering*,* **84,** 22-32.

BARTELL, F. E. & OSTERHOF, H. J. 1927. *Determination of the Wettability of a Solid by a Liquid*. Industrial & Engineering Chemistry*,* **19,** 1277-1280.

BEAR, J. 1988. *Dynamics of Fluids in Porous Media*, Dover.

BLUNT, M. & KING, P. 1991. *Relative permeabilities from two- and three-dimensional pore-scale network modelling*. Transport in Porous Media*,* **6,** 407-433.

BONEAU, D. F. & CLAMPITT, R. L. 1977. *A Surfactant System for the Oil-Wet Sandstone Of the North Burbank Unit*. SPE Journal of Petroleum Technology**,** 501-506.

CHUN, B.-S. & WILKINSON, G. T. 1995. *Interfacial tension in high-pressure carbon dioxide mixtures*. Industrial & Engineering Chemistry Research*,* **34,** 4371-4377.

DONALDSON, E. C., THOMAS, R. D. & LORENZ, P. B. 1969. *Wettability Determination and Its Effect on Recovery Efficiency*.

ECOTOXICOLOGY, E. C. F. & CHEMICALS, T. O. 1994. *Linear polydimethylsiloxanes (viscosity 10 - 10,000 centistokes): CAS*, ECETOC.

FOWLER, S. D. & GREENSPAN, P. 1985a. *Application of Nile red, a fluorescent hydrophobic probe, for the detection of neutral lipid deposits in tissue sections: comparison with oil red O*. Journal of Histochemistry & Cytochemistry*,* **33,** 833-6.

FOWLER, S. D. & GREENSPAN, P. 1985b. *Spectrofluorometric studies of the lipid probe, nile red*. Journal of Lipid Research*,* **26,** 781-9.

GU, J. 2010. *A Microvisual Investigation of Viscously Unstable Displacement for CO2 Injection.* Master of Science, Stanford University.

HORNBROOK, J. W., CASTANIER, L. M. & PETTIT, P. A. 1991. *Observation of Foam/Oil Interactions in a New, High-Resolution Micromodel*. *SPE Annual Technical Conference and Exhibition.* Dallas, Texas: 1991 Copyright 1991, Society of Petroleum Engineers, Inc.

JASPER, J. J. 1972. *The Surface Tension of Pure Liquid Compounds*, American Chemical Society.

JOHNSON JR, R. E. & DETTRE, R. H. 1966. *The wettability of low-energy liquid surfaces*. Journal of Colloid and Interface Science*,* **21,** 610-622.

KENNETH G, R. 1982. *Fluorescein. Physicochemical factors affecting its fluorescence*. Survey of Ophthalmology*,* **26,** 269-283.

KOVSCEK, A. R., TANG, G. Q. & RADKE, C. J. 2007. *Verification of Roof snap off as a foam-generation mechanism in porous media at steady state*. Colloids and Surfaces A: Physicochemical and Engineering Aspects*,* **302,** 251-260.

LENORMAND, R., TOUBOUL, E. & ZARCONE, C. 1987. *Immiscible Displacements in Porous Media: Testing Network Simulators by Micromodel Experiments*. *SPE Annual Technical Conference and Exhibition.* Dallas, Texas: 1987 Copyright 1987, Society of Petroleum Engineers.

LENORMAND, R., TOUBOUL, E. & ZARCONE, C. 1988. *Numerical models and experiments on immiscible displacements in porous media*. Journal of Fluid Mechanics*,* **189,** 165-187.

MA, K., RIVERA, J., HIRASAKI, G. J. & BISWAL, S. L. 2011. *Wettability control and patterning of PDMS using UV–ozone and water immersion*. Journal of Colloid and Interface Science*,* **363,** 371-378.

MATHIASSEN, O. M. 2003. *CO2 as Injection Gas for Enhanced Oil Recovery and Estimation of the Potential on the Norwegian Continental Shelf.* Master of Science, NTNU.

MELROSE, J. C. 1965. *Wettability as Related to Capillary Action in Porous Media*.
MOORE, T. F. & SLOBOD, R. L. 1955. *Displacement of Oil by Water-Effect of Wettability, Rate, and Viscosity on Recovery*.
MORROW, N. R. 1970. *Physics and Thermodynamics of Capillary Action in Porous Media*. Industrial & Engineering Chemistry*,* **62,** 32-56.
NIST CHEMISTRY WEBBOOK. 2012. Available: http://webbook.nist.gov/chemistry/ [Accessed May 30th 2012].
SARATHI, P. 1986. *Using Micromodels to Study Steam Displacement Processes in Porous Media*. United States. Dept. of Energy.
SUTHERLAND, W. 1893. *LII. The viscosity of gases and molecular force*. Philosophical Magazine Series 5*,* **36,** 507-531.
TABER, J. J. 1969. *Dynamic and Static Forces Required To Remove a Discontinuous Oil Phase from Porous Media Containing Both Oil and Water*.
WILCOCK, R. J., BATTINO, R., DANFORTH, W. F. & WILHELM, E. 1978. *Solubilities of gases in liquids II. The solubilities of He, Ne, Ar, Kr, O2, N2, CO, CO2, CH4, CF4, and SF6 in n-octane 1-octanol, n-decane, and 1-decanol*. The Journal of Chemical Thermodynamics*,* **10,** 817-822.
WILKINSON, D. & WILLEMSEN, J. F. 1983. *Invasion percolation: a new form of percolation theory* Journal of Physics A: Mathematical and General*,* **Volume 16,** 13.
WILLIAMS, R. T. & BRIDGES, J. W. 1964. *FLUORESCENCE OF SOLUTIONS: A REVIEW*. Journal of clinical pathology*,* **17,** 371-94.
WWW.ENGINEERINGTOOLBOX.COM. 2012. *Solubility of Gases in Water & Air Solubility in Water* [Online]. Available: http://www.engineeringtoolbox.com/air-solubility-water-d_639.html
http://www.engineeringtoolbox.com/gases-solubility-water-d_1148.html [Accessed May 27th 2012].
ZOLOTUKHIN, A. B. & URSIN, J. R. 2000. *Introduction to petroleum reservoir engineering*, Høyskoleforlaget, Norwegian Academic Press.